

UCLA

UCLA Electronic Theses and Dissertations

Title

Mechanized Mesoporous Inorganic Nanoparticles for Drug Delivery Applications: Design, Optimization and Properties

Permalink

<https://escholarship.org/uc/item/4wp149qg>

Author

Xue, Min

Publication Date

2013

Peer reviewed|Thesis/dissertation

UNIVERSITY OF CALIFORNIA
Los Angeles

Mechanized Mesoporous Inorganic Nanoparticles for Drug Delivery Applications:
Design, Optimization and Properties

A dissertation submitted in partial satisfaction of the
requirements for the degree Doctor of Philosophy
in Chemistry

by

Min Xue

2013

ABSTRACT OF THE DISSERTATION

Mechanized Mesoporous Inorganic Nanoparticles for Drug Delivery Applications:
Design, Optimization and Properties

by

Min Xue

Doctor of Philosophy in Chemistry
University of California, Los Angeles, 2013
Professor Jeffrey I. Zink, Chair

The research covered in this dissertation is described in six chapters. The first two chapters focus on the design of supramolecular nanovalves on mesoporous silica and silicon materials to form drug delivery systems. These systems are capable of autonomously releasing drug molecules *in vitro*. The third chapter describes size-selective nanovalves that are able to control the release of both large and small molecules. These nanovalves are constructed on mesoporous silica materials with 6.5 nm pores. The fourth chapter demonstrates two experimental methods, dynamic fluorescence anisotropy and rigidochromism spectroscopy, for probing the properties of the microenvironment inside the mesopores of mesoporous silica nanoparticles. In the fifth chapter of this dissertation, the design and operation of a chemical amplifier based on enzyme-encapsulated mesoporous silica are shown. This system employs a pH-responsive nanogate assembly to control the access to the encapsulated enzyme. It is the

first example of a chemical amplifier that is activated by and also amplifies the same type of reaction. The last chapter describes the spectroscopic consequences of the excited state mixed valence in a binuclear copper complex using a neighboring orbital model. The copper complex represents a new class of excited state mixed valence compounds, where the coupling of two equivalent charge-bearing units is mediated through a copper-iodine cluster. The result from the simple neighboring orbital approach is supported by resonance Raman spectroscopy and Gaussian calculations.

The dissertation of Min Xue is approved.

Paula L. Diaconescu

Andre E. Nel

Jeffrey I. Zink, Committee Chair

University of California, Los Angeles

2013

This dissertation is dedicated to my family and my friends

TABLE OF CONTENTS

ACKNOWLEDGEMENTS	viii
VITA	xi
Chapter 1 pH-Sensitive Nanovalves For Autonomous <i>in vitro</i> Drug Release	
1.1 Abstract	2
1.2 Introduction	3
1.3 Experimental	4
1.4 Results and Discussion	7
1.5 Summary	11
1.6 Tables and Figures	12
1.7 References	19
Chapter 2 pH-Operated Mechanized Porous Silicon Nanoparticles	
2.1 Abstract	23
2.2 Introduction	24
2.3 Experimental	24
2.4 Results and Discussion	27
2.5 Summary	31
2.6 Tables and Figures	32
2.7 References	41
Chapter 3 Size-Selective Megagates On Mesoporous Silica Materials	
3.1 Abstract	45
3.2 Introduction	46
3.3 Experimental	47
3.4 Results and Discussion	51
3.5 Summary	55
3.6 Figures	56
3.7 References	62
Chapter 4 Probing The Microenvironment Inside The Mesopores	
4.1 Abstract	66
4.2 Introduction	67
4.3 Experimental	68
4.4 Results and Discussion	70
4.5 Summary	81
4.6 Figures	82
4.7 References	95

**Chapter 5 A Chemical Amplifier Based On Enzyme-Encapsulated
Mesoporous Silica Nanoparticles**

5.1	Abstract	97
5.2	Introduction	98
5.3	Experimental	98
5.4	Results and Discussion	101
5.5	Summary	105
5.6	Figures	106
5.7	References	111

**Chapter 6 Excited State Mixed Valence In A Binuclear Cu(I) Complex Analyzed
By A Neighboring Orbital Model**

6.1	Abstract	114
6.2	Introduction	115
6.3	Experimental	116
6.4	Results	117
6.5	Discussion	118
6.6	Summary	122
6.7	Tables and Figures	123
6.8	References	137

ACKNOWLEDGEMENTS

It seems impossible for me to make a complete list of people that I should dedicate my acknowledgement to, for there are so many of them and everyone of them has helped me survived and enjoyed these past five years.

First of all, I want to acknowledge my advisor, Prof. Jeffrey I. Zink, for being a wonderful mentor. Five years ago, it was him that found my misplaced application and eventually helped me get an offer from UCLA. Without his effort, I would never be able to stand where I am and become who I am now. During my study here, I have tremendously benefited from his profound knowledge and scientific insights. He has taught me how to conduct decent research and how to be a good scientist. He has provided me with so many great opportunities to collaborate with other groups and to participate in all types of research projects. It is my great fortune to have him as my Ph.D. advisor and if I were be able to become a professor myself, I would like to be just as wise and inspiring as him.

I would like to acknowledge my colleagues and friends in the Zink group. I want to thank Dr. Sarah Angelos for teaching me the basic techniques of nanomachine experiments when I first joined the group and providing help for my first nanovalve project. I would like to thank Dr. Monty Liong for training me in nanoparticle synthesis and greatly helped me during my first year. I want to thank Dr. Sanaz Gardner, who provided me with so much knowledge on both science and life. I have never met anyone that is as good tempered and patient as her. I would like to thank Dr. Daniel Ferris for teaching me so much about the American society and helping me in establishing my own research projects. He is probably the funniest person I have ever met and I have learned a lot from him. I want to thank Dr. Yaroslav Klichko, Dr. Rachel Stephenson, Dr. Phillip Rutkowski, Dr. Ryan Hoekstra, Dr. Marcelle Dibrell, Dr. Bryanna Henderson, and Dr. Travis Pecorelli for their help during my study. I want to thank Dr. Yuen Lau for all the great food

that we have enjoyed together and all the happy talks that we shared. She is also a great scientist that I really enjoy spending time with. I also want to thank her for her help and support in my German study. I would like to thank Dr. Courtney Thomas for be a great friend and a great colleague, who have not only set up a great example of a good scientist for me, but also taught me how to interact with people and how to properly handle conflicts. I want to thank Dr. Li Du, who was an exchange student when I first joined the group, for her help and support in my early struggling times at UCLA. I want to give my special thanks to Dr. Zongxi Li and Angela Hwang for sharing all the ups and downs in the group. They are the dearest sisters that I never had and I am really grateful for having them in my life. I would like to thank Tania Guardado and Melissa Russell for spending times with me and always being supportive to me; thank Matt Kiesz and Janie Chen for being good fellows and sharing the beauty of spectroscopy with me; thank Eunshil Choi, Jon Brosmer, Sui Yang, Zilu Li, Dr. Lorraine Raboin and Dr. Philippe Saint-Circq Riviere for making my days in the group special. I want to thank Derrick Tarn for being such a great friend to me. He has helped me in understanding the culture and adapting to the environment. Without him, lots of things would not be as good as they are now to me. I also want to thank Juyao Dong for all the happy moments we share and all the valuable discussions we had. I would like to thank Prof. Yan-Li Zhao, who was a postdoc in the Zink group, for his great help in organic synthesis.

Next I would like to thank my collaborators, without whom most of my research projects would not be as successful and meaningful as they are now. I want to thank Prof. Andre E. Nel for his guidance in biomedical areas. His work ethics and enthusiasm in science have a great impact on me. It has been really inspiring working with him. I also would like to thank Dr. Huan Meng from the Nel group, who has not only been a great collaborator but also a generous friend. He has provided me with tremendous amount of help and priceless advices and I could never be able to pay him back for those. I would like to thank Dr. Tian Xia, Dr. Zhaoxia Ji, Dr. Haiyuan

Zhang and Dr. Sijie Lin from the Nel group for their help and support during my graduate studies. I want to thank Prof. J. Fraser Stoddart, his student Denise Cao and his postdoc Dr. Deniz Yilmaz for the great help during our collaborative work. I also would like to thank Prof. Xiangfeng Duan and his students Xing Zhong, Teng Xue and Hua Zhang for their kind collaborations for a number of projects. I want to thank Prof. Fuyuhiko Tamanoi and Dr. Zory Shaposhnik for the help in conducting cell experiments in mesoporous silicon materials. I want to thank Dr. Marcus Horwitz, Dr. Daniel Clemens and Dr. Bai-Yu Lee for their contributions in the collaborative work on the Tb projects. I would like to thank Prof. Kent Pinkerton from UC Davis and his student Xueting Li for giving me the opportunities of working on the silica inhalation projects.

I want to thank my friends outside of the school. I want to thank Alexander Afanasyev for being a great roommate and a close friend and for his generous help on all kinds of things in my life. I am really lucky to have such a friend. I would like to thank Haodong Chen and Letian Dou for their help and for sharing all the happy times we spent together. I want to thank Min Xu, Huangjian Zhou, Xiaojiang Xie, Jinyi Hu and Bo Shen for being great brothers to me and for their everlasting support to me. I would also like to thank Dr. Yuewei Sheng and Chaochao Cai for their help and friendship that are really valuable to me.

I would like to thank my family: my parents and my dear wife Fang Wang for bringing me happiness and being supportive to me all the time.

At last, I would like to thank Prof. Paula L. Diaconescu and Prof. Andre E. Nel for serving on my dissertation committee.

VITA

2008	B.S. in Chemistry Nanjing University Nanjing, China
2008-2013	Teaching Assistant Department of Chemistry and Biochemistry University of California, Los Angeles Los Angeles, California
2009-2013	Research Assistant Department of Chemistry and Biochemistry University of California, Los Angeles Los Angeles, California

PUBLICATIONS

(* Co-First Authors)

1. **M. Xue**, D. Cao, J. F. Stoddart, J. I. Zink, "Size-Selective pH-Operated Megagates on Mesoporous Silica Materials" *Nanoscale*, **2012**, *4*, 7569-7574.
2. D. Tarn, **M. Xue**, J. I. Zink, "pH-Responsive Dual Cargo Delivery from Mesoporous Silica Nanoparticles with a Metal-Latched Nanogate" *Inorg. Chem.*, **2013**, *52*, 2044-2049.
3. D. Tarn, C. E. Ashley, **M. Xue**, E. C. Carnes, J. I. Zink, C. J. Brinker, "Mesoporous Silica Nanoparticle Nanocarriers: Biofunctionality and Biocompatibility" *Acc. Chem. Res.*, **2013**, *46*, 792-801.
4. H. Meng,* **M. Xue**,* J. I. Zink, A. E. Nel, "Development of Pharmaceutically Adapted Mesoporous Silica Nanoparticles Platform" *J. Phys. Chem. Lett.*, **2012**, *3*, 358-359.
5. H. Meng, W. X. Mai, H. Zhang, **M. Xue**, T. Xia, S. Lin, X. Wang, Y. Zhao, Z. Ji, J. I. Zink, A. E. Nel, "Codelivery of an Optimal Drug/siRNA Combination Using Mesoporous Silica Nanoparticles To Overcome Drug Resistance in Breast Cancer in Vitro and in Vivo" *ACS Nano*, **2013**, *7*, 994-1005.
6. H. Zhang, D. R. Dunphy, X. Jiang, H. Meng, B. Sun, D. Tarn, **M. Xue**, X. Wang, S. Lin, Z. Ji, R. Li, F. L. Garcia, J. Yang, M. L. Kirk, T. Xia, J. I. Zink, A. E. Nel, C. J. Brinker, "Processing Pathway Dependence of Amorphous Silica Nanoparticle Toxicity: Colloidal vs Pyrolytic" *J. Am. Chem. Soc.*, **2012**, *134*, 15790-15804.

7. D. L. Clemens, B. Y. Lee, **M. Xue**, C. R. Thomas, H. Meng, D. Ferris, A. E. Nel, J. I. Zink, M. A. Horwitz, "Targeted Intracellular Delivery of Antituberculosis Drugs to Mycobacterium tuberculosis-Infected Macrophages via Functionalized Mesoporous Silica Nanoparticles" *Antimicrobial Agents and Chemotherapy*, **2012**, *56*, 2535-2545.
8. H. Zhang, T. Xia, H. Meng, **M. Xue**, S. George, Z. Ji, X. Wang, R. Liu, M. Wang, B. France, R. Rallo, R. Damoiseaux, Y. Cohen, K. A. Bradley, J. I. Zink, A. E. Nel, "Differential expression of syndecan-1 mediates cationic nanoparticle toxicity in undifferentiated versus differentiated normal human bronchial epithelial cells" *ACS Nano*, **2011**, *5*, 2756-2769.
9. **M. Xue**,* X. Zhong,* Z. Shaposhnik,* Y. Qu, F. Tamanoi, X. Duan, J. I. Zink, "pH-Operated mechanized porous silicon nanoparticles" *J. Am. Chem. Soc.*, **2011**, *133*, 8798-8801.
10. H. Meng,* **M. Xue**,* T. Xia, Z. Ji, D. Tarn, J. I. Zink, A. E. Nel, "Use of size and a copolymer design feature to improve the biodistribution and the enhanced permeability and retention effect of doxorubicin-loaded mesoporous silica nanoparticles in a murine xenograft tumor model" *ACS Nano*, **2011**, *5*, 4131-4144.
11. H. Meng,* **M. Xue**,* T. Xia,* Y. L. Zhao, F. Tamanoi, J. F. Stoddart, J. I. Zink, A. E. Nel, "Autonomous in vitro anticancer drug release from mesoporous silica nanoparticles by pH-sensitive nanovalves" *J. Am. Chem. Soc.*, **2010**, *132*, 12690-12697.
12. **M. Xue**, L. Huang, J. Q. Wang, Y. Wang, L. Gao, J. Zhu, Z. Zou, "The direct synthesis of mesoporous structured MnO₂/TiO₂ nanocomposite: a novel visible-light active photocatalyst with large pore size" *Nanotechnology*, **2008**, *19*, 185604-185608.
13. J. Wang, L. Huang, **M. Xue**, Y. Wang, L. Gao, J. Zhu, Z. Zou, "Architecture of a Hybrid Mesoporous Chemosensor for Fe³⁺ by Covalent Coupling Bis-Schiff Base PMBA onto the CPTES-Functionalized SBA-15" *J. Phys. Chem. C*, **2008**, *112*, 5014-5022.
14. J. Wang, L. Huang, **M. Xue**, L. Liu, Y. Wang, L. Gao, J. Zhu, Z. Zou, "Developing a novel fluorescence chemosensor by self-assembly of Bis-Schiff base within the channel of mesoporous SBA-15 for sensitive detecting of Hg²⁺ ions" *App. Surf. Sci.*, **2008**, *254*, 5329-5335.

Chapter 1

pH-Sensitive Nanovalves for Autonomous in vitro Drug Release

1.1 Abstract

Mesoporous silica nanoparticles (MSNP) have proven to be an extremely effective solid support for controlled drug delivery on account of the fact that their surfaces can be easily functionalized in order to control the nanopore openings. The Zink group has described previously a series of mechanized silica nanoparticles, which, under abiotic conditions, are capable of delivering cargo molecules employing a series of nanovalves. The key question for these systems has now become whether they can be adapted for biological use through controlled nanovalve opening in cells. In this chapter, I present a novel MSNP delivery system capable of drug delivery based on the function of β -cyclodextrin (β -CD) nanovalves. This system is responsive to the endosomal acidification conditions in human differentiated myeloid (THP-1) and squamous carcinoma (KB-31) cell lines. I also demonstrate how to optimize the surface functionalization of the MSNP so as to provide a platform for the effective and rapid doxorubicin release to the nuclei of KB-31 cells.

I would like to acknowledge my collaborators, Dr. Huan Meng and Dr. Yan-Li Zhao for participating in the research presented in this chapter.

1.2 Introduction

Mesoporous silica nanoparticles¹ (MSNP) are versatile, non-cytotoxic solid supports for nanogate-controlled drug delivery.² Mechanized silica nanoparticles that are capable of stimuli-responsive release of cargo molecules are presently under active investigation.³ A key challenge for these integrated systems is whether they can be designed for biological use through autonomously controlled nanogate opening inside cells of interest. Herein, I present a MSNP delivery system based on the operation of supramolecular nanogates that are tightly closed at physiological pH (7.4) but capable of opening and delivering drugs in acidifying cellular compartments. I demonstrate how to optimize the system for operation at certain pH levels for the efficient release of some drug molecules by varying the surface functionalization of the nanopores. The operation of this autonomous integrated nanosystem with appropriate design features is demonstrated in human differentiated myeloid (THP-1) and squamous carcinoma (KB-31) cell lines with the help of my collaborator Dr. Huan Meng.

The MSNP employed in this work are ~100 nm spheres containing ordered two-dimensional hexagonal arrays of tubular pores with diameters of ~ 2 nm. The nanopores are large enough to contain common biological dyes and anticancer drugs, yet small enough to be blocked by macrocyclic organic molecules, such as the cyclodextrins. There is currently much interest³ in developing stimuli-responsive methods for controlling access to and from the nanopores. These methods range from coating the nanoparticles with polymers⁴ to controlling individual nanopores with molecules that undergo large-amplitude motions.^{2b} The latter offers the highest degree of control because the “gatekeeper” molecules are bonded covalently inside or at the entrances of the nanopores.^{3a} The MSNP pores also have been functionalized with nanoimpellers, or supramolecules, including pseudorotaxanes, as well as molecules, such as bistable rotaxanes and simpler rotaxanes of the “snap-top” variety^{3a} at the nanopore entrances. These systems respond to physicochemical stimuli such as light, oxidation/reduction, enzymes,

and changes in pH in order to release the trapped cargo molecules.⁵ For *in vitro* or *in vivo* biological applications, both external stimuli (such as light^{5a}) as well as autonomous conditions (for example, intracellular enzymes^{5b} or pH^{5c-g}) can be used. In this chapter, I demonstrate the autonomous activation of supramolecular nanovalves on mechanized silica nanoparticles initiated by intercellular pH changes without invasive control.

1.3 Experimental

Materials

3-Aminopropyltriethoxysilane (APTS, 99%), ammonium chloride (>99%), cetyltrimethylammonium bromide (CTAB, 90%), β -cyclodextrin (98%), *N,N'*-dicyclohexylcarbodiimide (99%), doxorubicin (98%), FITC-dextran (MW = 70,000), fluorescein isothiocyanate (FITC, 90%), phorbol-12-myristate-13-acetate (PMA, >99%), 1-pyreneacetic acid (97%), tetraethylorthosilicate (TEOS, 90%), and 3-(trihydroxysilyl)propylmethylphosphonate monosodium aqueous solution (42%) were purchased from Sigma. *N*-(2-Aminoethyl)-3-aminopropyltrimethoxysilane (90%) and chloromethyltrimethoxysilane (90%) were obtained from Gelest. Benzimidazole (98%) was purchased from Fluka. Mono(6-diethylenetriamino-6-deoxy)- β -cyclodextrin was prepared according to literature procedures.⁶

Synthesis of MSNP

In a typical synthesis, cetyltrimethylammonium bromide (CTAB, 250 mg, 0.7 mmol) was mixed with NaOH solution (875 μ L, 2 M) and H₂O (120 mL). The mixture reaction was heated to 80 °C. Fluorescein isothiocyanate (2.7 mg) was dissolved in absolute EtOH (1.5 mL) and mixed with 3-aminopropyltriethoxysilane (6 μ L) for 2 h. After the temperature had stabilized, tetraethylorthosilicate (1.2 mL) was mixed with the ethanolic FITC-APTS solution and added to the CTAB solution. For amine-modified samples, *N*-(2-aminoethyl)-3-aminopropyl-

trimethoxysilane [60 (5% w/w), 90 (7.5% w/w) or 120 (10% w/w) μL] was mixed with TEOS-FITC-APTS solution. For phosphonate-coated nanoparticles, 3-(trihydroxysilyl) propylmethylphosphonate (315 μL) was added to the solution after 15 min. The solution was stirred vigorously at 80 °C for 2 h. The synthesized nanoparticles were centrifuged and washed with MeOH.

Synthesis of 1-methyl-1*H*-benzimidazole (MBI)-modified nanoparticles

Benzimidazole (24 mg, 0.2 mmol) was dissolved in anhydrous *N,N'*-dimethylformamide (DMF, 2.2 mL). Tetrabutylammonium iodide (4 mg) and anhydrous NEt_3 (0.3 mL) were added into the solution, followed by adding chloromethyltrimethoxysilane (30 μL). The solution was heated to 70 °C under N_2 for 24 h. The solvent was then removed in vacuo and the resulting mixture was washed with hexane. The mixture was added to a PhMe/EtOH suspension (40 mL of PhMe and 1 mL of EtOH) of the as-synthesized MSNP (200 mg). The suspension was refluxed under N_2 for 12 h, centrifuged and washed with MeOH. The CTAB surfactants were removed by dispersing the as-synthesized materials in MeOH (60 mL) and concentrated HCl (2.3 mL, 12 M), and refluxed under N_2 for 12 h. The materials were collected by centrifugation and washed with MeOH.

Synthesis of pyrene-modified β -cyclodextrin

Mono(6-diethylenetriamino-6-deoxy)- β -cyclodextrin (1.22 g, 1.0 mmol) and *N,N*-dicyclohexylcarbodiimide (0.21 g, 1.0 mmol) were dissolved in DMF (30 mL) in the presence of a small amount of 4 Å molecular sieves under an atmosphere of Ar. 1-Pyreneacetic acid (0.26 g, 1.0 mmol) was dissolved in DMF (10 mL) and then added dropwise into this solution. The reaction mixture was stirred for 2 days in an ice bath and then for another 2 days at room temperature, before being left to stand for 5 h until no more precipitate was deposited. The precipitate was removed by filtration, and the filtrate was poured into acetone (150 mL). The

precipitate that formed in acetone was collected by filtration and subsequently purified on a Sephadex G-25 column with water as eluent. After the residue had been dried in vacuo, a pure sample (0.66 g, 45 %) of mono[6-(1-pyreneacetamido)diethylenediamino-6-deoxy]- β -cyclodextrin was obtained as a colorless solid. ^1H NMR (500 MHz, D_2O , 25 °C, TMS): δ = 2.48–2.61 (m, 8H, $\text{NCH}_2\text{CH}_2\text{N}$), 3.58–3.86 (m, 42H), 4.21 (s, 2H, COCH_2Py), 4.95–5.04 (m, 7H), 7.86–8.11 ppm (m, 9H, Py-H); MS (HR-MALDI): Calcd for $\text{C}_{64}\text{H}_{93}\text{N}_3\text{O}_{35}$ m/z 1463.56, found m/z 1462.56 [M^+].

Drug loading

For Hoechst 33342 loading, MBI-modified nanoparticles (50 mg) were mixed with Hoechst 33342 (5 mL) in aqueous solution (1 mM). The suspension was stirred for 12 h before β -cyclodextrin (200 mg) or pyrene-modified β -cyclodextrin (200 mg) was added. The mixture was stirred for another 12 h, and the nanoparticles were centrifuged and washed with H_2O . For doxorubicin loading, MBI-modified nanoparticles (10 mg) were mixed with an aqueous solution (0.25 mL, 4 mg mL^{-1}) of doxorubicin and stirred for 12 h. Then, β -cyclodextrin (40 mg) was added before stirring for another 12 h. The sample was then centrifuged and washed with H_2O .

Assessment of drug release

The release profiles were obtained by time-resolved fluorescence spectroscopy, as previously described^{5d}. Briefly, a probe beam (448 nm, 20 mW for doxorubicin-loaded samples; 377 nm, 16 mW for Hoechst-loaded samples) was directed into the water or cell culture medium to excite the dissolved cargo molecules. The luminescence spectrum of the dissolved cargo was collected in 1 sec. intervals over the course of the experiment. 0.1 M HCl was added to decrease the pH to desired value. The luminescence intensity at the emission maximum of the dye was plotted as a function of time to generate a release profile.

Physicochemical characterization of MSNP coated with nanovalves

MSNP coated with nanovalves were characterized for sizes, zeta potentials, and shapes, respectively. The shapes and porous structures were characterized using transmission electron microscopy (JEOL JEM 2010, JEOL USA, Inc., Peabody, MA). The nanoparticle sizes and zeta potentials in pure water, BSA water solution (1 mg mL⁻¹), and cell culture media were measured by ZetaSizer Nano (Malvern Instruments Ltd., Worcestershire, UK). All of the measurements were performed with the nanoparticles suspended in filtered water or filtered cell culture media at 40 µg mL⁻¹ nanoparticle concentration.

1.4 Results and Discussion

A nanovalve delivery system was designed to meet a specific criterion, i.e., the nanovalve must be closed tightly at pH 7.4 – the pH of blood – but self-open in acidifying endosomal compartments, such as lysosomes. In order to achieve this objective, it is necessary to construct stalks that can be attached covalently to the nanopore openings and, in turn, will bind a capping agent, capable of blocking the nanopore openings reversibly. The interaction – a function of the binding constant – must be pH-dependent and change from a large value at pH 7.4 to a small one in response to mild endosomal acidification conditions that will trigger the release of the cap. After experimentation with a number of pH-responsive nanovalve components, a series of aromatic amines were chosen as the stalk and β-cyclodextrin (β-CD) as the cap. The β-CD ring encircles the stalks (Figure 1.1a) as a result of noncovalent bonding interactions under neutral pH conditions and effectively blocks the nanopore openings and traps the included cargo molecules. Lowering of the pH leads to protonation of the aromatic amines, followed by β-CD cap release and cargo diffusion from the nanopores.

In order to achieve the attachment and release of the β-CD caps in the lysosomes of these cells, it was necessary to develop a nanovalve system that responds to the acidification

level (pH<6) that is attainable in the LAMP1-positive endosomal compartments of THP-1 and KB-31 cells. After testing a range of aromatic amines that exhibit different pK_a values (Table 1), the *N*-methylbenzimidazole (MBI) stalk (Figure 1.1b) was chosen as the best candidate. Upon protonation, the mechanized MSNP release their β -CD caps without causing any cytotoxicity.

The nanovalves were attached covalently to MSNP, comprised of ~100 nm primary nanoparticles with uniform pore size ~2 nm, as indicated by TEM (Figure 1.1c). The MBI stalks were synthesized and attached covalently to the MSNP surfaces by means of a post-synthesis protocol (Figure 1.1a). The attachment was confirmed by ^{13}C -CPMS NMR and ^{29}Si -CPMS NMR spectroscopies (Figure 1.2).

In order to verify the functioning of the nanovalve system at appropriate pH conditions, the functionalized MSNP were first of all loaded by soaking in concentrated solutions of Hoechst 33342 dye or the fluorescent chemotherapeutic agent, doxorubicin. The nanoparticles were then capped with β -CD in a concentrated aqueous solution and washed carefully. The release of the trapped fluorescent molecules was tested in H_2O at pH 7.0 and monitored by time-resolved fluorescence spectroscopy. The capped and loaded nanoparticles were placed in the corner of a cuvette and the surrounding liquid was stirred gently. A probe beam was used to illuminate the liquid above the nanoparticles and to excite the fluorescent molecules as they escaped the nanoparticles. The nanovalves remain closed at pH 7 with no cargo leakage as shown in Figure 1.2, but upon decreasing the pH to 5, the fluorescent guest molecules were released. In order to demonstrate that this process is accompanied by β -CD release, the β -CD caps were labeled with pyrene. These fluorescent caps were monitored by UV-Vis spectroscopy so as to be able to follow their release into the supernatant (Figure 1.3a). The rapid release curve shows that β -CD release precedes the release of the Hoechst dye.

Curiously, the doxorubicin release was slow and incomplete compared to the Hoechst dye. This observation raises the possibility that the cationic nature of this chemotherapeutic agent ($pK_a = 8.2$) causes it to interact electrostatically with the negatively charged Si-O⁻ groups in the MSNP nanopores and thus are held relatively tightly to the nanoparticles. In order to alleviate this problem and obtain more rapid and complete release of doxorubicin, the next step in the design strategy was to modify the MSNP surface to prevent electrostatic interactions (Figure 1.4a). Positively charged ammonium groups were attached to the MSNP surface by a co-condensation method.^{3a} Due to the cationic nature of doxorubicin, the positively charged molecules interact electrostatically with the unmodified MSNP surface (Si-O⁻ group). This relatively strong binding interaction leads to slow drug release upon valve opening (upper panel). To speed up drug release, it is hypothesized that the attachment of a positively charged group (e.g. ammonium) will prevent the electrostatic binding and get more rapid drug release (Figure 1.4a, lower panel). Optimization of the release was achieved by testing a series of concentrations of the ammonium groups to find the cationic density at which the increase in electrostatic interactions – limiting the loading capacity of doxorubicin – is outweighed by an optimal rate of release. Figure 1.4b shows the loading yield of MSNP with different surface modifications. The MSNP at an ammonium concentration of 7.5% (w/w) show a moderate doxorubicin loading (1.7%, w/w): they can, however, release doxorubicin rapidly so that the MSNP yield the maximum drug delivery per unit time (Figure 1.4c). Thus, functionalization with 7.5% ammonium was used in all subsequent experiments for doxorubicin delivery. Figure 1.2b shows the improved pH-dependant release profiles of doxorubicin from the ammonium-modified compared to unmodified MSNP (Figure 1.2a). The fine tuning of the MSNP pores to optimize cargo specific drug delivery is another important design feature of our system.

In order to prove that the nanovalve integrated system remains functional under biologically relevant conditions, including the presence of buffered salts and growth

supplements, Hoechst and doxorubicin release were tested in THP-1 and KB-31 cell culture media. The respective release profiles in RPMI 1640 (THP-1) and DMEM (KB-31) are similar to those in H₂O, and are shown in Figure 1.5a and 5b. The flat baselines and the typical release curves demonstrate that the nanovalve remain operational under culture media conditions.

In order to verify these operational limits, confocal microscopy was used to follow the kinetics of Hoechst dye and doxorubicin release in THP-1 and KB-31 cells, respectively. Hoechst-loaded, FITC-labeled MSNP are efficiently taken up (Figure 1.6a) in THP-1 cells. At the earlier times (1h and 3h), the Hoechst dye is retained in the nanoparticles that localize in the peri-nuclear regions as fluorescent blue dots, suggesting that the MSNP delivery system does not leak (Figure 1.6a). However, this visual image changed after 6 h when the Hoechst dye was released to the nuclei of THP-1 (Figure 1.6a). This release was accompanied by the disappearance of the blue dots in the peri-nuclear region, while the FITC-labeled nanoparticles could still be visualized at this site for up to 36 h. Moreover, NH₄Cl treatment, which can prevent the acidification of lysosomal compartment, was quite effective at confining the Hoechst dye and FITC-labeled nanoparticles to the peri-nuclear regions without observable nuclear staining (Figure 1.6a, right panel).

While studying doxorubicin release in KB-31, these cells also efficiently took up FITC-MSNP to the peri-nuclear regions within 3 h, whereupon there was observable drug release (red fluorescence) to the nucleus (Figure 1.6b). This release was followed by progressive nuclear changes that reflect the pharmacological effect of the drug, including the formation of apoptotic bodies by 60 h and nuclear fragmentation by 80 h. Again, this visual image was dramatically changed by NH₄Cl treatment, a situation which led to most of the drug being retained inside the nanoparticles and little or no evidence of nuclear staining and cell death (Figure 1.6b, right panel).

1.5 Summary

In summary, I demonstrate pH-sensitive nanovalve-functionalized MSNP that function as a drug delivery vehicle in cells. The *N*-methylbenzimidazole stalks with the optimized pK_a endow the nanovalves with the capability of binding β -CD ring strongly at pH 7.4 and trapping dye and drug molecules in the nanopores. Deprotonation at pH <6 – as in acidifying endosomal compartments – causes dissociation of the β -CD caps and releases of the cargo molecules. By modifying the interior of the silica surface, the rate of release of the positively charged doxorubicin molecules was increased. Nanoparticles loaded with Hoechst dye and the anticancer drug doxorubicin were efficiently taken up into acidifying endosomal compartments in THP-1 and KB-31 cells. Doxorubicin release from within the LAMP-1 positive endosomal compartments results in apoptotic cell death in KB-31 cells. The fact that drug release and cell killing can be inhibited by lysosomal pH neutralizer NH_4Cl supports the hypothesis that the cargo release is caused by lysosomal acidification. The development of pH-sensitive MSNP, functionalized with nanovalves, could potentially improve the efficacy and safety of drug delivery¹³ for chemotherapeutic agents.¹⁴

1.5 Tables and Figures

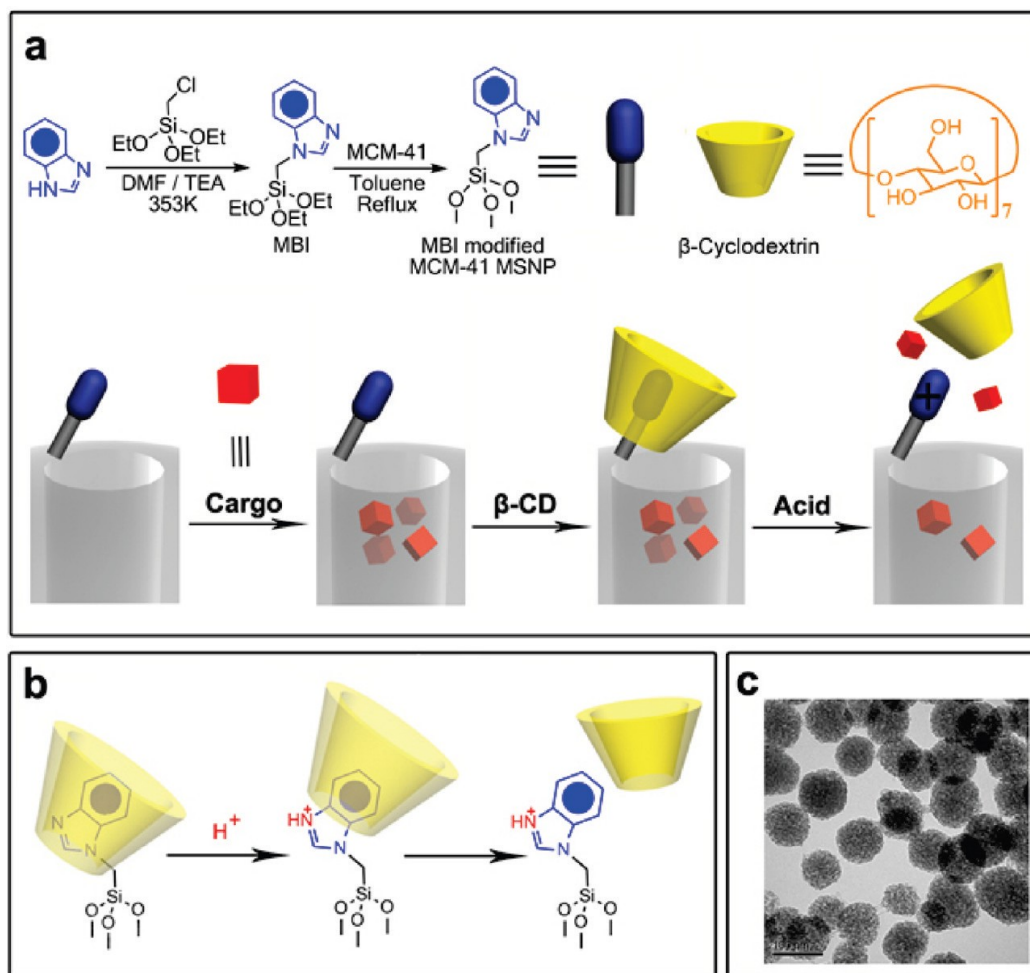


Figure 1.1. A graphical representation of the pH responsive MSNP nanovalve. **(a)** Synthesis of the stalk, loading of the cargo, capping of the pore, and release of the cap under acidic conditions. Based on our calculations,¹⁵ the maximum number of stalks per nanopore is 6, and the maximum number of fully assembled nanovalves per nanopore is 4. The average nanopore diameter of the MSNP is around 2.2 nm, and the periphery diameter of the secondary side of β -cyclodextrin is ~ 1.5 nm. Thus, for a cargo with diameter >0.7 nm, a single nanovalve should be adequate to achieve effective pH-modulated release. **(b)** Details of the protonation of the stalk and release of the β -cyclodextrin. **(c)** TEM image of capped MSNP. The scale bar is 100 nm.

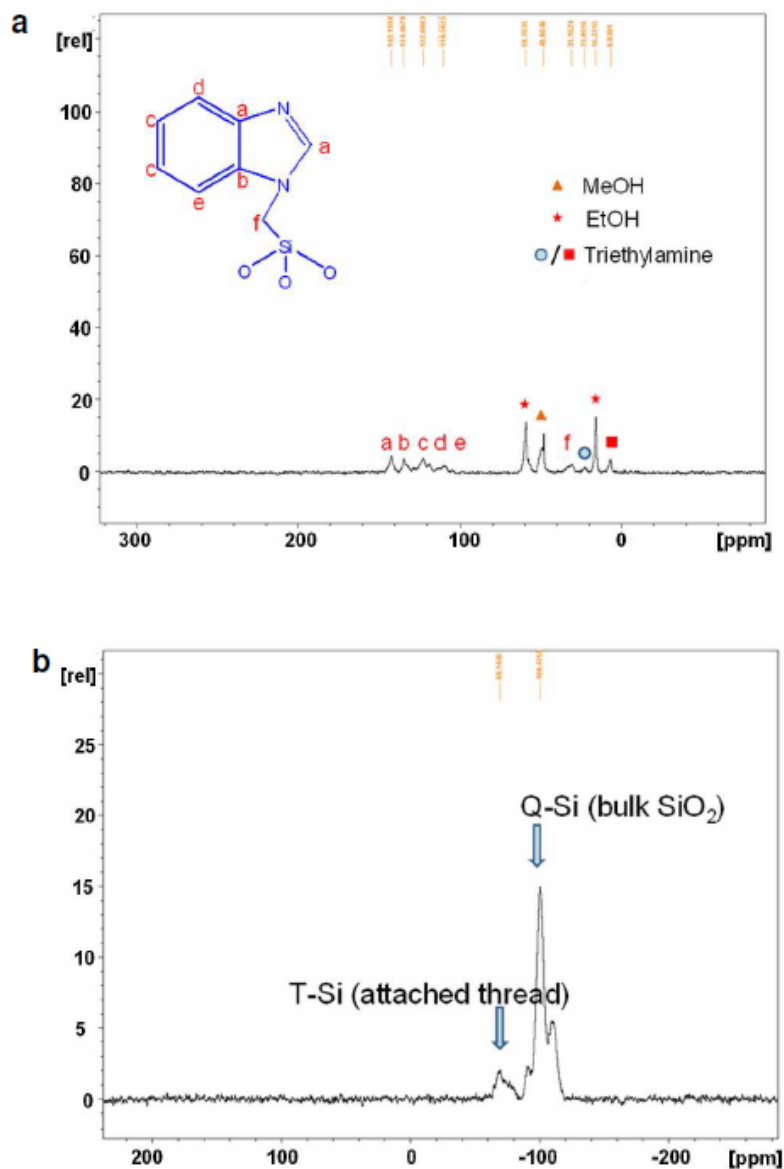


Figure 1.2. ^{13}C -CPMS NMR and ^{29}Si -CPMS NMR spectra of MBI MSNP. The spectrum was collected on a DSX300 NMR spectrometer (Bruker, 300 MHz), using a 4 mm CP/MAS probe at room temperature. **(a)** ^{13}C -CPMS NMR spectra for the MBI-MSNP particles. All the peaks are assigned as shown in the figure. The data illustrate that benzimidazole is bonded to the silica surface. The particle alone did not show peaks in the aromatic region. **(b)** ^{29}Si -CPMS NMR spectra for the MBI-MSNP showing the bulk silica band and attached thread (containing Si-C bond) band, proving the attachment of the MBI compound.

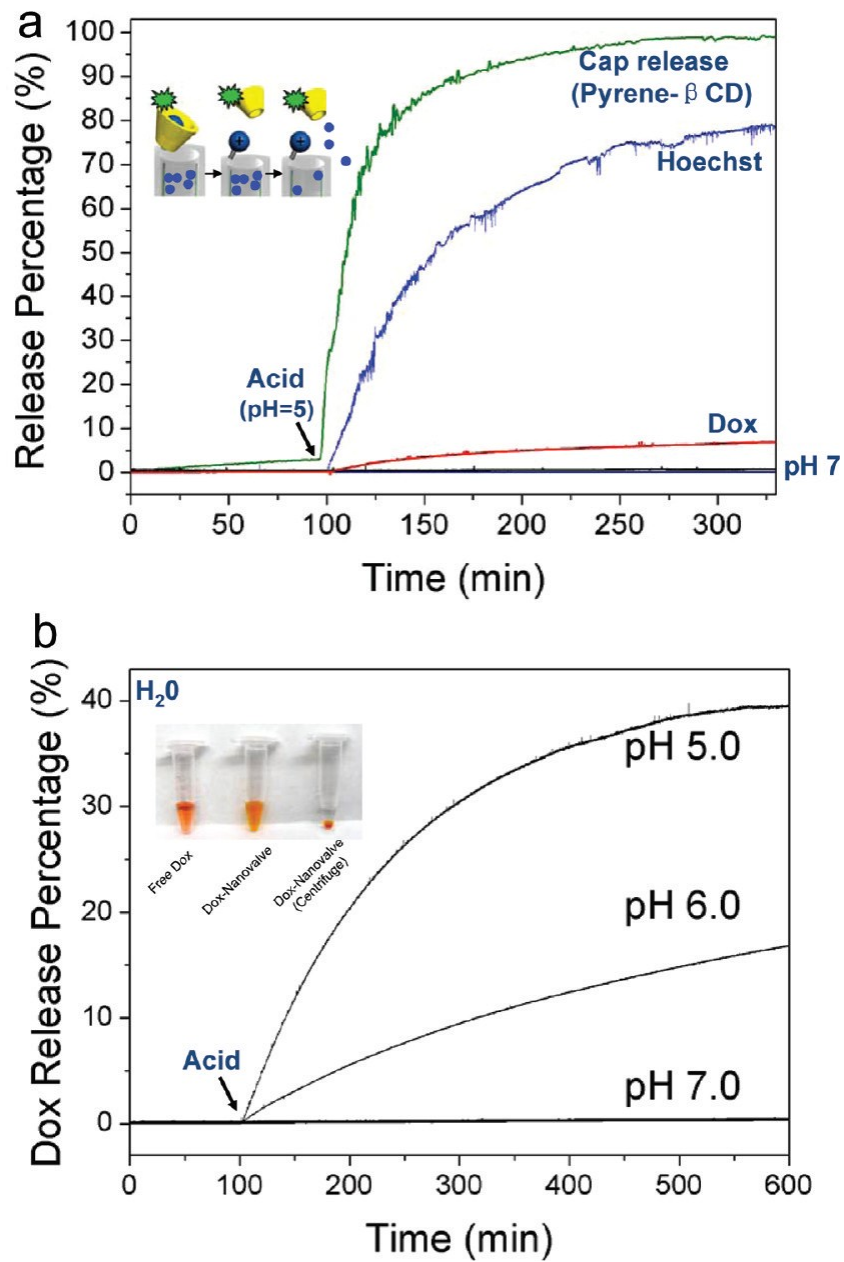


Figure 1.3. Release profiles of cargo molecules and the cyclodextrin. **(a)** Fluorescence intensity plots for the release of Hoechst dye, doxorubicin and the pyrene-labeled cyclodextrin cap released from MSNP containing –OH surface (Si-OH). **(b)** Release profiles of doxorubicin from ammonium modified (7.5%, w/w) particles showing the faster and larger response compared to the unmodified MSNP (**Figure 1.2a**).

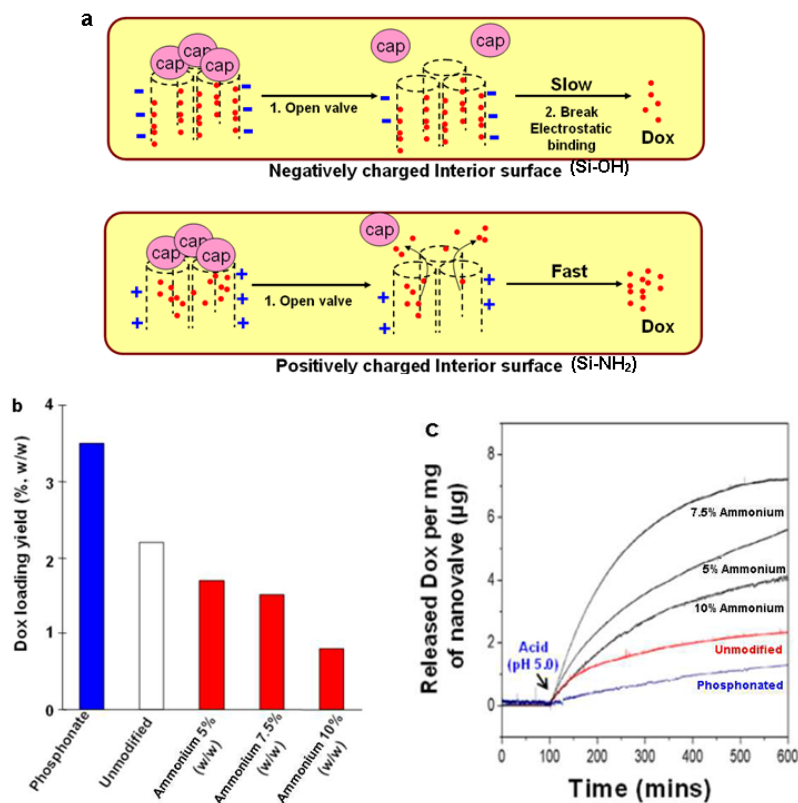


Figure 1.4. Ammonium attachment to the MSNP surface accelerates doxorubicin release. **(a)** Scheme showing that a positively charged silica porous surface is capable of accelerating doxorubicin release. **(b)** The drug loading capacity in accordance with the ammonium density while negatively charged surface assist electrostatic retention. **(c)** Release profiles of surface modified MSNP demonstrate that the 7.5% (w/w) amine modification increases doxorubicin release while maintaining appreciable loading. By comparison, a negatively charged surface shows the highest loading capacity but significantly reduces the rate of doxorubicin release. The 7.5% ammonium modified nanoparticle was chosen as the best compromise for subsequent experiments.

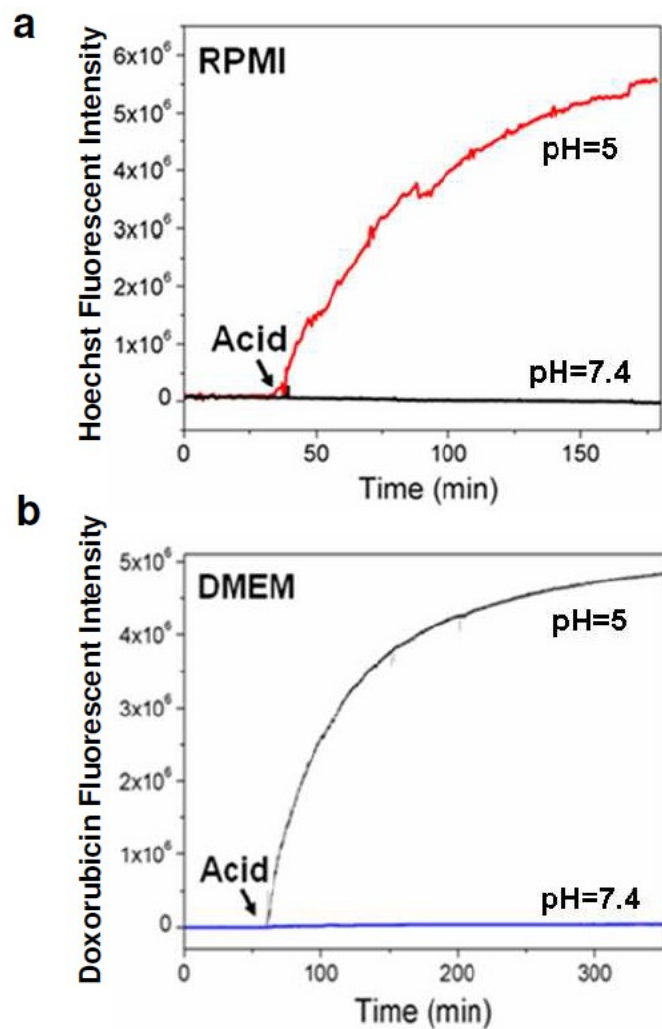


Figure 1.5. (a) Release profile of Hoechst loaded nanovalve MSNP in RPMI medium at pH 5. No release was found at pH 7.4. **(b)** Release profile of doxorubicin loaded nanovalve MSNP in DMEM medium at pH 5. No detectable was seen at pH 7.4.

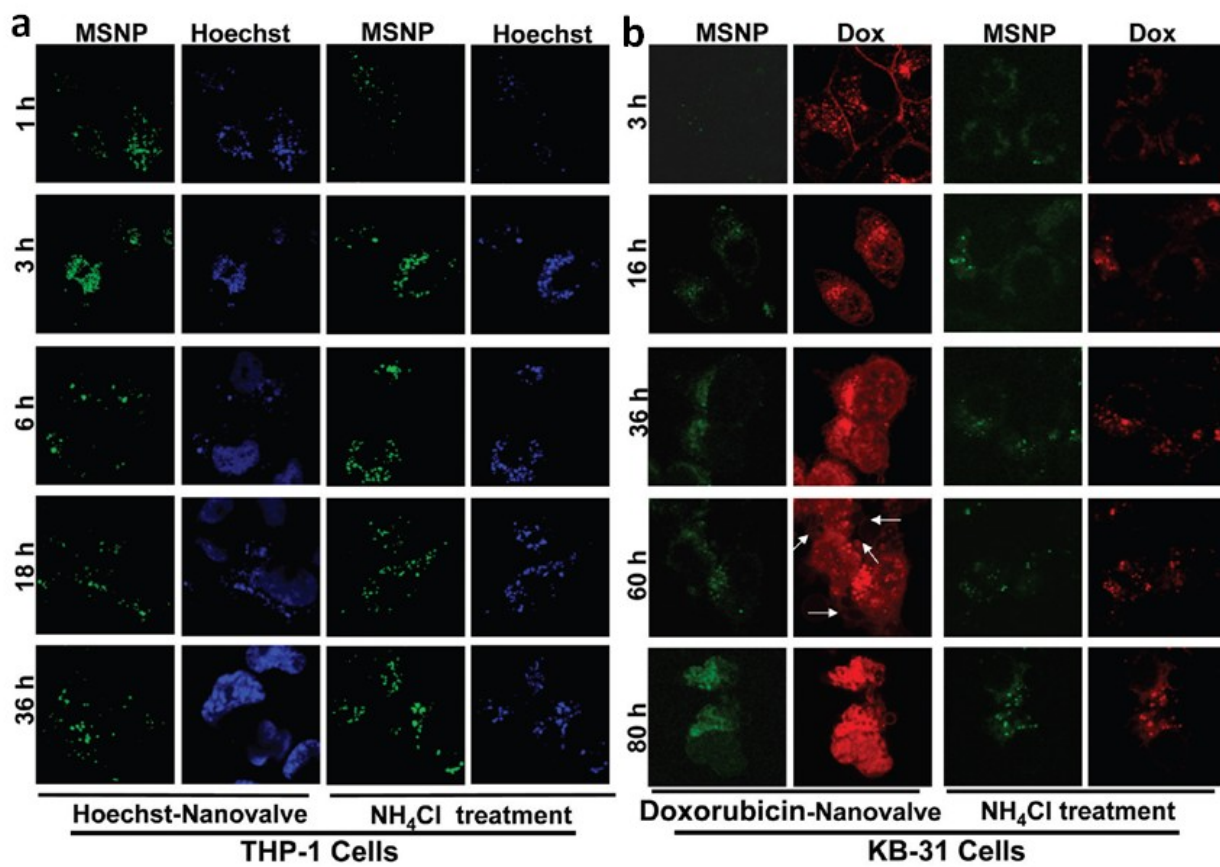


Figure 1.6. Confocal images of THP-1 and KB-31 cells incubated with MSNP containing Hoechst dye and doxorubicin drug for the indicated times. **(a)** Hoechst-loaded, FITC-labeled MSNP. **(b)** Doxorubicin-loaded, FITC-labeled MSNP.

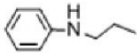
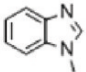
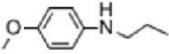
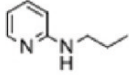
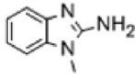
Stalk	^a pK _a	Releasing pH	Cap
	5.04	< 5.0	α-CD
	^b 5.67	< 6.0	β-CD
	5.89	< 6.0	α-CD
	6.41	< 7.0	α-CD
	7.66	< 8.0	β-CD

Table 1.1. Optimization of the operational pH conditions of MSNP fitted with different stalks to define physiologically responsive nanovalves. **a**, The pK_a values were calculated by Advanced Chemistry Development (ACD/Labs) Software V8.14 for Solaris (©1994-2010 ACD/Labs). **b**, The pK_a of MBI-β-CD is highlighted in red and represents the stalk chosen for the reported experiments. The release pH increases as the pK_a value of the aromatic group chosen for the stalk goes up. Biocompatible MBI was chosen because the nanovalves are closed tightly in neutral condition but self-open in acidifying endosomal compartments.

1.7 References

1. (a) Kresge, C. T.; Leonowicz, M. E.; Roth, W. J.; Vartuli, J. C.; Beck, J. S. *Nature* **1992**, *359*, 710-712. (b) Cai, Q.; Luo, Z. S.; Pang, W. Q.; Fan, Y. W.; Chen, X. H.; Cui, F. Z. *Chem. Mater.* **2001**, *13*, 258-263. (c) Lai, C.-Y.; Trewyn, B. G.; Jeftinija, D. M.; Jeftinija, K.; Xu, S.; Jeftinija, S.; Lin, V. S. Y. *J. Am. Chem. Soc.* **2003**, *125*, 4451-4459.
2. (a) Vallet-Regí, M.; Francisco, B.; Daniel, A. *Angew. Chem. Int. Ed.* **2007**, *46*, 7548-7558. (b) Angelos, S.; Johansson, E.; Stoddart, J. F.; Zink, J. I. *Adv. Funct. Mater.* **2007**, *17*, 2261-2271. (c) Xia, T.; Kovochich, M.; Liong, M.; Meng, H.; Kabehie, S.; George, S.; Zink, J. I.; Nel, A. E. *ACS Nano* **2009**, *3*, 3273-3286.
3. (a) Cotí, K. K.; Belowich, M. E.; Liong, M.; Ambrogio, M. W.; Lau, Y. A.; Khatib, H. A.; Zink, J. I.; Khashab, N. M.; Stoddart, J. F. *Nanoscale* **2009**, *1*, 16-39. (b) Trewyn, B. G.; Slowing, I. I.; Giri, S.; Chen, H. T.; Lin, V. S. Y. *Acc. Chem. Res.* **2007**, *40*, 846-853. (c) Slowing, I. I.; Trewyn, B. G.; Giri, S.; Lin, V. S.-Y. *Adv. Funct. Mater.* **2007**, *17*, 1225-1236. (d) Slowing, I.; Vivero-Escoto, J.; Wu, C.-W.; Lin, V. *Adv. Drug Deliv. Rev.* **2008**, *60*, 1278-1288.
4. (a) Zhu, Y. F.; Shi, J. L.; Shen, W. H.; Dong, X. P.; Feng, J. W.; Ruan, M. L.; Li, Y. S. *Angew. Chem. Int. Ed.* **2005**, *44*, 5083-5087. (b) Zhu, C.-L.; Song, X.-Y.; Zhou, W.-H.; Yang, H.-H.; Wen, Y.-H.; Wang, X.-R. *J. Mater. Chem.* **2009**, *19*, 7765-7770. (c) Andrew MacKay, J.; Chen, M.; McDaniel, J. R.; Liu, W.; Simnick, A. J.; Chilkoti, A. *Nat. Mater.* **2009**, *8*, 993-999.
5. (a) Lu, J.; Choi, E.; Tamanoi, F.; Zink, J. I. *Small* **2008**, *4*, 421-426. (b) Patel, K.; Angelos, S.; Dichtel, W. R.; Coskun, A.; Yang, Y. W.; Zink, J. I.; Stoddart, J. F. *J. Am. Chem. Soc.* **2008**, *130*, 2382-2383. (c) Nguyen, T. D.; Leung, K. C. F.; Liong, M.; Pentecost, C. D.; Stoddart, J. F.; Zink, J. I. *Org. Lett.* **2006**, *8*, 3363-3366. (d) Angelos, S.; Yang, Y. W.; Patel, K.; Stoddart, J. F.; Zink, J. I. *Angew. Chem. Int. Ed.* **2008**, *47*, 2222-2226. (e) Du, L.; Liao, S.; Khatib, H. A.; Stoddart, J. F.; Zink, J. I. *J. Am. Chem. Soc.* **2009**, *131*, 15136-15142. (f)

- Angelos, S.; Khashab, N. M.; Yang, Y. W.; Trabolsi, A.; Khatib, H. A.; Stoddart, J. F.; Zink, J. I. *J. Am. Chem. Soc.* **2009**, *131*, 12912-12914. (g) Liu, R.; Zhang, Y.; Zhao, X.; Agarwal, A.; Mueller, L. J.; Feng, P. *J. Am. Chem. Soc.* **2010**, *132*, 1500-1501.
6. May, B. L.; Kean, S. D.; Easton, C. J.; Lincoln, S. F. *J. Chem. Soc. Perkin Trans. 1* **1997**, 3157-3160.
7. (a) Ohkuma, S.; Poole, B. *Proc. Natl. Acad. Sci. U.S.A.* **1978**, *75*, 3327-3331. (b) Cardelli, J. A.; Richardson, J.; Miers, D. *J. Biol. Chem.* **1989**, *264*, 3454-3463.
8. (a) Ling, H.; Vamvakas, S.; Gekle, M.; Schaefer, L.; Teschner, M.; Schaefer, R. M.; Heidland, A. *J Am. Soc. Nephrol.* **1996**, *7*, 73-80. (b) Ling, H.; Ardjomand, P.; Samvakas, S.; Simm, A.; Busch, G. L.; Lang, F.; Sebekova, K.; Heidland, A. *Kidney Int.* **1998**, *53*, 1706-1712.
9. (a) Masaru, H.; Shotaro, S.; Masao, Y.; Motoaki, K.; Masahito, O.; Satoshi, S.; Yoshihiro, M.; Kazunori, N.; Michio, S.; Kyuichi, T. *J. Hepatol.* **1996**, *24*, 594-603. (b) Yoshimori, T.; Yamamoto, A.; Moriyama, Y.; Futai, M.; Tashiro, Y. *J. Biol. Chem.* **1991**, *266*, 17707-17712.
10. Gagliardi, S.; Gatti, P. A.; Belfiore, P.; Zocchetti, A.; Clarke, G. D.; Farina, C. *J. Med. Chem.* **1998**, *41*, 1883-1893.
11. Gavrieli, Y.; Sherman, Y.; Ben-Sasson, S. A. *J. Cell Biol.* **1992**, *119*, 493-501.
12. Database of Chemical Safety Information from Intergovernmental Organizations: <http://www.inchem.org/documents/jmpr/jmpmono/v073pr11.htm>.
13. (a) Leroux, J.-C.; Cozens, R. M.; Roesel, J. L.; Galli, B.; Doelker, E.; Gurny, R. *Pharm. Res.* **1996**, *13*, 485-487. (b) Dai, J.; Nagai, T.; Wang, X.; Zhang, T.; Meng, M.; Zhang, Q. *Int. J. Pharm.* **2004**, *280*, 229-240. (c) Bae, Y.; Jang, W.-D.; Nishiyama, N.; Fukushima, S.; Kataoka, K. *Mol. Biosyst.* **2005**, *1*, 242-250.
14. (a) Dianxiang, L.; Xiantao, W.; Jie, L.; Zhongwei, G.; Xingdong, Z.; Yujiang, F. *J. Biomed. Mater. Res. Part B Appl. Biomater.* **2009**, *89B*, 177-183. (b) Yang, Y.-J.; Tao, X.; Hou, Q.; Ma, Y.; Chen, X.-L.; Chen, J.-F. *Acta Biomater.* **2010**, *6*, 3092-3100. (c) Bae, Y.; Nishiyama,

N.; Kataoka, K. *Bioconjugate Chem.* **2007**, *18*, 1131-1139. (d) Lee, E. S.; Gao, Z.; Kim, D.; Park, K.; Kwon, I. C.; Bae, Y. H. *J. Control. Release* **2008**, *129*, 228–236.

15. The average hydroxyl coverage for silica nanoparticles and gels equals 4.9 OH/ nm² (Zhuravlev, L. T. *Langmuir*, **1987**, *3*, 316–318). This value corresponds closely to the value expected if, on average, the amorphous silica surface is represented by the <111> face of cristobalite (Brinker, C. J.; Scherer, G. W. *Sol-Gel Science* **1990**, Elsevier Science, USA, p.624). Based on this model, the distance between two surface OH groups is 5.3 Å. Thus, the number of surface OH groups around one nanopore (nanopore diameter 2.2 nm) is 13. Since the attachment of one stalk on the nanopore requires at least 2 OH groups on the nanopore perimeter, the maximum number of stalks that can become attached to one nanopore is about 6. For a fully assembled nanovalve, the size depends on the β-cyclodextrin – the periphery diameter of the secondary side is ~1.5 nm (Szejtli, J. *Chem. Rev.* **1998**, *98*, 1743–1754); thus, the maximum number of nanovalves per nanopore opening is about 4.

Chapter 2

pH-Operated Mechanized Porous Silicon Nanoparticles

2.1 Abstract

Porous silicon nanoparticles (PSiNPs) were synthesized by a silver-assisted electroless chemical etching of silicon nanowires generated on a silicon wafer. The rod-shaped particles (200-400 nm long and 100-200 nm in diameter) were derivatized with a cyclodextrin based nanovalve that is closed at physiological pH 7.4 but open at pH<6. Release profiles in water and tissue culture media show that no cargo leaks when the valves are closed and that release occurs immediately after acidification. In vitro studies using human pancreatic carcinoma PANC-1 cells proved that these PSiNPs are endocytosed and carry cargo molecules into the cells and release them in response to lysosomal acidity. These studies show that PSiNPs can serve as an autonomously functioning delivery platform in biological systems and open new possibilities for drug delivery.

I would like to acknowledge Mr. Xing Zhong for the assistance of generating silicon nanoparticles and Dr. Zory Shaposhnik for the *in vitro* biological studies.

2.2 Introduction

Porous silicon-based materials are attracting much recent interest for bio-applications including sensing, imaging and drug delivery.¹⁻⁶ Particles of porous silicon with attractive properties of high surface area,^{7,8} intrinsic luminescence and bio-degradability^{1a,2-4,11} have become a very promising scaffold for delivering drugs. Polymer-coated porous silicon nanoparticles (PSiNPs) have been shown to be an effective chemotherapeutic drug delivery system.^{1a} The method for drug transportation in these studies was based on the electrostatic interaction and/or physical adsorption of specific drugs to the particles.¹⁻⁴ A key challenge for drug delivery applications is to utilize and control the access to the pores of the PSiNPs in order to generate a stimulus-responsive system that can transport and release the payload on demand without premature release. Similar efforts on mesoporous silica nanoparticles (MSNPs) have led to the development of molecular nanovalves that control the pore openings.⁹ Because the surface of the PSiNPs is usually terminated with a native silica layer, it is reasonable to expect that nanovalve-controlled systems similar to those that have been developed on silica nanoparticles can also be adapted onto the PSiNP platform. In this chapter, I demonstrate the first example of a mechanized PSiNPs system with access to the pore structure controlled by nanovalves chemically bonded on the surface of the PSiNPs. I further show that these PSiNPs can be used as an in vitro delivery system to the human pancreatic carcinoma PANC-1 cells where the cargo is confined in the particles at pH 7.4 and released only on exposure to the decreased pH in endocytic vesicles.

2.3 Experimental

Synthesis of PSiNPs. Silicon wafers with a resistivity of 0.008-0.02 $\Omega\cdot\text{cm}$ were pre-cleaned with water, acetone and isopropanol. The native oxide layer on the silicon was removed by immersing the wafer into a buffered oxide etchant (BOE), leading to a hydrogen (H)-terminated surface. The porous silicon nanowires were then prepared by Ag coating followed by the etching

in an etchant solution containing HF and H₂O₂ for 60 minutes. The Ag nanoparticles were removed by soaking the samples into concentrated nitric acid for one hour. The porous silicon nanowires were then separated and suspended in methanol via sonication. The porous silicon nanowires were fragmented into PSiNPs by strong sonication (70 W, 42 kHz) for 2 hours. After the sonication, PSiNPs with different size were collected by filtering the suspension with 800 nm, 450 nm and 220 nm membrane filter. In this study, PSiNPs with a size range of < 450 nm were chosen for subsequent studies.

Grafting of Nanovalves. 20 mg of PSiNPs were suspended in 1 ml of absolute ethanol, followed by the addition of 5 μ l of 3-Iodopropyltrimethoxysilane (IPTMS, 90%, Gelest). The solution was stirred under inert atmosphere at 60 °C for 10 hrs. The IPTMS-modified PSiNPs were then collected via centrifugation and washed with ethanol. Then, the PSiNPs were re-suspended in 2 ml of anhydrous DMF, in which 20 mg of benzimidazole (98%, Fluka) and 20 μ l of *N,N*-diisopropylethylamine (99.5%, Sigma) were added. The solution was stirred at 70 °C under inert atmosphere for 24 hrs. The PSiNP-PBI were collected via centrifugation and washed with DMF and H₂O.

Fluorescent Labeling of PSiNP-PBI. 0.5 mg of fluorescein isothiocyanate (FITC, 90%, Sigma) was mixed with 1 μ l of *N*-(2-aminoethyl)-3-aminopropyltrimethoxysilane (90%, Gelest) in 1 ml of absolute ethanol. The solution was stirred under N₂ for 2 hrs. 20 mg of PSiNP-PBI were suspended in 1 ml of absolute ethanol, and mixed with the FITC ethanol solution. The mixture was stirred at 60 °C for 10 hrs. The resulted nanoparticles were centrifuged and washed with ethanol and H₂O.

Loading of Hoechst 33342. 20 mg of PSiNPs-PBI were mixed with 1 ml of Hoechst 33342 (Sigma) in aqueous solution (1 mM). The suspension was stirred for 12 hrs before β -cyclodextrin (40 mg) was added. The mixture was stirred for another 12 hrs, and the

nanoparticles were centrifuged and washed with H₂O. The content of Hoechst in the washing solution was monitored by UV-vis spectrometer and fluorescence spectrometer to ensure the maximal removal of surface associated dye molecules. The pH value of the loading and washing solution was also closely monitored by a pH meter so that the nanovalve should not open during these processes.

Release Studies. The release profiles were obtained by time-resolved fluorescence spectroscopy, as previously described (Reference 9c-9f from the manuscript). Briefly, a probe beam (377 nm, 20 mW) was directed into the water or DMEM cell culture medium to excite the dissolved Hoechst molecules. The luminescence spectrum of the dissolved cargo was collected in 1 sec intervals over the course of the experiment. Acetic acid was added to decrease the pH to desired value. The luminescence intensity at the emission maximum of the dye was plotted as a function of time to generate a release profile.

Characterization of PSiNPs. The as-prepared silicon nanowires were characterized by scanning electron microscopy (SEM JEOL 6700) and transmission electron microscopy (TEM, CM120). The nanoparticle sizes were measured by ZetaSizer Nano (Malvern Instruments Ltd., Worcestershire, UK). N₂ adsorption-desorption experiment was performed on QuadraSorb SI (Quantachrome Instruments). The C-13 CPMAS NMR spectrum was collected on a DSX300 NMR spectrometer (Bruker, 300 MHz), using a 4 mm CPMAS probe at room temperature.

Cell Culture. Human pancreatic cancer PANC-1 cells grown in DMEM supplemented with 10% FBS were seeded overnight into 8 well chamber slides (Nalge Nunc International). FITC-Hoest containing PSiN and unlabeled PSiN dissolved in water were sonicated briefly prior to being added to cells for five hours at 37 °C or 4 °C. To demonstrate that PSiNP uptake occurs via an energy dependant process such as endocytosis or phagocytosis, one group of cells was pre-incubated at 4 °C for 30 minutes prior to PSiNP addition and subsequent incubation for another

5 hours at that temperature. Cells were washed three times in PBS and fixed in 1% PFA for 10 minutes prior to mounting in 50% glycerol and imaging by confocal microscopy.

2.4 Results and Discussion

Traditionally, porous silicon is produced by applying a voltage bias to a silicon wafer in hydrofluoric acid containing solutions.¹⁰ In this study, the rod-like PSiNPs were prepared from breaking down porous silicon nanowires (PSiNWs), that were generated on a silicon wafer via a Ag-assisted electroless chemical etching method.⁸ Currently, several mechanisms have been proposed to explain the porosification process.^{8c,11,12} The mechanism we suggested here is based on previous work^{8c} and schematically illustrated in Figure 2.1A. Silver nanoparticles, which were pre-deposited on the silicon wafer (Figure 2.1A1), will etch pits down into the wafer. The nanowires were consequently formed as the result of the pit walls left between particles. In the process, the Ag nanoparticles at the bottom of these pits can re-dissolve in the etching solution, diffuse up and nucleate again (Figure 2.1A2-1A3) on the sidewalls of the as-formed silicon nanowires, serving as a new etching site and generating the pores (Figure 2.1A4). By using this method, PSiNWs can be generated without external electricity, and the nanowire lengths as well as their pore sizes can be easily tuned by controlling the reaction time and conditions.^{8c} Figure 2.1B displays the cross sectional SEM image of an as-prepared PSiNW array on the substrate. The length of the nanowires is around 30 μm . The nanowires were separated from the substrate and broken into small fragments to form PSiNPs via sonication (Figure 2.1A5). PSiNPs with different sizes were then separated by using filtration membranes. The size chosen for this study was between 200-400 nm, which is suitable for conducting *in vitro* studies. Figure 2.1C shows the TEM image of PSiNPs after sonication, from which their average length is estimated to be about 300 nm, in agreement with the result obtained from dynamic light scattering measurements (Figure 2.2). The pore structure can be clearly observed via HR-TEM (Figure 2.1C inset). N_2 adsorption-desorption analysis gives a BET surface area of

293 m²/g and a pore volume of 0.98 cc/g, consistent with a previous report.^{8c} These PSiNPs exhibit a relatively wide pore size distribution (Figure 2.3) due to the variable sizes of the nucleated Ag nanoparticles on the sidewall of the silicon nanowires.

In this study, a well-established pH-responsive nanovalve-system consisting of an aromatic amino group and a cyclodextrin cap^{9d,9f} was chosen to be adapted to the PSiNPs. This nanovalve was shown to be tightly closed under physiological pH (pH 7.4) and to open autonomously under acidic conditions (pH<6) present in endosomal/lysosomal vesicles. In order to attach the nanovalves, The PSiNPs were first derivatized with 3-iodopropyltrimethoxy-silane and then coupled with a benzimidazole molecule under base catalysis (Figure 2.4). Solid state NMR spectrum proves that the modification was successful (Figure 2.5). The modified PSiNPs exhibit a BET surface area of 282 m²/g and a pore volume of 0.95 cc/g, which is similar to those before modification.

In order to demonstrate the operation of the nanovalves, the fluorescent biological staining dye Hoechst 33342 was chosen as a model cargo. The PSiNPs were loaded with the dye by soaking them in a concentrated Hoechst 33342 solution. β -cyclodextrin was then added into the solution to finish the full assembly of the nanovalves, followed by washing with water to remove dye molecules absorbed on the nanoparticles' exteriors. Under neutral pH conditions, the benzimidazole stalk remains hydrophobic and therefore can bind to the cyclodextrin molecule via supramolecular interactions. By doing this, the bulky cyclic cyclodextrin molecules block the pore openings and function as gate keepers to prevent the cargo in the pore from leaking out. When the pH is lowered, the benzimidazole is protonated, and the binding constant between the stalk and the cyclodextrin drops dramatically, causing the cyclodextrin to dissociate. After the pores are unblocked, the cargo can diffuse out (Figure 2.4).

In order to verify the functional operation of the nanovalves, the cargo-loaded PSiNPs were placed in water and the pH was lowered to stimulate the opening of the nanovalves. The

fluorescence intensity of the model cargo Hoechst 33342 dye under different concentrations and pH values is shown in Figure 2.6, which proves that Hoechst 33342 is a suitable model molecule for this study. The increased concentration of cargo dye released into the aqueous solution was monitored as a function of time by fluorescence spectroscopy to generate a release profile (Figure 2.7A). Similar to the behavior in the case of silica nanoparticles,^{9f} these nanovalves on silicon nanoparticles remain tightly closed at pH 7.0, giving a flat baseline as illustrated in Figure 2.6A. Upon lowering the pH, the nanovalves opened and the cargo was released. Cargo release was completed in about 3 hr, which is much faster than that in the case of MCM-41. As a control experiment, PSiNPs with stalks but without capping components were used. In this case, all of the cargo should be removed from PSiNPs during washing. The flat profile for these PSiNPs observed upon acidification shows that no cargo was released as expected (Figure 2.7A). The release of cargo molecules at different pH values is shown in Figure 2.8, where the release rate increases when the solution was adjusted to be more acidic.

The loading capacity of these PSiNPs is dependent on the size of the cargo. In the case of Hoechst, a loading capacity of 1% w/w was determined using UV-vis absorption spectroscopy. This relatively low value is due to the small size of the Hoechst molecules. The nanovalve on the PSiNPs has a size of about 1.5 nm, thus is only capable of controlling the release of Hoechst from < 5.5 nm sized pores.¹³

Before conducting *in vitro* studies, it is important to verify that the nanovalve-modified PSiNPs remain functional in biological conditions where the large amount of buffering salt and proteins could potentially change the behavior of the nanovalves. In order to address this point, release profiles were generated in a DMEM cell culture medium with 10% FBS, using Hoechst-loaded PSiNPs (Figure 2.7B). The PSiNPs were stable in the cell culture medium for at least 5 hr, as no cargo leakage was observed. When the pH was lowered, the fluorescence intensity increased over time, indicating that the valves opened and released cargo. This result

demonstrates that the nanovalve-modified PSiNPs are stable, functional and suitable for utilization as a drug delivery system.

Human pancreatic carcinoma PANC-1 cells were studied in order to prove that the nanovalve-modified PSiNPs can be taken up by cells and deliver their cargo inside them. The cells were incubated at 37 °C with the fluorescein-labeled PSiNPs that were loaded with Hoechst 33342. Figure 2.9A shows that after incubation for three hours, the Hoechst dye was released and stained the cell nucleus. This process is relatively fast and is consistent with the abiotic release profile. In order to further prove that it is the endocytosed PSiNPs that opened and released the dye, several control experiments were conducted. First, the cells were incubated at 4 °C, where the energy-dependant endocytosis pathway is inactive, with the same amount of PSiNPs. In principle, if it is the nanovalves that control the release of the dye, then non-endocytosed PSiNPs should not stain the cells because they do not experience a pH change. As shown in Figure 2.9B, no staining was observed after 3 hrs' incubation at low temperature, proving that the dye is not released. Furthermore, contact between PSiNPs and the cell membrane does not cause the nanovalves to open. This result also suggests that the endocytosis process is necessary for opening the nanovalves. Secondly, in order to further investigate the functioning of the mechanized PSiNPs, a competition experiment was conducted. The cells were treated with the same amount of Hoechst-loaded FITC-labeled PSiNPs and increasing amounts of plain PSiNPs with no payload or FITC-labeling. If the particles are indeed taken up primarily via a specific energy dependant uptake process, the amount of FITC-labeled particle uptake (and nuclear staining) should decrease as the concentration of unlabelled particles increases. Figure 2.9C and 2.9D prove this assumption by showing much less FITC signal along with less nuclear staining. This result demonstrates that the nanovalves on the PSiNPs do not open in cell culture medium at 37 °C, and also proves that the endocytosis

process is necessary to enable the particles to reach lysosomes and trigger the release of the cargo.

2.5 Summary

In summary, it has been demonstrated that pH-sensitive nanovalves can be successfully grafted onto the surface of PSiNPs and function as valves to control the pore openings. These mechanized PSiNPs are endocytosed and release their cargo molecules inside the cells.

2.6 Figures

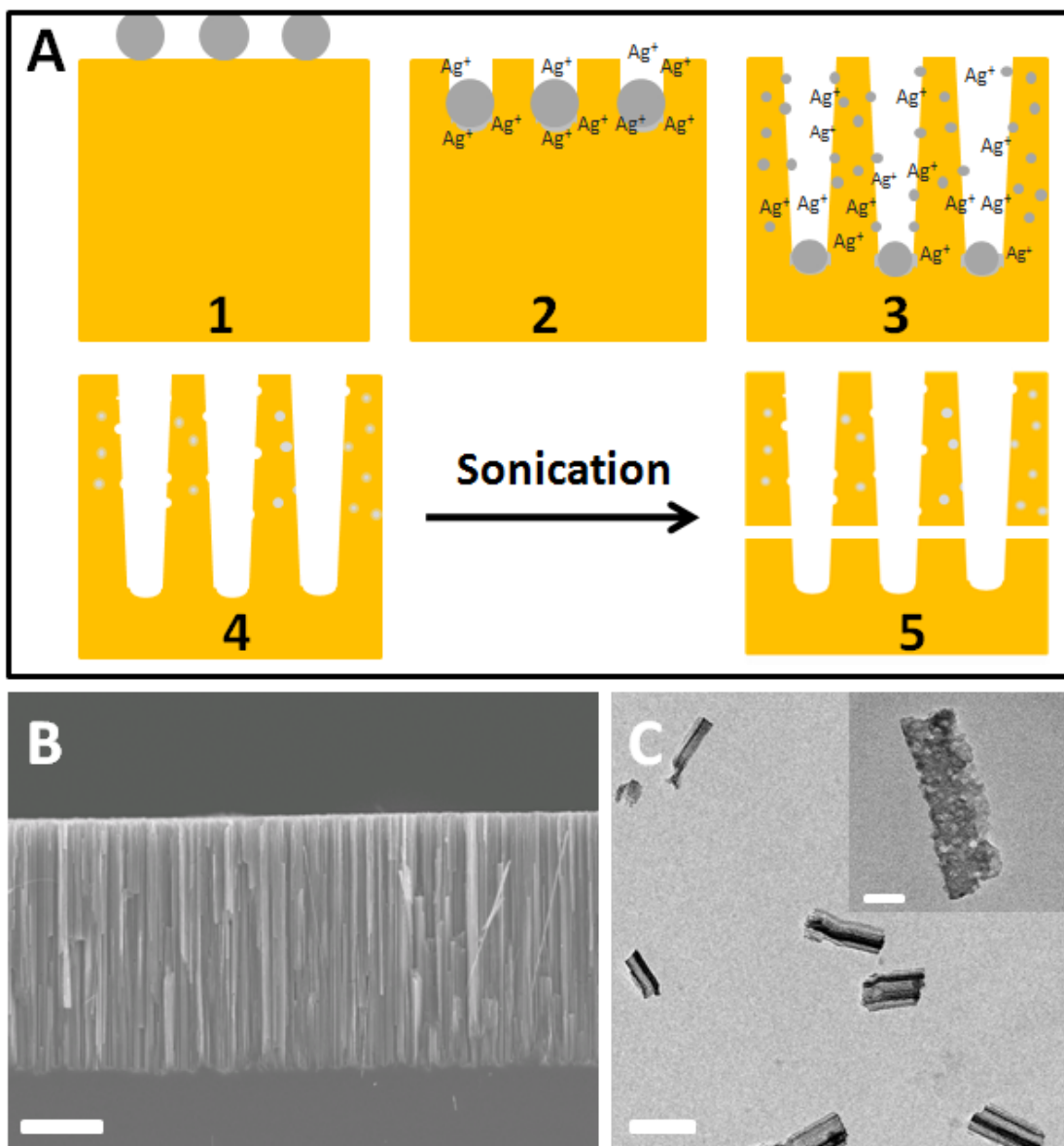


Figure 2.1. (A) The generation of porous silicon nanowires by the etching process with silver nanoparticles. (B) Cross sectional SEM image of a porous silicon nanowire array on the substrate. The scale bar is 10 μm . (C) TEM image of the PSiNPs after sonication and filtration. The scale bar is 300 nm. A high resolution TEM image of a PSiNP is displayed as an inset with a scale bar of 50 nm.

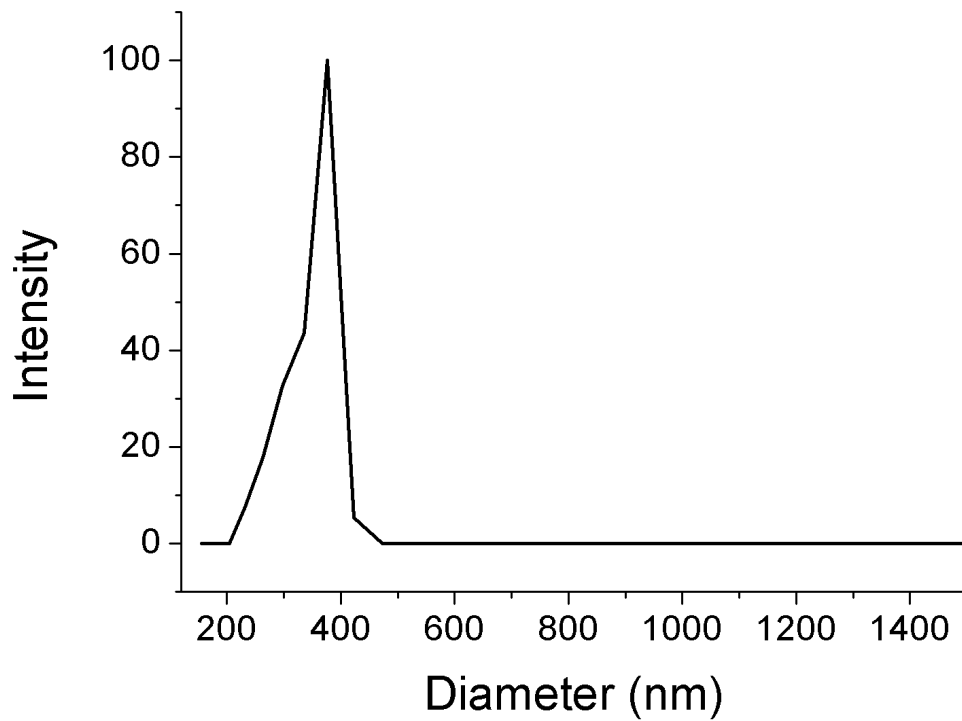


Figure 2.2. Dynamic light scattering result of PSiNPs in aqueous suspension. The non-symmetric distribution is due to the rod-like shape of the PSiN nanoparticles. The effective hydrodynamic size of the PSiN is calculated to be 320 nm,

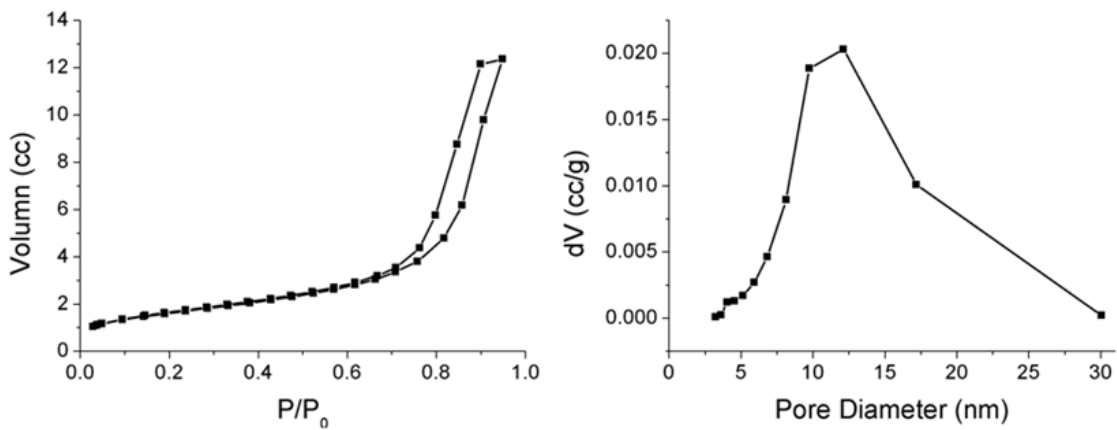


Figure 2.3. (Left) N_2 adsorption-desorption isotherms of the PSiN. The hysteresis indicates the existence of the pore. **(Right)** Pore diameter calculated from the desorption isotherm using BJH method. The relatively wide pore size distribution is consistent with the pore forming mechanism, where re-nucleated Ag nanoparticles vary in size.

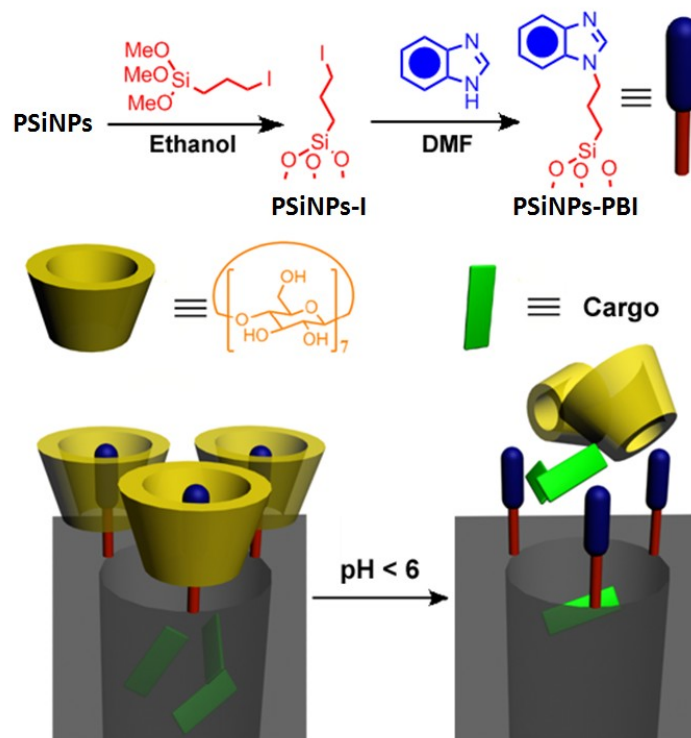


Figure 2.4. Schematic illustration of the synthesis and operation mechanism of the nanovalve. **(Top left)** Attachment of the stalk precursor to the nanoparticle. **(Top right)** Completion of the synthesis of the stalk. **(Bottom)** Binding of β -cyclodextrin cap to the neutral stalk (left) and release of the cap upon protonation of the stalk.

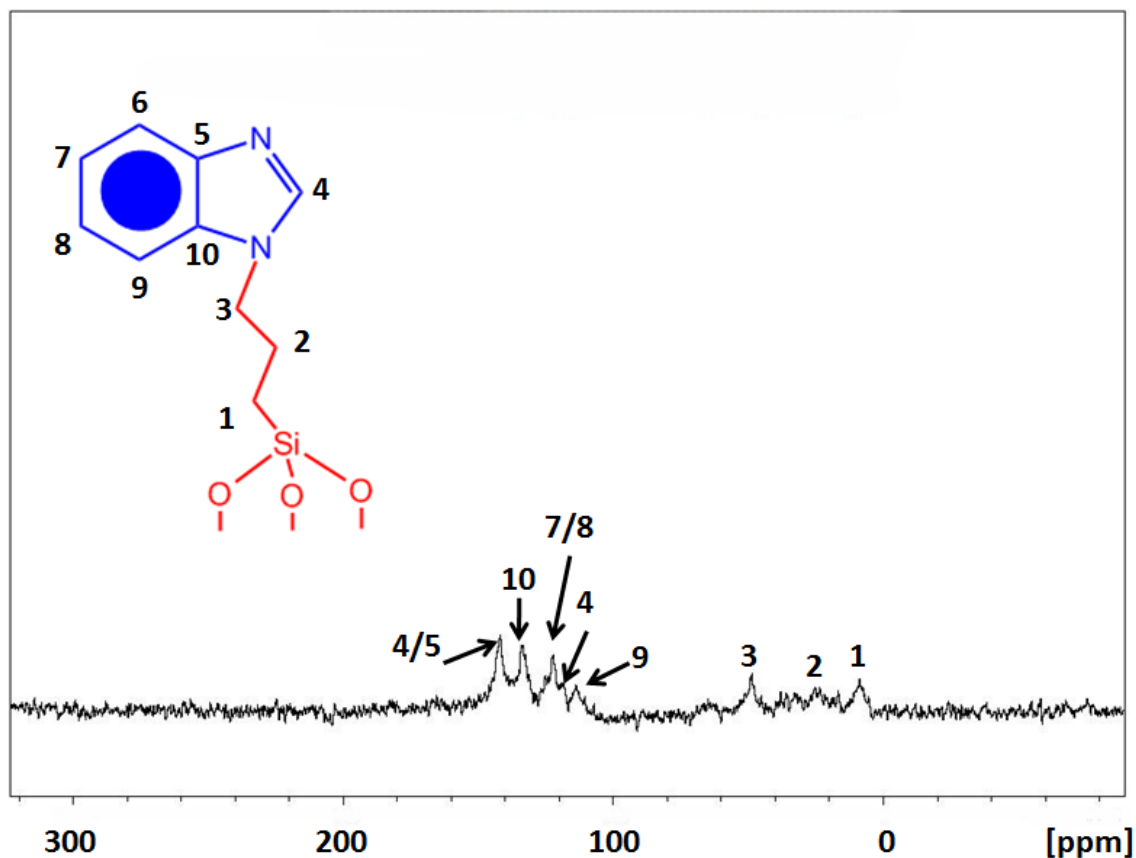


Figure 2.5. C-13 CPMAS NMR spectrum of nanovalve-modified PSiNPs. The peaks are assigned as indicated in the figure. During the synthesis, any absorbed or unreacted compounds will be removed from the PSiNPs' surface. This result proved the success of the modification.

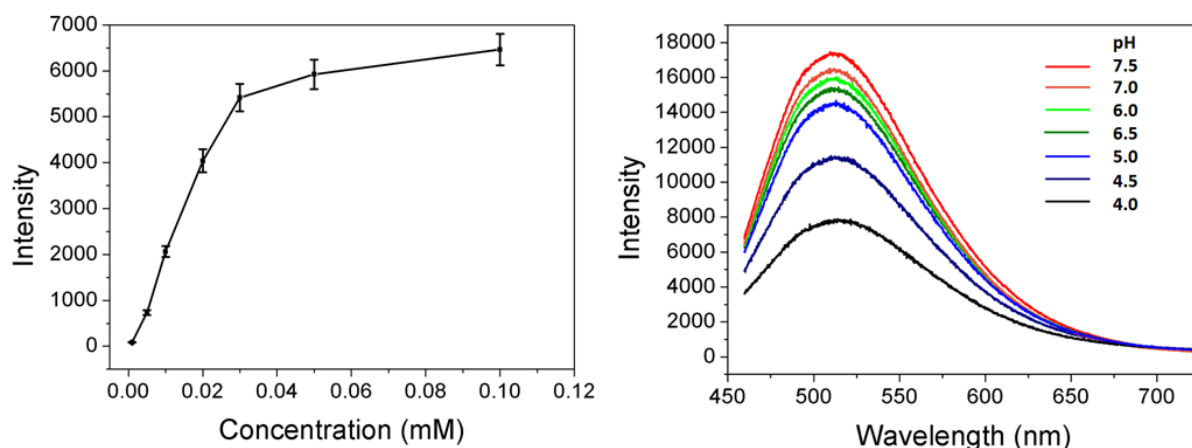


Figure 2.6. (Left) Fluorescence intensity as a function of Hoechst 33342 concentration. At low concentration, the relation between intensity and concentration is almost linear. In the controlled release experiment, the concentration of Hoechst dye released into the solution is lower than 0.01 mM. **(Right)** Fluorescence Spectra of a 0.01 mM Hoechst 33342 water solution under different pH. The pH value was adjusted by NaOH or HCl. The fluorescent intensity slightly drops from pH 7.5 - pH 5.0. In the controlled release experiments, the fluorescence intensity increased upon opening the nanovalve, which proved that the concentration of the Hoechst dye in the solution increased.

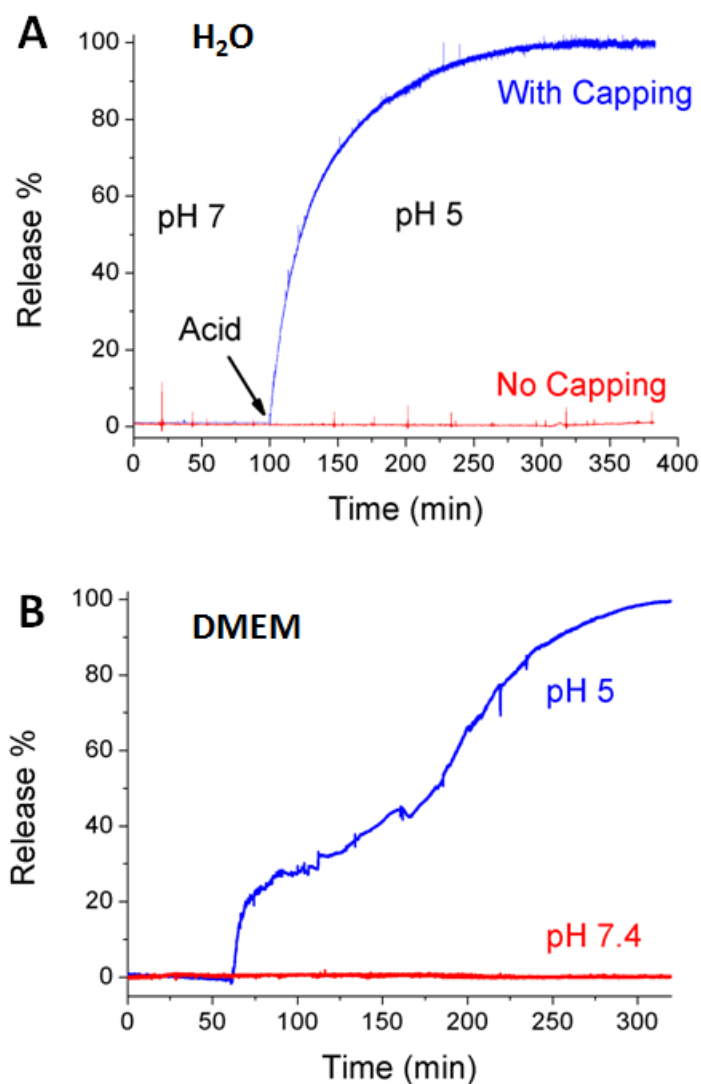


Figure 2.7. (A) Plot of the release of Hoechst 33342 from PSiNPs in aqueous solution. Acid was added to adjust the solution pH. The red line shows the release profile from the control experiment where no cyclodextrin was used for capping. **(B)** The release profile generated in tissue culture medium DMEM. The blue line shows the functioning of the nanovalve when acid was added at 60 min. The red line shows the absence of leakage when the pH is unchanged.

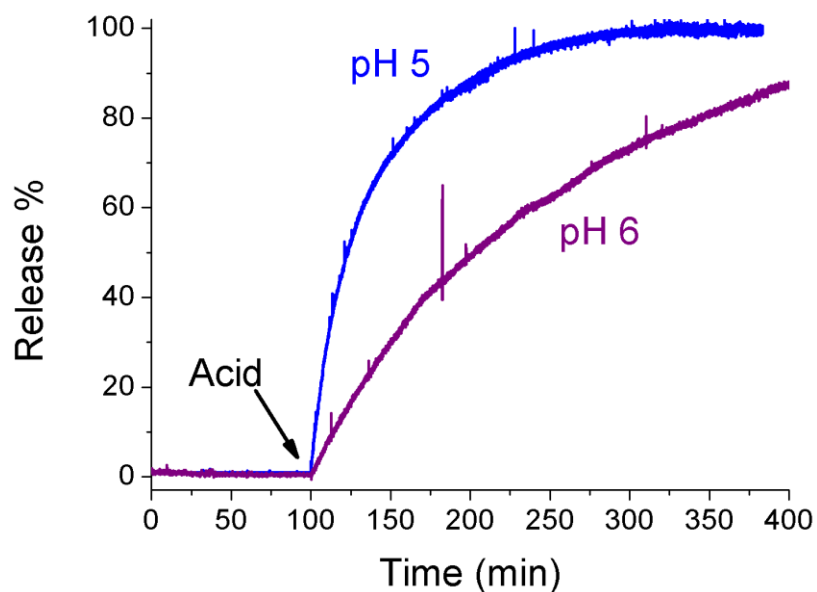


Figure 2.8. Plot of the release of Hoechst 33342 from PSiNPs in aqueous solution at different pH. We have observed that less acidity will lead to prolonged release course. This is, however, believed to be due to the interaction between the positively charged cargo and the negatively charged PSiNPs surface.

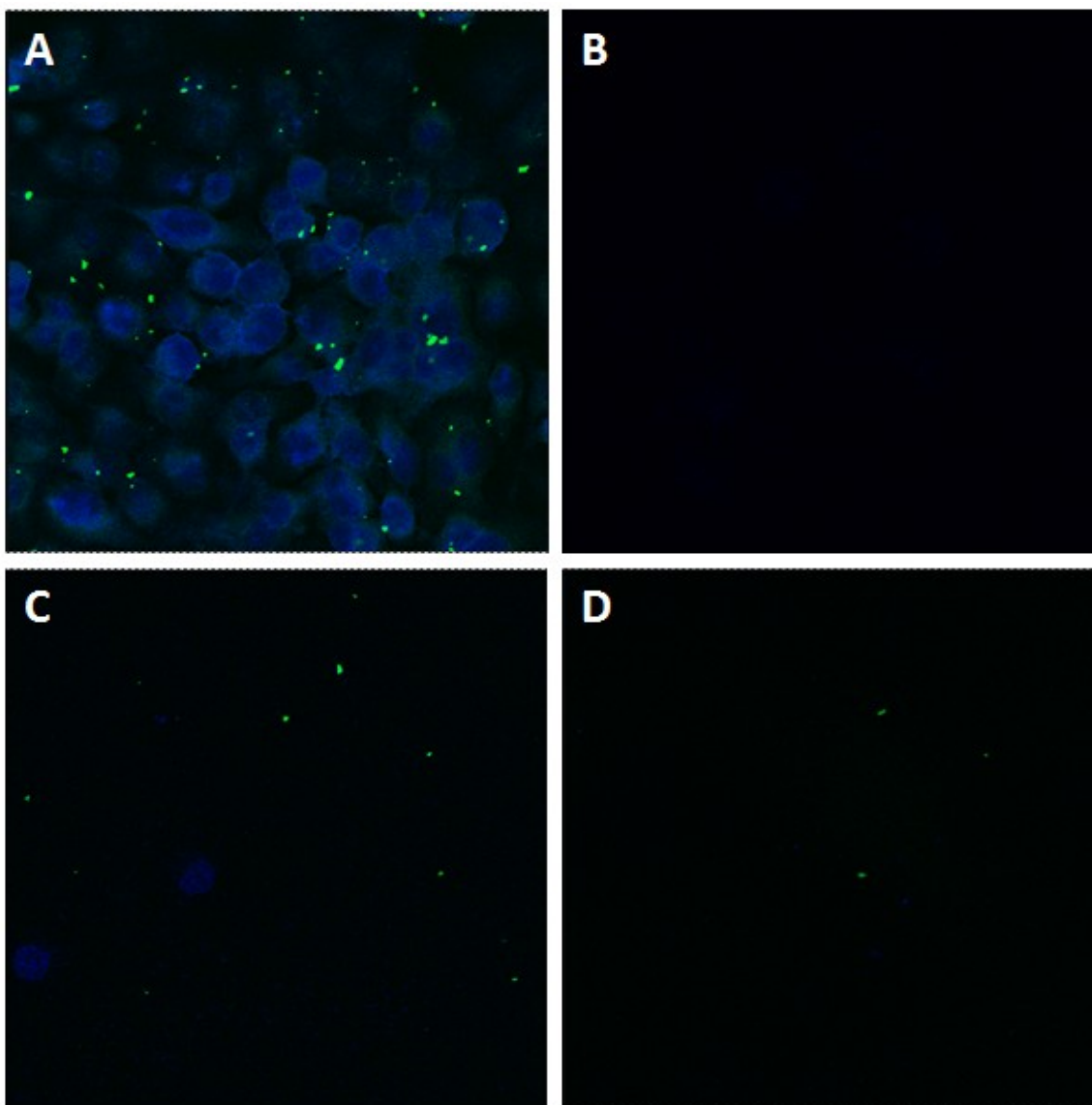


Figure 2.9. Confocal images of PANC-1 cells incubated with PSiNPs. **(A)** Cells treated with 20 $\mu\text{g}/\text{ml}$ of FITC-PSiNPs loaded with Hoechst 33342 at 37 $^{\circ}\text{C}$. **(B)** Same experiment conducted at 4 $^{\circ}\text{C}$. No staining was observed after incubation at low temperature. **(C)** and **(D)** Competition tests: cells were treated with 20 $\mu\text{g}/\text{ml}$ of FITC-PSiNPs loaded with Hoechst 33342 and **(C)** 60 $\mu\text{g}/\text{mL}$ or **(D)** 200 $\mu\text{g}/\text{ml}$ of plain PSiNPs at 37 $^{\circ}\text{C}$.

2.7 References

1. (a) Park, J.-H.; Gu, L.; von Maltzahn, G.; Ruoslahti, E.; Bhatia, S. N.; Sailor, M.J. *Nature Materials* **2009**, *8*, 331-336. (b) Sailor, M. J.; Wu, E. C., *Adv. Funct. Mater.* **2009**, *19*, 3195–3208. (c) Cheng, L.; Anglin, E.; Cunin, F.; Kim, D.; Sailor, M. J.; Falkenstein, I.; Tammewar, A.; Freeman, W. R; *Br. J. Ophthalmol.* **2008**, *92*, 705–711. (d) Anglin, E. J.; Cheng, L.; Freeman, W. R.; Sailor, M. J., *Adv. Drug Deliv. Rev.* **2008**, *60*, 1266–1277. (e) Wu, E. C.; Park, J.-H.; Park, J.; Segal, E.; Cunin, F.; Sailor, M. J., *ACS Nano* **2008**, *2*, 2401-2409.
2. (a) Bimbo, L. M.; Sarparanta, M.; Santos, H. A.; Airaksinen, A. J.; Makila, E.; Laaksonen, T.; Peltonen, L.; Lehto, V.-P.; Hirvonen, J.; Salonen, J.. *ACS Nano* **2010**, *4*, 3023-3032. (b) Salonen, J.; Laitinen, L.; Kaukonen, A.M.; Tuura, J.; Björkqvist, M.; Heikkilä, T.; Vähä-Heikkilä, K.; Hirvonen, J.; Lehto, V.-P. *J. Ctrl. Rel.* **2005**, *108*, 362-374.
3. De Angelis, F.; Pujia, A.; Falcone, C.; Iaccino, E.; Palmieri, C.; Liberale, C.; Mearini, F.; Candeloro, P.; Luberto, L.; de Laurentiis, A.; Das, G.; Scala, G.; Di Fabrizio, E. *Nanoscale* **2010**, *2*, 2230-2236.
4. (a) Ferrati, S.; Mack, A.; Chiappini, C.; Liu, X.; Bean, A. J.; Ferrari, M.; Serda, R. E. *Nanoscale* **2010**, *2*, 1512-1520. (b) Tasciotti, E.; Liu, X.; Bhavane, R.; Plant, K.; Leonard, A. D.; Price, B. K.; Cheng, M. M.; Decuzzi, P.; Tour, J. M.; Robertson, F.; Ferrari, M. *Nature Nano-technology* **2008**, *3*, 151-157. (c) Serda, R. E.; Ferrati, S.; Godin, B.; Tasciotti, E.; Liu, X. W.; Ferrari, M. *Nanoscale* **2009**, *1*, 250-259. (d) Serda, R. E.; Mack, A.; Pulikkathara, M.; Zaske, A. M.; Chiappini, C.; Fakhoury, J. R.; Webb, D.; Godin, B.; Conyers, J. L.; Liu, X. W.; Bankson, J. A.; Ferrari, M. *Small* **2010**, *6*, 1329-1340.
5. Rosso-Vasic, M; Spruijt, E.; Popovic, Z.; Overgaag, K.; van Lagen, B.; Grandidier, B.; Vanmaekelbergh, D.; Dominguez-Gutierrez, D.; De Cola, L.; Zuilhof, H. *J. Mater. Chem.* **2009**, *19*, 5926-5933.

6. Vaccari, L.; Canton, D.; Zaffaroni, N.; Villa, R.; Tormen, M.; di Fabrizio, E. *Microelectronic Engineering* **2006**, *83*, 1598-1601.
7. Hochbaum, A. I.; Gargas, D.; Hwang, Y. J.; Yang, P. D. *Nano Lett.* **2009**, *9*, 3550-3554.
8. (a) Qu, Y. Q.; Zhong, X.; Li, Y. J.; Liao, L.; Huang, Y.; Duan, X. F. *J. Mater. Chem.* **2010**, *20*, 3590–3594. (b) Qu, Y. Q.; Liao, L.; Li, Y. J.; Zhang, H.; Huang, Y.; Duan, X. F. *Nano Lett.* **2009**, *9*, 4539–4543. (c) Zhong, X.; Qu, Y.Q.; Lin, Y.C.; Liao, L.; Duan, X.F.; *ACS Appl. Mater. Inter.* **2011**, *3*, 261-270.
9. (a) Patel, K.; Angelos, S.; Dichtel, W. R.; Coskun, A.; Yang, Y. W.; Zink, J. I.; Stoddart, J. F. *J. Am. Chem. Soc.* **2008**, *130*, 2382-2383. (b) Nguyen, T. D.; Leung, K. C. F.; Liong, M.; Pentecost, C. D.; Stoddart, J. F.; Zink, J. I. *Org. Lett.* **2006**, *8*, 3363-3366. (c) Angelos, S.; Yang, Y. W.; Patel, K.; Stoddart, J. F.; Zink, J. I. *Angew. Chem. Int. Ed.* **2008**, *47*, 2222-2226. (d) Du, L.; Liao, S.; Khatib, H. A.; Stoddart, J. F.; Zink, J. I. *J. Am. Chem. Soc.* **2009**, *131*, 15136-15142. (e) Angelos, S.; Khashab, N. M.; Yang, Y. W.; Trabolsi, A.; Khatib, H. A.; Stoddart, J. F.; Zink, J. I. *J. Am. Chem. Soc.* **2009**, *131*, 12912-12914. (f) Meng, H.; Xue, M.; Xia, T.; Zhao, Y.-L.; Tamanoi, F.; Stoddart, J.F.; Zink, J.I.; Nel, A.E. *J. Am. Chem. Soc.* **2010**, *132*, 12690–12697.
10. Cullis, A.G.; Canham, L.T.; Calcott, P.D.; *J. Appl. Phys.* **1997**, *82*, 909-965.
11. Chiappini, C.; Liu, X.; Fakhoury, J.R.; Ferrari, M. *Adv. Funct. Mater.* **2010**, *20*, 2231-2239.
12. Huang, Z.; Geyer, N.; Werner, P.; de Boor, J.; Gösele, U. *Adv. Mater.* **2011**, *23*, 285-308.
13. The size of Hoechst molecule is about 2.5 nm by 0.75 nm. At the pore opening, the nanovalve occupies part of the space and blocks the pore. The size of nanovalve in this work is about 1.5 nm. Assuming that there are 2 nanovalves per pore opening; about 3 nm of the pore diameter will then be blocked. As a result, only pores with sizes smaller than 5.5 nm will be utilized to trap Hoechst molecules. Any Hoechst stored in larger pores will have enough space to move in and out freely, and they will be removed from the PSiNPs during

the washing process. When a larger molecule (Doxorubicin) was used as cargo, a loading capacity of 3% was determined under the same conditions.

Chapter 3

Size-Selective Megagates on Mesoporous Silica Materials

3.1 Abstract

pH-responsive megagates have been fabricated around mesoporous silica material SBA-15 in order to mechanize the mesopores. These megagates remain closed in neutral conditions, but open at pH 5. The capping components of the megagates were designed to be capable of controlling pores up to 6.5 nm in diameter. Selectivity of payloads with different sizes can be achieved through the use of different capping components. The operation of the megagates was demonstrated by time-resolved fluorescence spectroscopy which is capable of monitoring the release of both the payload and the cap. This study opens up new possibilities in the field of controllable release.

3.2 Introduction

Mesoporous silica materials have been studied widely in the fields of controlled release and drug delivery,¹ on account of their high surface areas, porous structures, and ease of functionalization. One of the most important applications of these materials has been to employ them as scaffolds for the controlled release of cargo molecules.² In order to achieve this end, the access to the pore opening needs to be controlled, preferably by means of a chemical method that can mechanize the pores so as to result in a stimulus-responsive release. A variety of methods have been developed to meet this criterion, such as macromolecule capping,³ nanocrystal capping,⁴ polymer coating,⁵ and nanomachine construction.⁶ These methods have all proven to be successful and many of them have resulted in materials with potential biomedical applications.^{2,3,6b} These methods, however, have mostly been applied only to MCM-41-type materials in which the typical pore size is 2–3 nm. This choice of materials limits considerably the size range of molecules that can serve as payloads, thus restricting the future applications of the delivery systems. Some pioneering works have demonstrated the storage and release of larger cargos,⁷ such as proteins, polymers, and RNAs, from large pored mesoporous silica materials, where the simple electrostatic interaction between the cargos and the silica served as the dominant storage-release mechanism. It remains challenging to design a method to achieve on-demand release in a more precisely controlled manner.

In this chapter, I describe the design and synthesis of a cargo size-selective pH-responsive megagate system that is able to mechanize mesopores with diameters of up to 6.5 nm. The megagates are designed to be fluorescent so that their operation may be monitored facilely. A well-established standard polymer (dextran) has been chosen as a model cargo for proof of principle. By using another cargo molecule with a smaller size—fluorescein disodium salt—I demonstrate that size-selective controlled release can be achieved upon tuning the capping components of the megagates.

3.3 Experimental

General Methods

All reactions were performed under an argon atmosphere and in dry solvents, unless otherwise stated. tetraethylorthosilicate (99%) and 1-butylaldehydetriethoxysilane (90%) were purchased from Gelest Inc. (PA). Propargyl bromide (80% in toluene), 2-[2-(2-chloroethoxy)-ethoxy]-ethanol (96%), 1-adamantanecarbonyl chloride (95%), copper(II) sulfate pentahydrate (98%), sodium L-ascorbate (98%), Pluronic P123, fluorescein disodium salt (98.5%), and fluorescein isothiocyanate-dextran (MW 3K), and all solvents were purchased from Sigma-Aldrich (St. Louis, MO). 6-(2-aminoethyl)amino-6-deoxy- β -cyclodextrin,⁸ **1**,⁹ and **3**¹⁰ were synthesized according to literature procedures. Analytical thin-layer chromatography (TLC) was performed on aluminum sheets, precoated with silica gel 60-F254 (Merck 5554). Column chromatography was carried out using silica gel 60F (230-400 mesh). ¹H and ¹³C NMR spectra were recorded on Bruker ARX 500 MHz and DSX 500 MHz spectrometers, respectively, at ambient temperature, unless otherwise noted. Solid-state ¹³C CP/MAS Spectra was recorded on a Bruker DSX 300 MHz spectrometer. High-resolution MS data were recorded on an Applied Biosystems-MDS Sciex 4000 Q Trap with ESI sources. The chemical shifts are listed in ppm on the δ scale and coupling constants were recorded in Hertz (Hz). Chemical shifts are reported in ppm relative to the signals corresponding to the residue non-deuterated solvents (CDCl₃: δ 7.26 ppm, CD₃SOCD₃: δ 2.47 ppm). The following abbreviations are used to explain the multiplicities: s, singlet; d, doublet; t, triplet; b, broad peaks; m, multiplet or overlapping peaks.

Synthesis of Compound 2

SiCl₄ (5.25 mL, 45.7 mmol) was added over 5 min to a solution of **1**⁹ (2.0 g, 11.5 mmol) in EtOH (10 mL). After the reaction mixture had been stirred for a further 15 min, the precipitates were collected by vacuum filtration and washed with MeOH to yield **2** as a pink solid (1.1 g, 61%). ¹H NMR (500 MHz, CDCl₃): δ = 7.66 (s, 3H), 7.63 (d, *J* = 8.7 Hz, 6H), 7.09 (d, *J* = 8.7 Hz,

6H), 4.76 (d, $J = 2.4$ Hz, 6H), 2.56 (t, $J = 2.2$ Hz, 3H). ^{13}C NMR (125 MHz, CDCl_3): $\delta = 157.2$, 141.7, 134.7, 128.4, 124.1, 115.2, 78.5, 75.7, 55.9.

Synthesis of Compound 4

Anhydrous K_2CO_3 (0.77 g, 5.6 mmol) was added to a solution of **3**¹⁰ (0.23 g, 0.7 mmol) in anhydrous DMF (30 mL). The solution was purged with Argon for 30 min. Propargyl bromide (80% in PhMe, 700 μL , 7.9 mmol) was added to this solution. The mixture was heated at 80 °C under Argon protection for 18 h. After cooling to room temperature, the mixture was poured into ice water (150 mL). The precipitate was collected by filtration, washed with EtOAc (60 mL) and $\text{Me}_2\text{CO}/\text{H}_2\text{O}$ (70 mL, 3:4 w/v), and dried under vacuum to afford **4** as an off-white powder (0.3 g, 77%). ^1H NMR (500 MHz, CD_3SOCD_3): $\delta = 8.12$ (s, 6H), 5.08 (s, 12H), 3.60 (s, 6H).

Synthesis of Compound 5

Sodium azide (3 g, 46.1 mmol) was added to a solution of 2-[2-(2-chloroethoxy)-ethoxy]ethanol (5.0 g, 29.7 mmol) in anhydrous DMF (50 mL). The mixture was heated at 80 °C for 18 h under Argon. After cooling to room temperature, the mixture was concentrated by rotary evaporation, and the residue was dissolved in anhydrous CH_2Cl_2 and passed through Celite. The resultant solution was concentrated under vacuum and chromatographed (SiO_2 , EtOAc) to yield **5** as a colorless oil (4.5 g, 85%). ^1H NMR (500 MHz, CDCl_3): $\delta = 3.36$ (t, $J = 4.9$ Hz, 2H), 3.58 (t, $J = 3.4$ Hz, 2H), 3.63–3.65 (m, 6H), 3.70 (t, $J = 3.7$ Hz, 2H).

Synthesis of Compound 6

Anhydrous K_2CO_3 (1 g, 7.2 mmol) was added to a solution of **5** (1.3 g, 7.4 mmol) in anhydrous CH_2Cl_2 (5 mL). A solution of 1-adamantanecarbonyl chloride (2.0 g, 10.0 mmol) in anhydrous CH_2Cl_2 (10 mL) was added to the reaction dropwise. The solution was stirred at room temperature for 24 h. The insoluble solid was separated from the solution by filtration. The filtrate was concentrated by rotary evaporation. The residue was then dissolved in EtOAc and

washed with 5% NaHCO₃ aqueous solution and brine. The organic layer was dried (Na₂SO₄), filtered, and concentrated by rotary evaporation. The crude was purified by column chromatography (SiO₂, Hexanes/EtOAc 3:1) to yield **6** as a colorless oil (0.35 g, 20%). ¹H NMR (500 MHz, CDCl₃): δ = 1.71(m, 6H), 1.90 (d, *J* = 4.9 Hz, 6H), 2.01 (s, 3H), 3.39 (t, *J* = 6.2 Hz, 2H), 3.66–3.71 (m, 8H), 4.21 (t, *J* = 6.2 Hz, 2H).

Synthesis of Compound MG-1

CuSO₄•5H₂O (20 mg, 80 μmol) and sodium ascorbate (50 mg, 0.3 mmol) were added to a solution of **6** (0.4 g, 1.2 mmol) and **2** (0.15 g, 0.3 mmol) in DMF (5 mL). The mixture was stirred for 4 d at room temperature then concentrated by rotary evaporation, redissolved in EtOAc, and washed with brine. The organic layer was dried (MgSO₄), filtered, and concentrated by rotary evaporation. The crude was purified by column chromatography (Al₂O₃, Hexanes/EtOAc 1:2, then EtOAc, then EtOAc/MeOH 50:1) to yield **MG-1** as a pale yellow solid (0.36 g, 80%). ¹H NMR (500 MHz, CDCl₃): δ = 1.65 (m, 18H), 1.83 (d, *J* = 3.5 Hz, 18H), 1.95 (s, 9H), 3.57–3.62 (m, 18H), 3.86 (t, *J* = 4.6 Hz, 6H), 4.16 (t, *J* = 4.8 Hz, 6H), 4.53 (t, *J* = 4.6 Hz, 6H), 5.24 (s, 6H), 7.08 (d, *J* = 8.6 Hz, 6H), 7.58 (d, *J* = 8.6 Hz, 6H), 7.62 (s, 3H), 7.84 (s, 3H). ¹³C NMR (125 MHz, CDCl₃): δ = 177.3, 170.9, 157.9, 143.7, 141.6, 134.0, 128.2, 123.9, 123.7, 115.0, 70.4, 70.3, 69.3, 69.1, 50.2, 40.5, 38.6, 36.3, 27.8. ESI-MS: C₈₄H₁₀₅O₁₅N₉ Calculated: [M]⁺ 1480.7919, Found: 1480.5782.

Synthesis of Compound MG-2

CuSO₄•5H₂O (20 mg, 80 μmol) and sodium ascorbate (50 mg, 0.3 mmol) were added to a solution of **6** (0.35 g, 1.0 mmol) and **4** (0.1 g, 0.2 mmol) in DMF (5 mL). The mixture was stirred for 4 d at room temperature. The mixture was concentrated by rotary evaporation, redissolved in EtOAc, and washed with brine. The organic layer was dried over anhydrous MgSO₄, filtered, and concentrated by rotary evaporation. The crude was purified by column chromatography (Al₂O₃, Hexanes/EtOAc 1:2, then EtOAc, then EtOAc/MeOH 50:1) to yield **MG-**

2 as a pale yellow solid (0.13 g, 30%). ¹H NMR (500 MHz, CDCl₃): δ = 1.62–1.70 (m, 36H), 1.70 (d, *J* = 3.3 Hz, 36H), 1.96 (s, 18H), 3.50–3.58 (m, 36H), 3.88 (t, *J* = 6.5 Hz, 12H), 4.13 (t, *J* = 4.9 Hz, 12H), 4.55 (t, *J* = 6.5 Hz, 12H), 5.53 (s, 12H), 8.09 (s, 6H), 8.14 (s, 6H). ¹³C NMR (125 MHz, CDCl₃): δ = 177.4, 148.0, 143.8, 124.5, 123.8, 108.2, 70.5, 70.3, 69.4, 69.1, 50.2, 40.5, 38.7, 36.3, 27.8. ESI-MS: C₁₃₈H₁₈₆O₃₀N₁₈ Calculated: [*M*]⁺ 2577.0696, Found: [*M+H*]⁺ 2578.0671.

Synthesis of SBA-15

Pluronic P123 (2.0 g) was dissolved in a mixture of H₂O (15 mL) and 2 M HCl (60 mL). The mixture was heated to 40 °C until the solution became clear. Tetraethylorthosilicate (4.25 g, 21.6 mmol) was then added to the solution dropwise. The mixture was stirred at 40 °C for 24 h after which it was transferred to a Teflon container and heated under pressure at 80 °C for 24 h. The precipitant, SBA-15,¹¹ was collected by filtration and dried in air.

Synthesis of SBA-15-Aldehyde

As-synthesized SBA-15 (200 mg) was dried under vacuum and suspended in anhydrous PhMe (10 mL). 1-Butylaldehyde-triethoxysilane (30 μL, 0.1 mmol) was added to the reaction mixture. The suspension was heated under reflux over argon for 15 h. After cooling to room temperature, the precipitates were collected by filtration, washed with MeOH, and dried under vacuum. The P123 surfactant was extracted by EtOH in a Soxhlet extractor.

Synthesis of SBA-15-Cyclodextrin

SBA-15-Aldehyde (100 mg) was suspended in anhydrous DMF (10 mL). 6-(2-Aminoethyl)amino-6-deoxy-β-cyclodextrin⁸ (100 mg, 0.08 mmol) and anhydrous MgSO₄ (100 mg, 0.8 mmol) were added into the solution. The mixture was heated at 60 °C for 24 h under Argon. After cooling to room temperature, the resultant precipitates were collected by filtration and washed with H₂O. The product was dried under vacuum.

Loading and Capping for SBA-15-Cyclodextrin

SBA-15-Cyclodextrin (30 mg) was suspended in an aqueous solution of fluorescein disodium salt (FDS) (2 mL, 2 mg/mL) or FITC-Dextran (2 mL, 2 mg/mL). The mixture was stirred at room temperature for 24 h. A solution of the capping agent, **MG-1** or **MG-2**, (20 mg) in Me₂SO (2 mL) was then added into the mixture which was stirred for 30 min and the precipitate was collected by centrifugation, washed extensively with Me₂SO/H₂O (1:1) and dried under vacuum.

Assessment of Cargo Release and Cap Dissociation

The release profiles were obtained by a time-resolved fluorescence spectroscopy method. The solid sample was placed at the corner of a quartz cuvette. The cuvette was then filled with PBS buffer (pH 7.4) and the solution was gently stirred to accelerate the dispersion of the released dye. A probe beam (448 nm, 20 mW for FDS and FITC-Dextran; 257 nm, 20 mW for **MG-1**; 351 nm, 30 mW for **MG-2**) was directed into the solution to excite the dissolved cargo molecules or dissociated cap molecules. The luminescence spectrum was collected in 1 sec intervals over the course of the experiment. The pH of the solution was adjusted to the desired value with 1 M HCl. The luminescence intensity at the emission maximum of the cargo or cap was plotted as a function of time to generate a release profile.

3.4 Results and Discussion

In this investigation, the well-known mesoporous silica material, SBA-15,¹¹ has been employed as the model platform. The synthesis of SBA-15 was based on established procedures. A pluronic P123 triblock copolymer was used as the templating agent, resulting in 2D hexagonal-patterned pores. N₂ adsorption-desorption analysis gave a BET surface area of 650 m²/g, and the average pore size was calculated to be around 6.5 nm (Figure 3.4).

In our previous studies where MCM-41-type materials were employed, a variety of nanovalve systems were designed^{6,12} to mechanize the pores. The typical design of these nanovalves consisted of two components, a linear one (the stalk) that is grafted at the opening of the mesopores, and a bulky compound (the cap) that can associate with the stalk as a result of noncovalent bonding interactions and block the pores.^{6,12} Upon appropriate stimulation, the interactions between the stalk and the cap can be weakened, allowing the cap to depart from the binding site, thus opening up the pore. In order to control access to the bigger pores found in SBA-15, a much larger capping agent, namely a megagate molecule (MGM), becomes necessary.

It is not necessary, however, to cover the pores completely in order to prevent leakage when attempting to store large molecules. It is envisioned that the use of a weblike cap large enough to extend across the pores would be sufficient to serve as a megagate. With this thought in mind, I designed **MG-1**, consisting of a 1,3,5-triphenylbenzene core linked to three adamantine moieties by triethylene glycol chains using Cu-catalyzed azide-alkyne cycloaddition (CuAAC).¹³ The core was synthesized (Figure 3.1a) by first of all propargylating 4'-hydroxyacetophenone to obtain the precursor **1**. A subsequent SiCl₄-induced cyclotrimerization yielded **2**, a versatile trialkyne building block. The arms of the cap were obtained (Figure 3.1c) by converting 2-[2-(2-chloroethoxy)-ethoxy]-ethanol to the azide **5** and then reacting **5** with 1-adamantanecarbonyl chloride under basic conditions to yield **6**. A simple CuAAC between **2** and **6** provided (Figure 3.1d) the desired compound, **MG-1**.

MG-1 has a theoretical diameter of about 5.5 nm—calculated by a molecular mechanics method in SPARTAN 5.1—when fully extended. While this diameter is less than that of the average pore size (ca. 6.5 nm) in the nanoparticles, **MG-1** is still a good candidate because (i) in the case of sufficiently large cargo molecules, blocking even just a small section of the pore orifice—much like a mathematical chord of a circle—will prevent leakage from the nanoparticle, (ii) this dimension does not include the size of the surface-attached cyclodextrin moiety, which is

around 1.5 nm, and (iii) more importantly, more than one cap molecule may be associated with each pore.

The bare SBA-15 nanoparticles were functionalized with 1-butylaldehydetriethoxysilane to provide an anchoring point for the stalks. The amine-modified cyclodextrin stalk **7** was grafted (Figure 3.2b) onto SBA-15 by imine bond formation. It is well-known¹⁴ that imine bonds are acid-sensitive, and will cleave upon lowering the pH, providing the mechanism for operation of the megagate.[‡] The successful surface modification of the SBA-15 was confirmed by solid-state NMR spectroscopy (Figure 3.3).

The overall operation of the megagate is illustrated in Figure 3.2c. The modified SBA-15 is loaded with cargo, and then capped by a MGM. In aqueous solutions, the adamantane moieties bind strongly to the cyclodextrin tori as a result of hydrophobic interactions. Upon binding, the MGMs serve to prevent the loaded cargo from leaking out of the pores. When the pH of the solution is lowered, the imine bonds in the stalks are cleaved, allowing the cyclodextrin tori to dissociate from the surface. As a result, the MGMs, which are still bound to the cyclodextrin tori, are no longer blocking the pores, thus leading to the release of cargo from the nanoparticles.

In order to demonstrate the functioning of the megagates, a well-established¹² time-resolved fluorescence spectroscopic method was employed. The SBA-15 was first of all loaded with the fluorescent cargo, that is, either FITC-Dextran (M.W. 3K, hydrodynamic size about 4 nm¹⁵) or fluorescein disodium salt (FDS). MGMs were then used to cap the pores. After drying under vacuum, the capped SBA-15 was placed in a PBS buffer solution. The pH of the solution was then adjusted to 5 to initiate the release of the cargo. The released cargo in the supernatant was excited by a probe laser beam and the corresponding fluorescence spectrum was recorded by a CCD spectrometer to generate the release profile.

When **MG-1** was employed as the capping agent (Figure 3.5a), FITC-Dextran was trapped successfully in the pores of SBA-15. There was no significant premature release,

indicating that as predicted, **MG-1** is large enough to block the pore orifices and prevent the FITC-Dextran molecules from escaping. A release capacity of about 3.3% wt. was determined by UV-Vis spectroscopy after the completion of the release. This relatively low value arises from the fact that the capping process occurs on a statistical basis. Only those pores blocked by extended MGs will contribute to the effective release capacity. Cargos loaded in incompletely capped pores will be washed out during the subsequent washing process. This release capacity is enough, however, for certain biomedical applications.¹⁶ The prolonged time course of the release is a consequence of the low diffusion rate of the bulky FITC-Dextran cargo. In a control experiment where there was no **MG-1** capping agent present, a significantly smaller amount of cargo release was observed as molecules could not be trapped within the pores during the loading process. The near-negligible release detected may be attributed to residual surface-adsorbed molecules. This proves that megagates equipped with **MG-1** caps operate as designed. By using a different probe beam, the dissociation process of the megagates from the silica surface to the solution can be monitored (Figure 3.5b). The fast completion of this process correlates well with the proposed release mechanism.

When a smaller cargo (FDS) was used in analogous experiments, however, **MG-1** failed (Figure 3.5c) to function as a cap, presumably because the gaps between the adamantane moieties were too big to prevent FDS from leaking out. In order to trap smaller molecules, a “tighter” cap is needed. Therefore, a cap with twice as many adamantane arms as **MG-1** was designed. The synthesis (Figure 3.1b) of **MG-2** was facile. Hexahydroxytriphenylene (**3**) was propargylated to yield the hexaalkyne **4**, which was then reacted with **6** under CuAAC conditions to yield (Figure 3.1d) **MG-2**. With its hexameric structure, **MG-2** exhibits much less space between adamantane moieties while maintaining a similar area of coverage as **MG-1** (Figure 3.2a). Indeed, **MG-2** was able (Figure 3.6a) to trap FDS molecules successfully. The release profile, which was again tracked by time-resolved fluorescence spectroscopy, was faster than that of FITC-Dextran, an observation which can be explained by the higher mobility of the

smaller cargo. The dissociation profile of **MG-2** also correlates well with the release course (Figure 3.6b) of the FDS. In order to compare the efficiency of MG-2 with that of MG-1, FITC-Dextran was employed as cargo in the MG-2 system, and a release capacity of 3.3 % wt. was determined. This result is close to that from the MG-1 system, suggesting that in spite of the size-selective effect, the cap does not influence the loading or release of the cargo.

3.5 Summary

In this chapter, a “megagate” methodology has been developed to mechanize the mesopores of SBA-15. Depending on the number of arms on the cap, the megagate is capable of storing, and then releasing, differently sized cargoes from SBA-15 upon pH stimulation. Further investigations towards biomedical applications are currently ongoing.

3.6 Figures

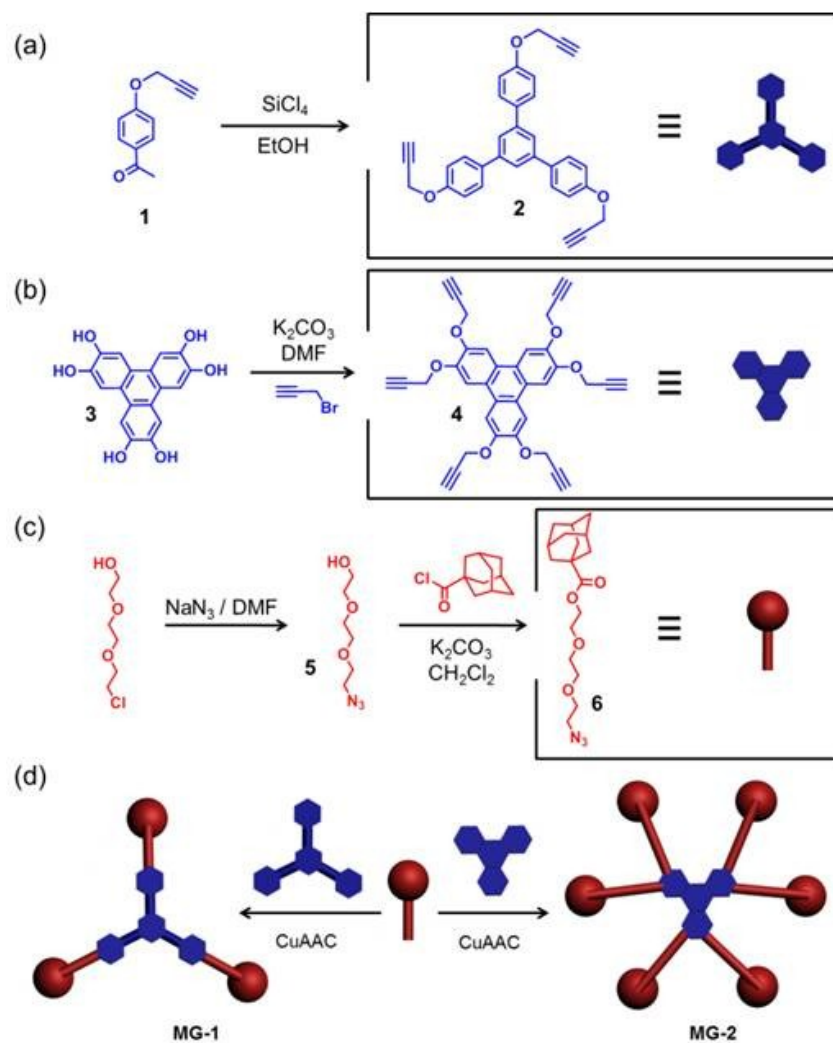


Figure 3.1. The synthesis of (a) **2**, (b) **4**, and (c) **6**. The construction of (d) **MG-1** and **MG-2** by Cu-catalyzed click reactions

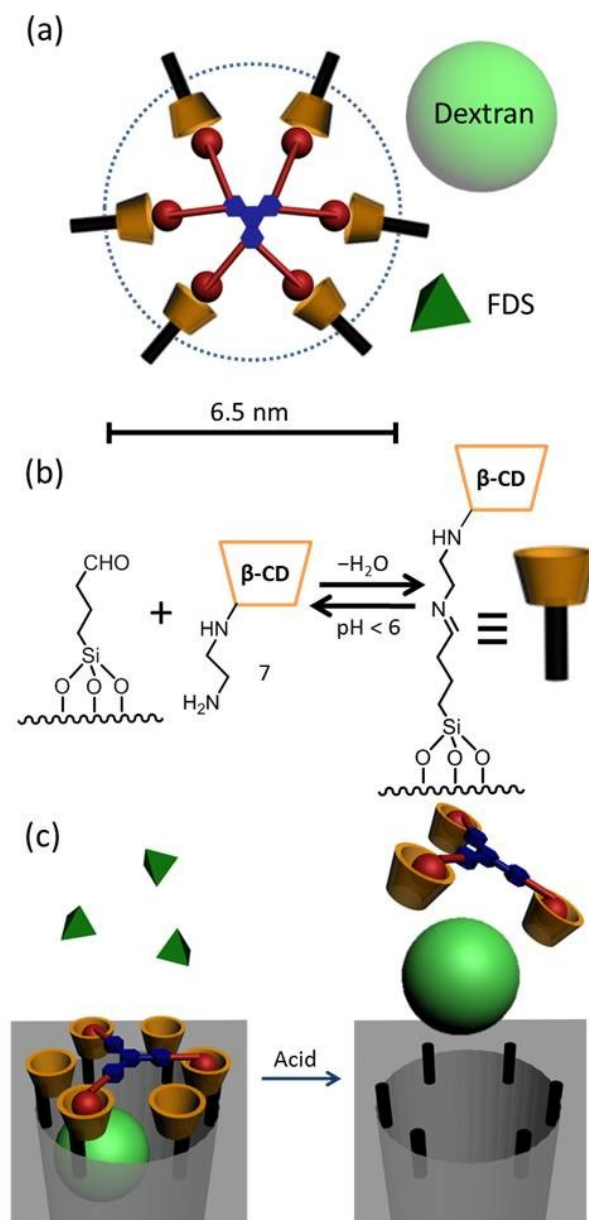


Figure 3.2. (a) The fully extended structure of a megagate incorporating **MG-2** as the capping molecule. The dashed circle, the light green ball and the dark green pyramid show the relative sizes of the pore, the dextran cargo, and the fluorescein disodium salt (FDS), respectively. (b) The attachment of cyclodextrin onto the aldehyde-modified silica through imine formation. (c) The operation of a megagate capped by **MG-1**. The size of **MG-1** allows FDS to escape freely from the pore, while Dextran is trapped within the pore until the gate is opened by the addition of acid.

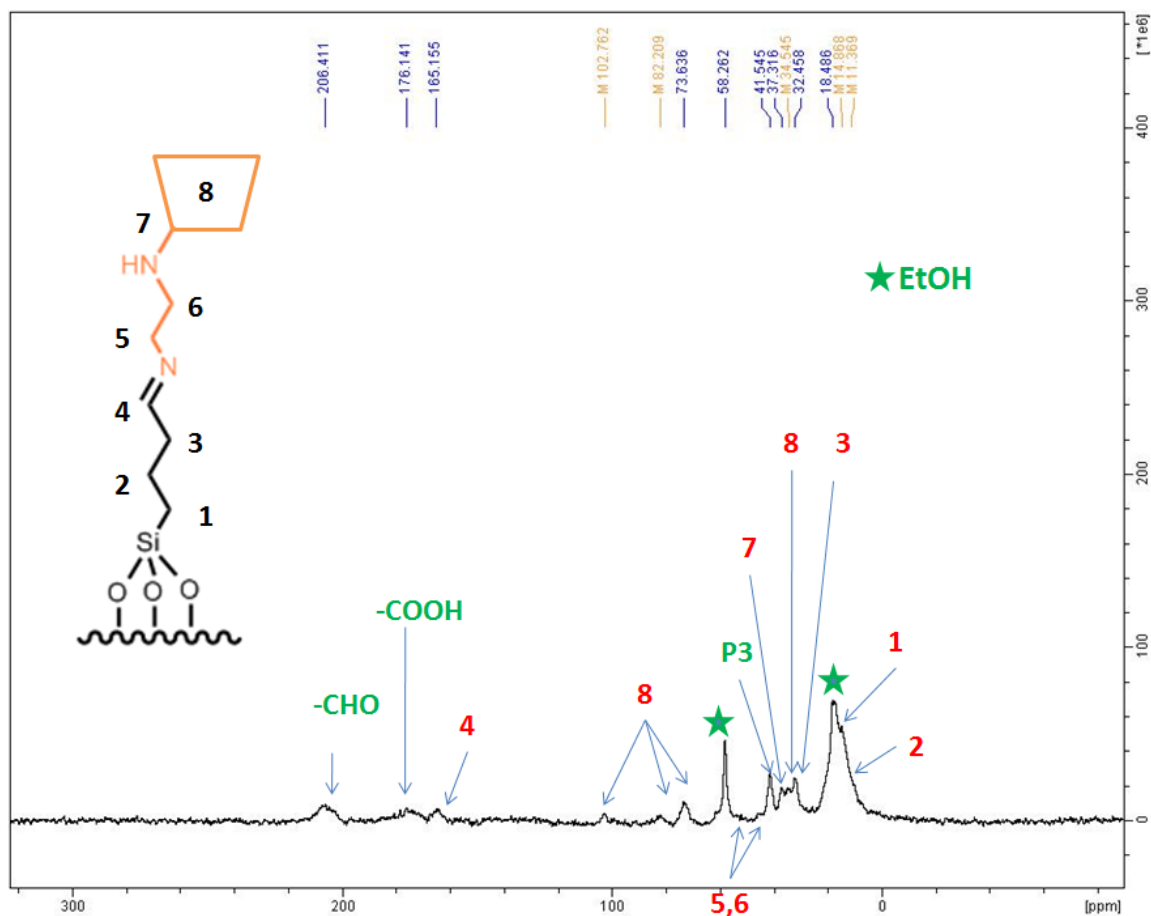


Figure 3.3. The ^{13}C CP/MAS NMR spectrum of the cyclodextrin-modified SBA-15. All resonances are assigned in the Figure. The green stars denote EtOH resonances. The ^{13}C CP/MAS NMR spectrum of the cyclodextrin-modified SBA-15 confirms that imine formation between 6-(2-aminoethyl)amino-6-deoxy- β -cyclodextrin and SBA-15 took place successfully. The resonances at ~ 210 ppm can be assigned to unreacted aldehyde residues. The resonances at ~ 180 ppm can be assigned to carboxylic acids that are a product of the oxidation of the unreacted aldehydes. The proton α to the unreacted aldehyde, P3, resonates at ~ 40 ppm.

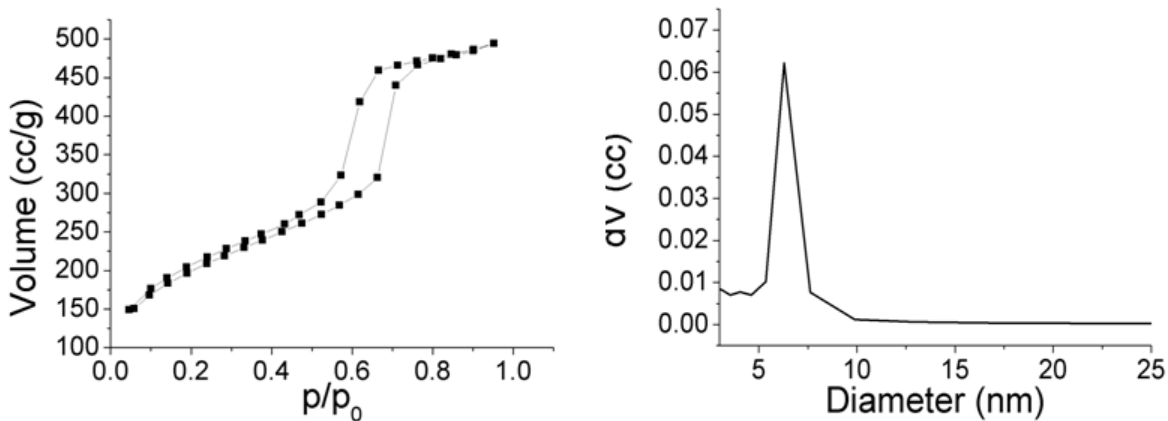


Figure 3.4. The N₂ adsorption and desorption isotherms (**left**) and the pore size distribution (**right**) for SBA-15 as-synthesized. The distribution of pore sizes was determined from N₂ adsorption-desorption experiments. The relatively uniform pore sizes ensure that the majority of the pores are functional and able to uptake the large dextran cargo molecules.

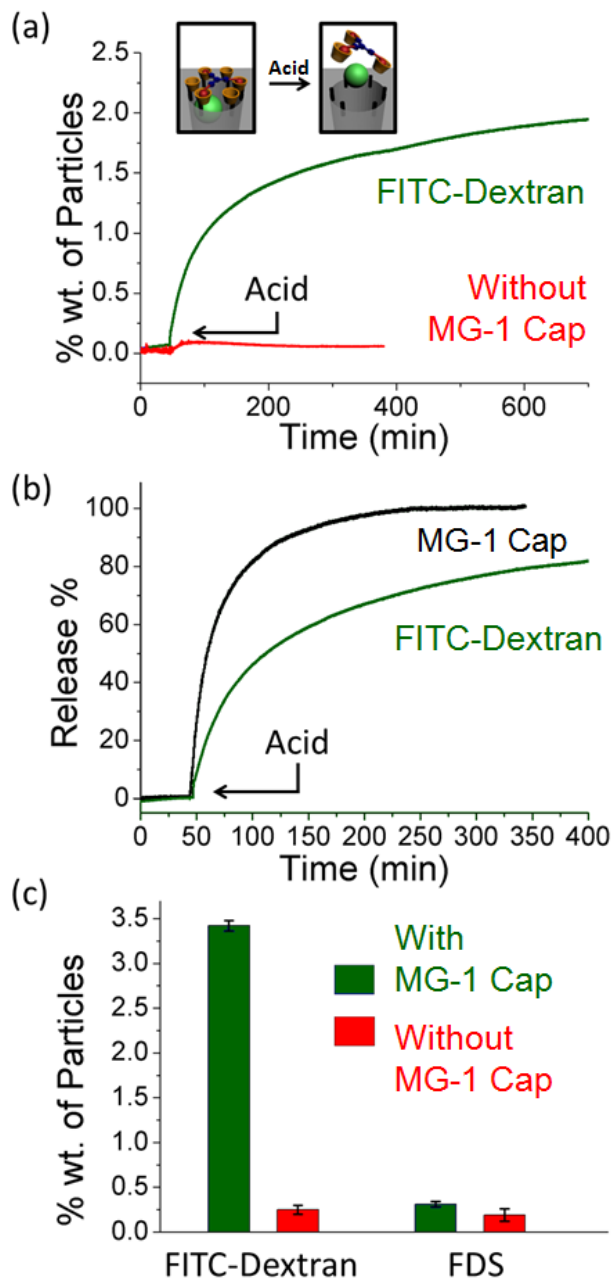


Figure 3.5. (a) The release profile of FITC-Dextran from SBA-15 capped with **MG-1** (green line). The control experiment with no cap resulted in negligible release (red line). (b) The release profile of the MG-1 cap (black line). The release of the cargo (green line) was used as a reference. (c) Release capacities of nanoparticles loaded with different cargoes, with and without the MG-1 cap.

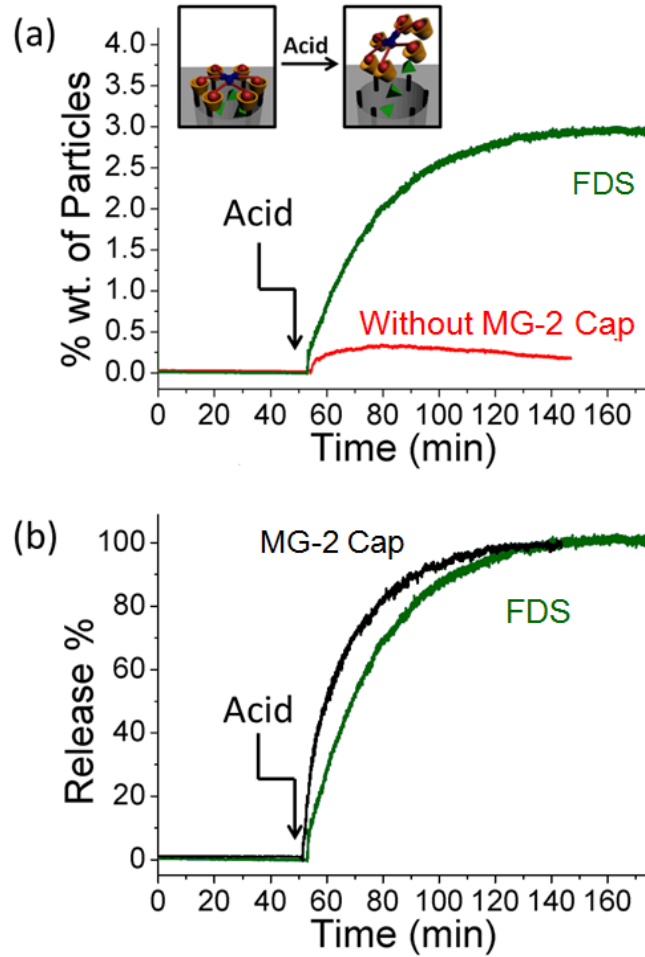


Figure 3.6. (a) The release profile of FDS from SBA-15 capped with **MG-2** (green line). The control experiment with no cap resulted in negligible release (red line). **(b)** The release profile of the **MG-2** cap (black line). The release of FDS was used as reference (green line).

3.7 References

- 1 (a) M. Vallet-Regi, A. Rámila, R. P. del Real and J. Pérez-Pariente, *Chem. Mater.* 2001, **13**, 308–311; (b) I. I. Slowing, B. G. Trewyn, S. Giri and V. S.-Y. Lin, *Adv. Func. Mater.* 2007, **17**, 1225–1236; (c) J. Kim, H. S. Kim, N. Lee, T. Kim, H. Kim, T. Yu, I. C. Song, W. K. Moon and T. Hyeon, *Angew. Chem. Int. Ed.* 2008, **47**, 8438–8441; (d) M. Liong, S. Angelos, E. Choi, J. F. Stoddart and J. I. Zink, *J. Mater. Chem.* 2009, **19**, 6251–6257; (e) C. E. Ashley, E. C. Carnes, G. K. Phillips, D. Padilla, P. N. Durfee, P. A. Brown, T. N. Hanna, J. Liu, B. Phillips, M. B. Carter, N. J. Carroll, X. Jiang, D. R. Dunphy, C. L. Willman, D. N. Petsev, D. G. Evans, A. N. Parikh, B. Chackerian, W. Wharton, D. S. Peabody and C. J. Brinker, *Nat. Mater.* 2011, **10**, 389–397.
- 2 (a) B. G. Trewyn, I. I. Slowing, S. Giri, H.-T. Chen and V. S.-Y. Lin, *Acc. Chem. Res.* 2007, **40**, 846–853; (b) Z. Li, J. C. Barnes, A. Bosoy, J. F. Stoddart and J. I. Zink, *Chem. Soc. Rev.* 2012, **41**, 2590–2605; (c) K. K. Qian, R. H. Bogner, *J. Pharm. Sci.* 2012, **101**, 444–463; (d) J. M. Rosenholm, V. Mamaeva, C. Sahlgren and M. Linden, *Nanomedicine*, 2012, **7**, 111–120.
- 3 (a) D. R. Radu, C.-Y. Lai, K. Jeftinija, E. W. Rowe, S. Jeftinija and V. S.-Y. Lin, *J. Am. Chem. Soc.* 2004, **126**, 13216–13217; (b) A. Schlossbauer, S. Warncke, P. M. E. Gramlich, J. Kecht, A. Manetto, T. Carell and T. Bein, *Angew. Chem. Int. Ed.* 2010, **49**, 4734–4737.
- 4 C.-Y. Lai, B. G. Trewyn, D. M. Jeftinija, K. Jeftinija, S. Xu, S. Jeftinija and V. S.-Y. Lin, *J. Am. Chem. Soc.* 2003, **125**, 4451–4459.
- 5 (a) J. M. Xue and M. Shi, *J. Ctrl. Rel.* 2004, **98**, 209–217; (b) Y. Zhu, J. Shi, W. Shen, X. Dong, J. Feng, M. Ruan and Y. Li, *Angew. Chem. Int. Ed.* 2005, **44**, 5083–5087; (c) H. Meng, M. Liong, T. Xia, Z. Li, Z. Ji, J. I. Zink and A. E. Nel, *ACS Nano* 2010, **4**, 4539–4550; (d) C. Argyo, V. Cauda, H. Engelke, J. Rädler, G. Bein and T. Bein, *Chem. Eur. J.* 2012, **18**, 428–432.

- 6 (a) K. Coti, M. E. Belowich, M. Liong, M. W. Ambrogio, Y. A. Lau, H. A. Khatib, J. I. Zink, N. M. Khashab and J. F. Stoddart, *Nanoscale* 2009, **1**, 16–39; (b) H. Meng, M. Xue, T. Xia, Y.-L. Zhao, F. Tamanoi, J. F. Stoddart, J. I. Zink and A. E. Nel, *J. Am. Chem. Soc.* 2010, **132**, 12690–12697; (c) M. W. Ambrogio, C. R. Thomas, Y.-L. Zhao, J. I. Zink and J. F. Stoddart, *Acc. Chem. Res.* 2011, **44**, 903–913; (d) C. Wang, Z. Li, D. Cao, Y.-L. Zhao, J. W. Gaines, O. A. Bozdemir, M. W. Ambrogio, M. Frasconi, Y. Y. Botros, J. I. Zink and J. F. Stoddart, *Angew. Chem. Int. Ed.* 2012, **51**, 5460–5465.
- 7 (a) Q. Yang, S. Wang, P. Fan, L. Wang, Y. Di, K. Lin and F.-S. Xiao, *Chem. Mater.* 2005, **17**, 5999–6003; (b) I. I. Slowing, B. G. Trewyn and V. S.-Y. Lin, *J. Am. Chem. Soc.* 2007, **129**, 8845–8849; (c) F. Gao, P. Botella, A. Corma, J. Blesa and L. Dong, *J. Phys. Chem. B.* 2009, **113**, 1796–1804; (d) T.-W. Kim, I. I. Slowing, P.-W. Chung and V. S.-Y. Lin, *ACS Nano*, 2011, **5**, 360–366; (e) M.-H. Kim, H.-K. Na, Y.-K. Kim, S.-R. Ryoo, H. S. Cho, K. E. Lee, H. Jeon, R. Ryoo and D.-H. Min, *ACS Nano*, 2011, **5**, 3568–3576.
- 8 B. L. May, S. D. Kean, C. J. Easton and S. F. Lincoln, *J. Chem. Soc., Perkin Trans.* 1997, **1**, 3157–3160.
- 9 R. H. Hans, E. M. Guantai, K. Chibale, C. Lategan, P. J. Smith, B. Wan, S. G. Franzblau, J. Gut and P. J. Rosenthal, *Bioorg. Med. Chem. Lett.* 2010, **11**, 942–944.
- 10 F. C. Krebs, N. C. Schioedt, W. Batsberg and K. Bechgaard, *Synthesis*. 1997, **11**, 1285–1290.
- 11 D. Zhao, J. Feng, Q. Huo, N. Melosh, G. H. Fredrickson, B. F. Chmelka and G. D. Stucky, *Science* 1998, **279**, 548–552.
- 12 (a) T. D. Nguyen, H.-R. Tseng, P. C. Celestre, A. H. Flood, Y. Liu, J. F. Stoddart and J. I. Zink, *Proc. Natl. Acad. Sci. USA*. 2005, **102**, 10029–10034; (b) S. Angelos, N. M. Khashab, Y. W. Yang, A. Trabolsi, H. Khatib, J. F. Stoddart and J. I. Zink, *J. Am. Chem. Soc.* 2009, **131**, 12912–12914; (c) S. Angelos, Y. W. Yang, N. M. Khashab, J. F. Stoddart and J. I. Zink, *J. Am. Chem. Soc.* 2009, **131**, 11344–11346. (d) D. P. Ferris, Y.-L. Zhao, N. M. Khashab, H.

- A. Khatib, J. F. Stoddart and J. I. Zink, *J. Am. Chem. Soc.* 2009, **131**, 1686–1688; (e) L. Du, S. Liao, H. A. Khatib, J. F. Stoddart and J. I. Zink, *J. Am. Chem. Soc.* 2009, **131**, 15136–15142; (f) C. R. Thomas, D. P. Ferris, J.-H. Lee, E. Choi, M. H. Cho, E. S. Kim, J. F. Stoddart, J.-S. Shin, J. Cheon and J. I. Zink, *J. Am. Chem. Soc.* 2010, **132**, 10623–10625.
- 13 (a) H. C. Kolb, M. G. Finn and K. B. Sharpless, *Angew. Chem. Int. Ed.* 2001, **40**, 2004–2021; (b) V. V. Rostovtsev, L. G. Green, V. V. Fokin and K. B. Sharpless, *Angew. Chem. Int. Ed.* 2002, **41**, 2596–2599.
- 14 (a) C.-H. Lee, S.-H. Cheng, I.-P. Huang, J. S. Souris, C.-S. Yang, C.-Y. Mou and L.-W. Lo, *Angew. Chem. Int. Ed.* 2010, **49**, 8214–8219; (b) Y.-L. Zhao, Z. Li, S. Kabehie, Y. Y. Botros, J. F. Stoddart and J. I. Zink, *J. Am. Chem. Soc.* 2010, **132**, 13016–13025.
- 15 N. Takahashi, T. Kishimoto, T. Nemoto, T. Kadowaki and H. Kasai, *Science* 2002, **297**, 1349–1352.
- 16 H. Meng, M. Xue, T. Xia, Z. Ji, D. Y. Tarn, J. I. Zink and A. E. Nel, *ACS Nano* 2011, **5**, 4131–4144.

Chapter 4

Probing the Microenvironment inside the Mesopores

4.1 Abstract

In this chapter, I demonstrate two experimental methods, dynamic fluorescence anisotropy and rigidochromism spectroscopy for probing the properties of the microenvironment inside the mesopores of the mesoporous silica nanoparticles. Two different probe molecules, tris(bipyridine)ruthenium(III) hexafluorophosphate (Ru-trisBPy) and tricarbonylchloro(sodium bathocuproine disulfonato)Rhenium(III) (Re-SBD) were employed. A nanovalve construction was used for differentiating probe molecules absorbed on the surface and those trapped in the pore channels. Results show that the properties of probe molecules have strong effect on the spectroscopic outcome and a total symmetric probe molecule is preferred.

Part of the work presented in this chapter was done in collaboration with my fellow group member Dr. Zongxi Li.

4.2 Introduction

Mesoporous silica nanoparticles have been widely studied in the field of drug delivery. Despite the achievements in their bioapplications, there are few studies done to reveal the physical properties of the microenvironment inside the mesopores, and to probe the interaction between the silica matrix and the guest molecules.¹ The key challenge in this type of study is to successfully distinguish the properties of the outer surface from those of the inner pores. Our group has developed a series of nanomachines that are capable of controlling the access to the pores, which can facilitate the discrimination of the pore spaces.² By grafting nanomachines at the pore opening, probe molecules can be loaded and trapped in the mesopores while those absorbed on the outer surface can be removed during subsequent washing steps. This allows us to probe primarily the inner surface with minimal interference from probe molecules either on the outer surface or in the surrounding solution.³

In this chapter, two fluorophores, tris(bipyridine)ruthenium(III) hexafluorophosphate (Ru-trisBPy) and tricarbonylchloro(sodium bathocuproine disulfonato)rhenium(III) (Re-SBD)⁴ were used as probe molecules due to their appropriate size, water solubility, long fluorescence lifetimes and decent photo stability. These probe molecules were loaded into MSNP and trapped with nanomachines. Two types of studies were conducted to probe the microenvironment inside the mesopores. Dynamic fluorescence anisotropy experiments were performed to reveal the molecule mobility inside the pores, while the rigidochromism studies were employed to detect the rigidity of the solvent matrix inside the pore.

In the dynamic fluorescence anisotropy experiments, fluorescent molecules that were encapsulated in the mesopores were irradiated by a polarized light pulse, and the fluorescence anisotropy of the emitted light was measured. The experiment setup is illustrated in Figure 4.1. Because the probability of exciting a fluorophore molecule depends on the angle between the

transition dipole and the electric field vector of the excitation light, and because the fluorophore molecules are randomly oriented, the resulting fluorescence emission is partially polarized, and this induces the fluorescence anisotropy. When the molecules are mobile in the environment, the anisotropy decays as a result of the rotational diffusion of the molecule, and the decay rate correlates to the molecule mobility.⁵⁻⁸

The second type of experiment utilizes the rigidochromic properties of certain fluorophores, which can provide information about the rigidity of the microenvironment. Generally, the position of the emission maximum of a fluorophore molecule is highly dependent on the local environment. A rigid environment results in an emission maximum at a higher energy and a loose environment shifts the maximum to lower energy, which is named the rigidochromic effect. By utilizing this effect, different properties of the microenvironment in the pores where the fluorophores are located can be revealed.⁹⁻¹¹

4.3 Experimental

Synthesis of MSNP

The MSNP synthesis is based on a well-established procedure.³ In a typical synthesis, 250 mg of cetyltrimethylammonium bromide was mixed with NaOH solution (875 μ L, 2 M) and 120 mL of H₂O. The mixture reaction was heated to 80 °C. After the temperature had stabilized, tetraethylorthosilicate (1.5 mL) was added to the solution. The solution was stirred vigorously at 80 °C for 2 h. The synthesized nanoparticles were centrifuged and washed with methanol.

Construction of Nanovalve

In order to graft nanovalves onto the MSNP, 200 mg of MSNP was suspended in 30 mL of toluene and mixed with 25 μ L of *N*-Phenylaminomethyltriethoxysilane. The mixture was stirred at room temperature under nitrogen for 24 hours. The particles were collected through

centrifugation and washed with methanol. The surfactants were removed by refluxing the nanoparticles in a mixture of 60 mL of methanol and 2.3 mL of 12 M HCl for 6 hours. The MSNP were then collected by centrifugation and washed with methanol.³

Pore Modification of MSNP

The MSNP equipped with nanovalves were further modified with positively and negatively charged groups. To achieve positive charge modification, 50 mg of nanovalve-grafted MSNP were suspended in 1.5 mL of methanol and mixed with 10 μ L of 3-aminopropyltriethoxysilane. The mixture was stirred under nitrogen at room temperature for 24 hours and the resulting nanoparticles were collected by centrifugation and washed extensively with methanol.

The negative charge modification was conducted in a similar way, where 50 mg of nanovalve-grafted MSNP was suspended in 1.5 mL of water, to which 25 μ L of 3-(trihydroxysilyl) propylmethylphosphonate monosodium aqueous solution (42%) was added. After stirring at room temperature for 24 hours, the nanoparticles were collected by centrifugation and washed with water.

Loading of Molecular Probes

The molecular probes were loaded into MSNP by soaking 10 mg of bare or nanovalve-functionalized MSNP in 2 mL of Ru-trisBPy or Re-SBD aqueous solution (0.1 mM). The mixtures were stirred at room temperature for 3 days. For bare MSNP samples, the nanoparticles were centrifuged and washed with deionized water. For the nanovalve-functionalized MSNP, the loaded samples were capped with α -cyclodextrin (50 mg) and after another 24 hours, the nanoparticles were collected by centrifugation and washed with deionized water. All samples were dried under vacuum before the spectroscopic studies were carried out.

Spectroscopic Techniques

Nanoparticles were placed in 2 mm glass culture tubes for the spectroscopic experiments. To measure dry samples, the culture tubes were evacuated with a vacuum pump and filled with argon. For nanoparticle suspensions, the samples were suspended in the desired solvents and purged with argon for 30 min before being sealed. For nanoparticle pellets, nanoparticle suspensions were centrifuged down and the supernatant was removed before the tubes were sealed under argon.

In the dynamic fluorescence anisotropy studies, the samples were excited by a Brilliant Compact Pulsed Nd:YAG laser (Quantel) through an Optical Parametric Oscillator Magic Prism (OPOTEK). A Glan-Thompson polarizer was placed used to ensure the polarity of the excitation pulse. The fluorescence was guided through a 0.3 m monochromator with a 300 groove/mm grating and subsequently dispersed onto a Roper Scientific PI-MAX gated, intensified CCD to generate time-resolved fluorescence spectra. A second Glan-Thompson polarizer was placed in front of the monochromator to select out parallel and perpendicular emission components, and a polarization scrambler was used to reduce polarization-related spectral bias. The optics were tested with an isotropic light source, with a resulting difference of $< 0.5\%$ between parallel and perpendicular intensity measurements.

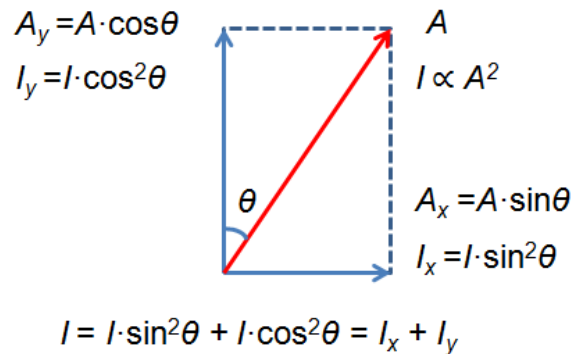
In the rigidochromic studies, the Ru-trisBPy-loaded samples were excited by a Coherent 448 nm diode laser and the Re-SBD-loaded samples were excited by a Coherent 407 nm diode laser. The laser powers were set at 2 mW to minimize any damage to the sample. The fluorescence spectra were collected by a CCD camera (Princeton Instruments) equipped with an Acton 2300i monochromator.

4.4 Results and Discussion

4.4.1 Dynamic Fluorescence Anisotropy Studies

4.4.1.1 Theories and Principles

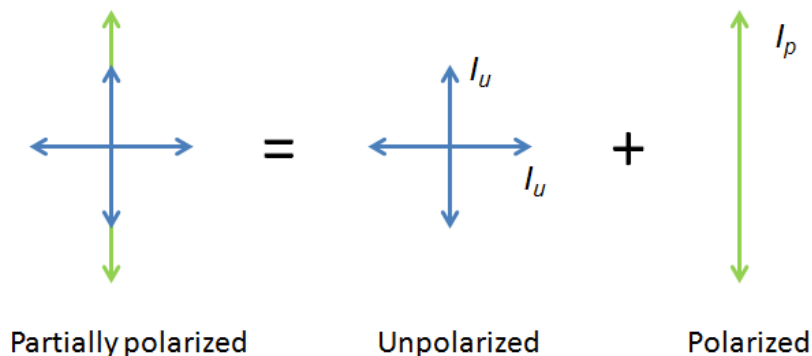
A light wave can be expressed as an oscillating electric field, the strength of which can be expressed as $E=A \cdot \cos(kx-\omega t+\varphi)$, where A is the amplitude. The energy of this light wave is described by its intensity I , which is proportional to the square of the amplitude ($I \propto A^2$). In a two dimensional Cartesian coordinate that is perpendicular to the direction of the light beam, the amplitude of this light wave can be decomposed into two orthogonal components (A_x and A_y). Consequently, the total intensity of the light wave can be expressed as the sum of intensities of those two orthogonal components (I_x and I_y).



A light beam from a natural light source is usually unpolarized, which means that it is a superimposition of different light waves with randomly orientated electric field vectors. As a result, its x and y components always have the same intensity in spite of the orientation of the Cartesian coordination. Contrarily, a polarized light beam only contains light waves whose electric field vectors are in the same direction.

In my studies, the emission from the chromophores is partially polarized, which means its intensity can be decomposed into a polarized component (I_p) and an unpolarized component (I_u). The excitation laser beam employed in my experiments is polarized in the vertical direction, which is defined as the *parallel* direction (\parallel), and the horizontal direction is defined as the *perpendicular* direction (\perp). Therefore, the polarized component can be expressed as a vector in

the *parallel* direction, while the unpolarized component can be expressed as a vector in the *parallel* direction and a vector of the same strength in the *perpendicular* direction.



It is obvious that the total intensity in the *parallel* direction is $I_{\parallel} = I_p + I_u$, while the intensity in the *perpendicular* direction is $I_{\perp} = I_u$. From this we can easily determine that the polarized component $I_p = I_{\parallel} - I_{\perp}$, while the unpolarized one $I_u = I_{\perp}$. Because the chromophores in my studies emit in three dimensions, there exists an additional perpendicular component that has the same intensity of I_{\perp} . Therefore, the total emission intensity is $I_t = I_{\parallel} + 2I_{\perp}$. We define the intensity of the polarized component over the total emission intensity as the fluorescence anisotropy (r).

$$r = \frac{I_{\parallel} - I_{\perp}}{I_{\parallel} + 2I_{\perp}}$$

When a chromophore molecule is positioned at an angle θ to the *parallel* direction and at an angle φ to the *perpendicular* direction (Figure 4.2A), suppose the emission intensity is I_0 , the emission intensity in the *parallel* direction is

$$I_{\parallel} = \cos^2\theta \cdot I_0$$

The emission intensity in the *perpendicular* direction is

$$I_{\perp} = \sin^2\theta \cdot \sin^2\varphi \cdot I_0$$

The probability of this particular molecule to be excited by the excitation beam is proportional to the intensity of the excitation beam component along the direction of this molecule, which results in a coefficient of $\cos^2\theta$. For all the randomly oriented molecules in the whole sample, the population of molecules at the angle θ is proportional to $\sin\theta$. Therefore, the excitation probability of molecules at the angle θ in the whole sample can be described as

$$P_{\theta} = \cos^2\theta \cdot \sin\theta$$

Now consider the overall emission intensity of the whole sample, we need to take into account of all the molecules, which have θ values from 0 to π .

$$I_{\parallel} = I_0 \int_0^{\pi} P_{\theta} \cos^2\theta d\theta = I_0 \int_0^{\pi} \cos^4\theta \sin\theta d\theta = \frac{2}{5} I_0$$

$$I_{\perp} = I_0 \int_0^{\pi} \int_0^{2\pi} P_{\theta} \sin^2\theta \sin^2\varphi d\varphi d\theta = \frac{2}{15} I_0$$

Therefore the intrinsic anisotropy resulted from the random orientations of the molecules in the sample, and the correlating absorption probability, is

$$r_1 = \frac{I_{\parallel} - I_{\perp}}{I_{\parallel} + 2I_{\perp}} = \frac{2}{5}$$

If the orientation of the emitting dipole moment is different from that of the absorbing dipole moment, with an angle α between these two, the loss in the emission polarization due to this angle can be calculated to be

$$r_2 = \frac{3\cos^2\alpha - 1}{2}$$

Hence, for a sample where the chromophore molecules are immobile, the total fluorescence anisotropy should be

$$r_0 = r_1 \cdot r_2 = \frac{3\cos^2\alpha - 1}{5}$$

When the chromophore molecules are mobile, the rotational diffusion of the molecules causes a decay of the fluorescence anisotropy. The decay can be described by an exponential equation, where the “lifetime” of this decay is defined as the *rotational correlation time* τ_c . The longer this correlation time is, the slower the rotational diffusion of the molecules is, therefore the less mobile the molecules are.

$$r(t) = r_0 e^{-\frac{t}{\tau_c}} = \frac{I_{\parallel}(t) - I_{\perp}(t)}{I_{\parallel}(t) + 2I_{\perp}(t)}$$

The total emission intensity also decays exponentially and this provides information about the fluorescence lifetime τ_F .

$$I(t) = I_0 e^{-\frac{t}{\tau_F}}$$

In my studies, the intensities of the *parallel* and *perpendicular* components of the sample emission are employed to generate a time-resolved fluorescence anisotropy profile, and this profile is fitted by an exponential decay equation to determine the rotational correlation time τ_c . Meanwhile, the decay of the total emission intensity is fitted using a similar exponential equation to calculate the fluorescence lifetime τ_F . These two values provide information about the effect of local environments on the fluorophore molecule.

4.4.1.2 Studies Using Re-SBD without Nanovalves

The dynamic fluorescence anisotropy studies were first performed on an aqueous solution of Re-SBD. The fluorescence lifetime τ_F is $0.99 \pm 0.01 \mu\text{s}$. The rotational correlation time is $0.105 \pm 0.001 \mu\text{s}$ (Figure 4.3). When the same experiments were performed on a pure Re-SBD solid sample, the rotational correlation time increased to $2.30 \pm 0.05 \mu\text{s}$, which can be

easily explained by the significantly decreased dye mobility in the solid sample. The lifetime decreased to $0.511 \pm 0.003 \mu\text{s}$, as a result of the increased possibility of energy transfer and fluorescence quenching in a pure solid sample.

The Re-SBD dye was first loaded into bare MSNP and dried under vacuum. The time-resolved fluorescence anisotropy studies were measured on a dry sample and on samples that were immersed in water or toluene. The rotational correlation time for the dry sample is $3.43 \pm 0.09 \mu\text{s}$ (Figure 4.4), which is much higher than that of the dye solution and also higher than the solid dye sample. This indicates that those dye molecules in the dry samples have very low mobility. Two fluorescence lifetime values, $1.6 \pm 0.1 \mu\text{s}$ and $0.44 \pm 0.02 \mu\text{s}$, exist in the dry sample, which demonstrates that there are two populations of dye molecules in the sample that are in different environments. The $0.44 \mu\text{s}$ lifetime is close to that of the solid dye sample, and possibly corresponds to dye molecules that have little interaction with the MSNP. The other component exhibits a longer lifetime, which is probably due to the strong interaction between these dye molecules and the silica matrix.

When the Re-SBD loaded sample was immersed in water, two components emerged while fitting the fluorescence correlation time. One of them has a correlation time of $0.09 \mu\text{s}$, which is comparable to that of a dye solution. This population indicates that some dye molecules are dissolved into the solution and therefore become very mobile. The other component exhibits a correlation time of $2.1 \mu\text{s}$, which is smaller than that of the dry sample. This proves that solvent molecules are getting into the pore channels and increasing the mobility of the dye molecules. There are two different components for the fluorescence lifetime; both of them are smaller than those from the dry sample. This also indicates that the water molecules are weakening the interactions between the dye molecule and the silica matrix.

The sample immersed in toluene gave a single fluorescence correlation time of $1.11 \pm 0.04 \mu\text{s}$, which is because the dye molecules do not dissolve in toluene. This value is higher than those in water, but lower than those of the dry sample. This demonstrates that the dye molecules have a lower mobility in toluene than in water, which is consistent with the higher viscosity of toluene.

The results for the above five samples demonstrated that the τ_c and τ_F values can be used to measure the mobility of the dye molecules in the pore as well as the interaction between the dye molecules and the silica matrix. All results are summarized in Table 4.1.

4.4.1.3 Studies Using Re-SBD with Nanovalves

In order to differentiate the dyes that are in the pore channels versus those are absorbed to the outer surface of MSNP, a nanovalve functionalization was introduced. The nanovalve employed here is a well-established pH-sensitive nanovalve that will keep the pore closed at neutral pH and thus trap the dye in the pore. The dye molecules that are absorbed to the outer surface of MSNP can therefore be washed off without any impact towards those in the pore channels.

Three different charge modifications of the pore walls were employed in these studies. Two fluorescence lifetimes which were different from that of the Re-SBD solution were obtained for each sample. The fluorescence correlation times for the amine modified sample (positively charged, zeta potential +35 mV) is $1.56 \mu\text{s}$, for the bare silanol surfaced sample (negatively charged, zeta potential -20 mV) is $1.95 \mu\text{s}$, and for the phosphonate modified sample (negatively charged, zeta potential -35 mV) is $2.65 \mu\text{s}$ (Figure 4.5). The results are summarized in Table 4.2. These results demonstrate that the mobility of the Re-SBD molecules increases as more positively charged groups were introduced into the pore. This is contradictory to the simple assumption that the Re-SBD dye should become less mobile in a positively charged

environment since it is negatively charged and could be attracted electrostatically to the pore walls. However, considering that the Re-SBD dye molecule has asymmetrically distributed charge and hydrophobic region, there is a simple model that explains why the results did not dovetail with the electrostatic attraction assumption.

Figure 4.6 illustrates a possible model to explain this result. In this model, the distance of the Re-SBD molecule from the pore wall depends on four factors: the interaction between water molecules and charged groups on the silica surface; the thickness of the effective charged layer; the strength of the interaction between Re-SBD molecules and the charged groups; and the orientation of the Re-SBD molecules inside the pore channels. These factors complicate the system and make it difficult to predict the behavior of the Re-SBD molecules in the pores. We can infer that the Re-SBD molecules are oriented in such way that the hydrophobic part is pointing to the middle of the pore, where the solvent molecules are less dense and less rigid. In the amine-modified sample, the Re-SBD molecule is not close to the pore surface, possibly because of the strong interaction between the water molecules and the amine groups. This results in a relatively loose environment for the Re-SBD dye and therefore it moves more easily. In the phosphonated sample, there is a much stronger interaction between the water molecules and the Re-SBD molecules, which causes the Re-SBD molecule to become more mobile. This model correlates well with the result from rigidochromism studies that are described later in this chapter. However, in order to further understand the result and to further probe factors such as the orientation of the molecules, much more sophisticated studies must be conducted and they are beyond the scope of this chapter.

4.4.1.4 Studies Using Ru-trisBPy

The Ru-triBPy was chosen as an alternative probe molecule due to its totally symmetric distribution of charge and hydrophobicity, as well as the minimized possibility of interference

from the counter ion (hexafluorophosphate) and the interaction with silanol groups. A fluorescence anisotropy study was first performed on a Ru-triBPY aqueous solution, which gave a correlation time of 0.43 μs and a fluorescence life time of 0.41 μs (Figure 4.7).

Similar to the studies using Re-SBD, nanovalve-modified MSNPs were loaded with Ru-triBPY and capped with cyclodextrin. The surface absorbed Ru-triBPY was removed via extensive washing. The MSNP was first suspended in water and the suspension was then centrifuged to form a wet pellet. The supernatant was carefully removed. This was done in order to minimize potential interferences originating from particles' tumbling. The fluorescence anisotropy measurements were carried out using these wet pellets of MSNPs.

Cationic and anionic charge modifications were introduced during the MSNP synthesis as described in previous sections. The amine-modified, positively charged sample gave a fluorescence correlation time of 0.75 μs and a fluorescence lifetime of 1.15 μs (Figure 4.7). This increased lifetime is consistent with the result of previous studies, and indicative of the entrapment of Ru-triBPY inside the pores. The fluorescence correlation time is almost double that in solution, which proves that the Ru-triBPY molecules are in a restrained environment and their mobility is limited.

The phosphonated and the unmodified samples gave fluorescence lifetimes of 0.84 μs and 0.80 μs , respectively, which are similar between each other, but different from the values from solution studies and amine-modified samples. This indicates that the Ru-triBPY molecules are in a different environment and this may be due to the negatively charged pore surfaces in the phosphonated and the unmodified samples. The unmodified sample exhibited a fluorescence correlation time of 1.3 μs and the phosphonated sample gave 1.48 μs . These values are much larger than that of the amine-modified sample, which reveals that Ru-triBPY

molecules are much less mobile in these negatively charged environments than in a positively charged one.

This result is expected because the Ru-triBPY cation is positively charged and the charge distribution is symmetric. In the negatively charged samples, the Ru-triBPY molecules are most likely adsorbed onto the pore wall because of the electrostatic attraction, which significantly decreases their mobility. On the contrary, the positively charged wall in the amine-modified sample does not have strong affinity towards Ru-triBPY cations. As a result, the Ru-triBPY molecules can move more freely. This demonstrates that Ru-triBPY can serve as a good probe in dynamic fluorescence anisotropy studies. The results of this section are summarized in Table 4.3.

4.4.2 Rigidochromic Spectroscopy

4.4.2.1 Theories and Principles

When a fluorophore molecule is placed in a solvent, the solvent dipole moments are oriented by the fluorophore's molecular dipole moment (Figure 4.8). During an excitation process, if the dipole moment of a fluorophore molecule changes its direction, it becomes misaligned with the solvent dipoles. Consequently, the fluorophore molecule appears to be at an excited state with a slightly higher energy level than that of a molecule excited in vacuum. When the solvent matrix is rigid, the solvent dipole moment cannot realign before the emission from the excited fluorophore molecule occurs. This leads to a blue-shift of the emission band maximum. In the contrast, when the solvent matrix is loose and the solvent molecules are free to move, the realignment occurs faster than the emission process, and the emission band maximum thus appears at a longer wavelength.

4.4.2.2 Studies using Re-SBD

As shown in Figure 4.9, the emission maximum of the Re-SBD in positively charged pores is around 590 nm, which is similar to that of the dye solution (580 nm). In the negatively charged samples, i.e. the phosphonated and the bare silanol samples, the probe emission exhibits relatively lower emission maxima around 560 nm. This means that the environments in negatively charged pores (phosphonated and bare silanol samples) are more rigid than that in the positively charged pores. This result can be explained by the proposed model described in section 4.4.1.3. In that model, there are fewer water molecules surrounding the Re-SBD molecule in the positively charged pores and more water molecules around the probe in the negatively charged pores, as a result of the various locations of the Re-SBD molecules in different samples. However, it must be noted that many other factors will pose strong influences on the result; these include the distance between the Re-SBD and the pore wall, the interaction between the water molecules and the Re-SBD molecules, the orientation of the Re-SBD molecules inside the pores, etc. The unsymmetrical nature of the charge distribution and the hydrophobicity of the Re-SBD molecule make it difficult to elucidate the properties of the microenvironment and to form a comprehensive conclusion.

4.4.2.3 Studies using Ru-triBPY

The symmetric Ru-triBPY molecule has been demonstrated to be a good probe in dynamic fluorescence anisotropy studies described in section 4.4.1.4. This feature simplifies its interactions between the water molecules and the pore walls. The rigidochromic effect of Ru-triBPY is not as great as that of Re-SBD; however, the shift of the emission maxima fits well with expectation. As shown in Figure 4.10, the emission maximum of Ru-triBPY solution is at 615 nm whereas the maxima for negatively charged samples (the phosphonated and the silanol surfaces) are at 612 nm and 609 nm, respectively. The positively charged amine-modified sample gives an emission maximum of 603 nm. This result suggests that the Ru-triBPY molecules are in a less rigid environment as the surrounding environment becomes more

positively charged, which is consistent with the trend in section 4.4.1.4, where a positively charged environment leads to a faster tumbling rate. As the environment becomes more positively charged, the distance between the Ru-triBPY molecule and the pore wall increases. This accounts for the decreased rigidity of the local environment because the solvent molecules are significantly less rigid than the silica matrix, and the layer of water molecules close to the pore wall are more rigid than those in the middle of the pore. This result demonstrates that Ru-trisBPY can serve as a rigidochromic probe for revealing the rigidity of local microenvironments.

4.5 Summary

In this chapter, I have demonstrated two methods capable of probing the microenvironment inside the MSNP pore channels. Dynamic fluorescence anisotropy studies utilize the tumbling rate of a probe molecule to reveal the properties of local environments, and rigidochromic studies can be used to determine the rigidity of the solvent matrix. The employment of the nanovalve construction can help differentiate the probe molecules on the outer surface versus those in the pore channels, as the outer surface ones can be removed through extensive washing. The properties of probe molecules have strong effects on the spectroscopic results and a total symmetric molecule with less specific interaction with the matrix is strongly preferred.

4.6 Tables and Figures

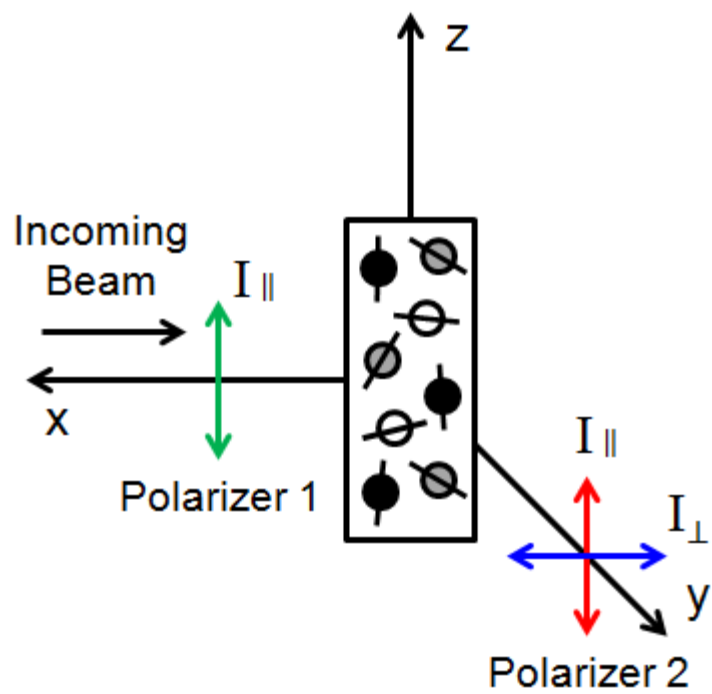


Figure 4.1. Illustrations of the fluorescence anisotropy experiment.

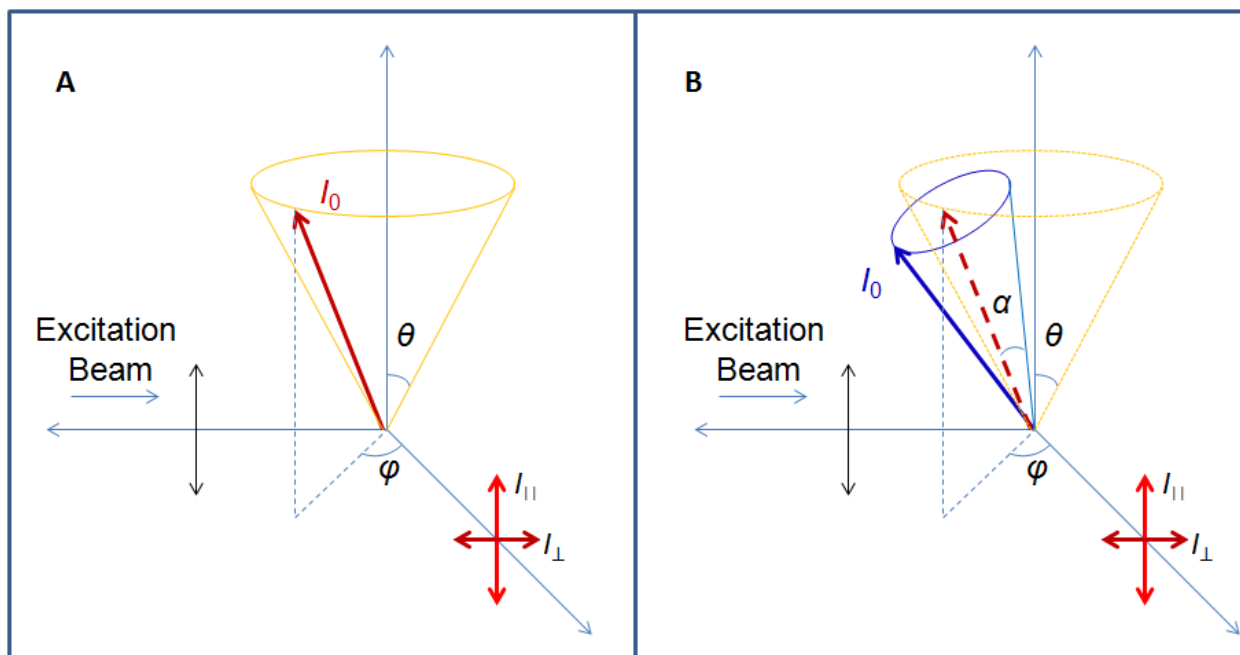


Figure 4.2. Principles of fluorescence anisotropy. **(A)** Anisotropy from the orientation of the fluorophore in regard of the excitation beam. **(B)** Additional anisotropy from the angle between the adsorption and emission dipole moments.

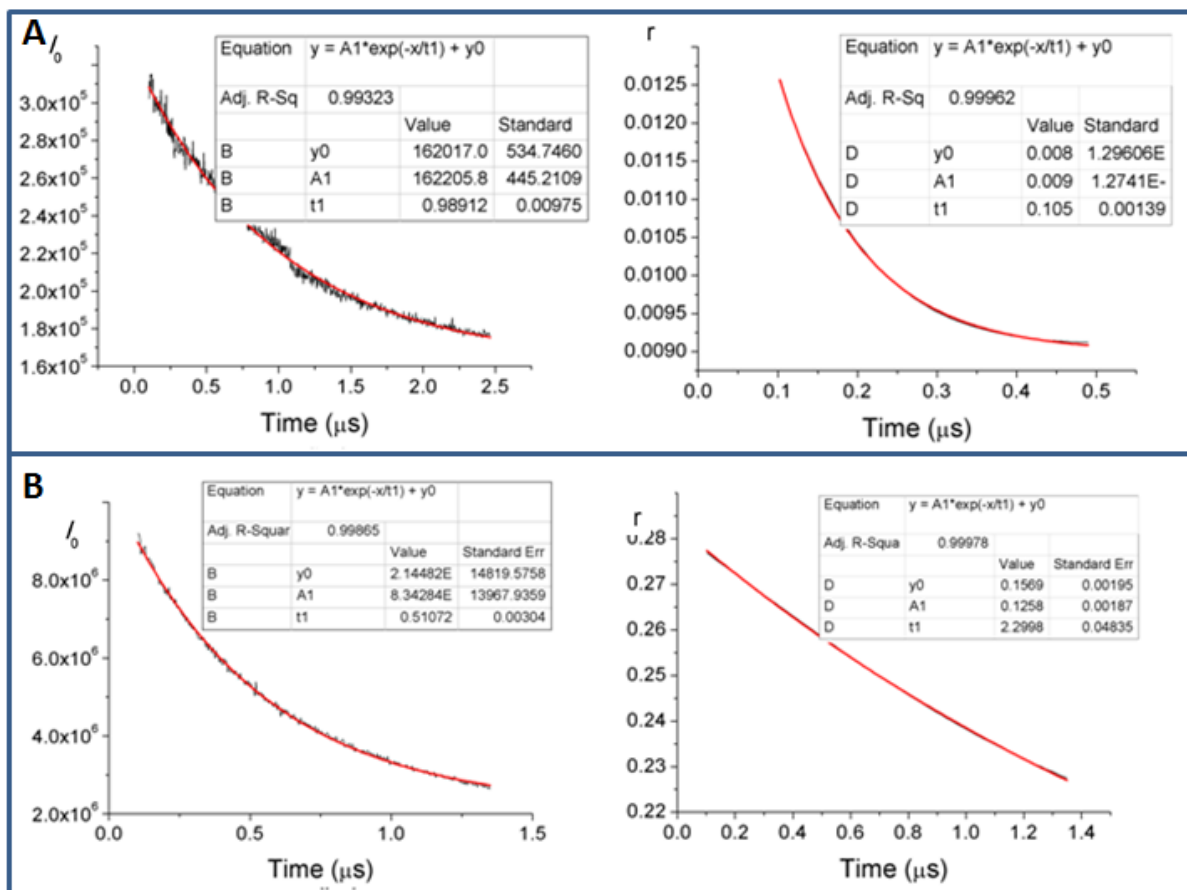


Figure 4.3. The total fluorescence intensity profile (**left**) and the fluorescence anisotropy profile (**right**) of **(A)** the aqueous solution of Re-SBD and **(B)** the pure solid sample of Re-SBD.

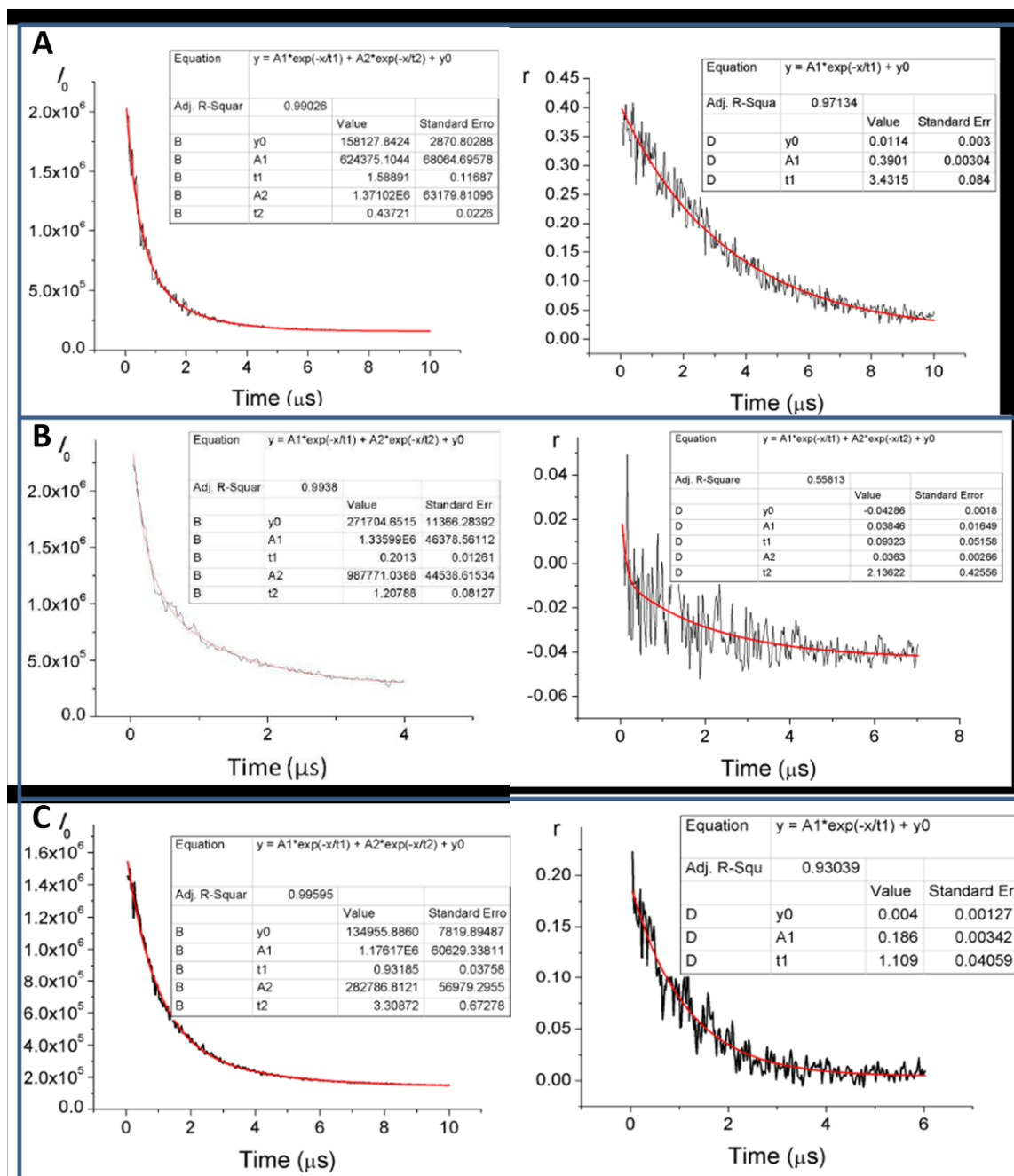


Figure 4.4. The total fluorescence intensity profile (left) and the fluorescence anisotropy profile (right) of Re-SBD loaded MSNP without nanovalves. **(A)** Dry solid sample. **(B)** Sample in water. **(C)** Sample in toluene.

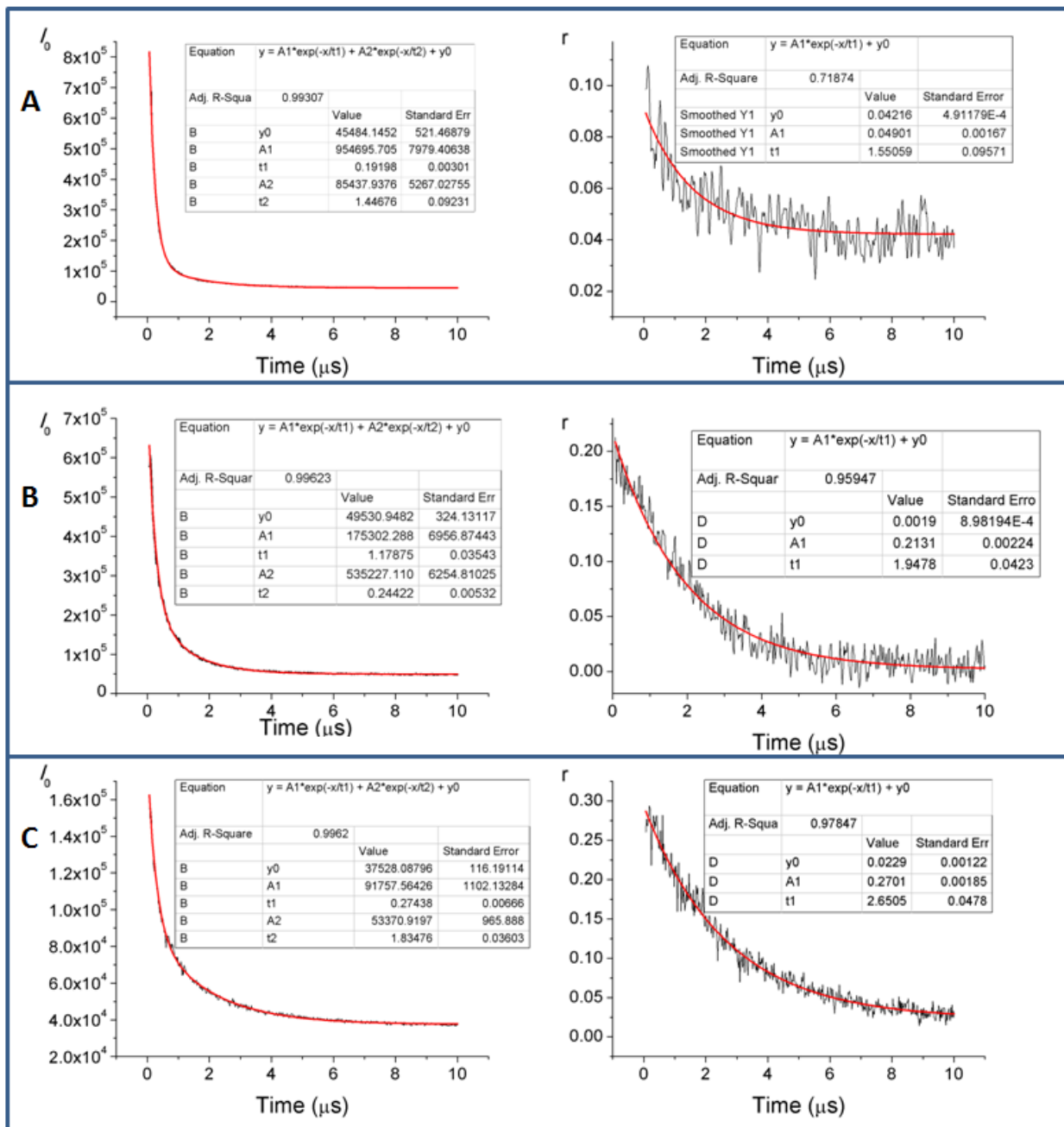


Figure 4.5. The total fluorescence intensity profile (left) and the fluorescence anisotropy profile (right) of Re-SBD loaded MSNP with nanovalves in water. **(A)** Amine-modified sample. **(B)** Silanol surface (unmodified) sample. **(C)** Phosphanated sample.

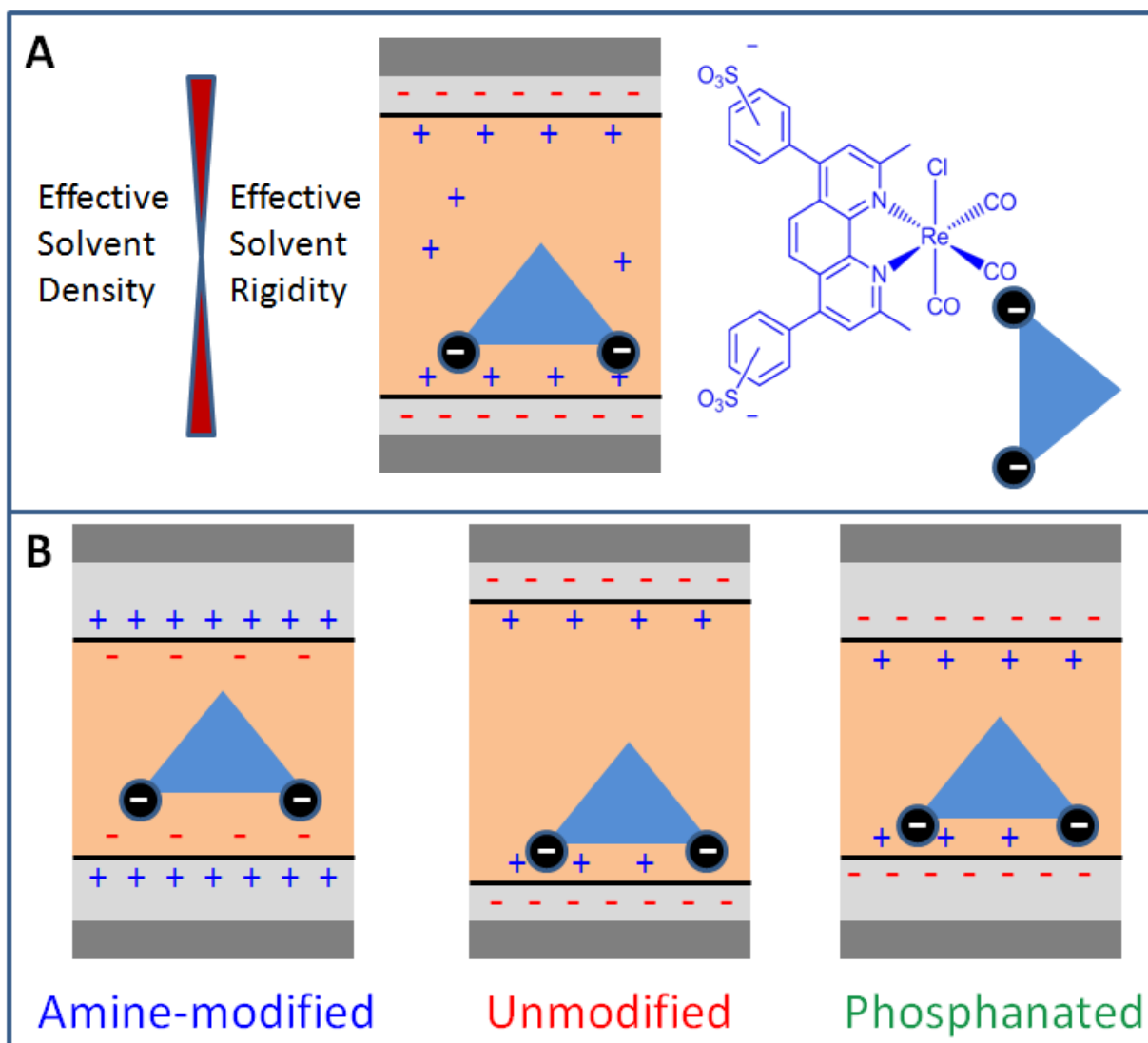


Figure 4.6. A proposed model explaining the results using Re-SBD dye. **(A)** The effective solvent rigidity and density distribution inside the pore channel. **(B)** The distance between the Re-SBD molecule and the pore wall in different charge modified samples.

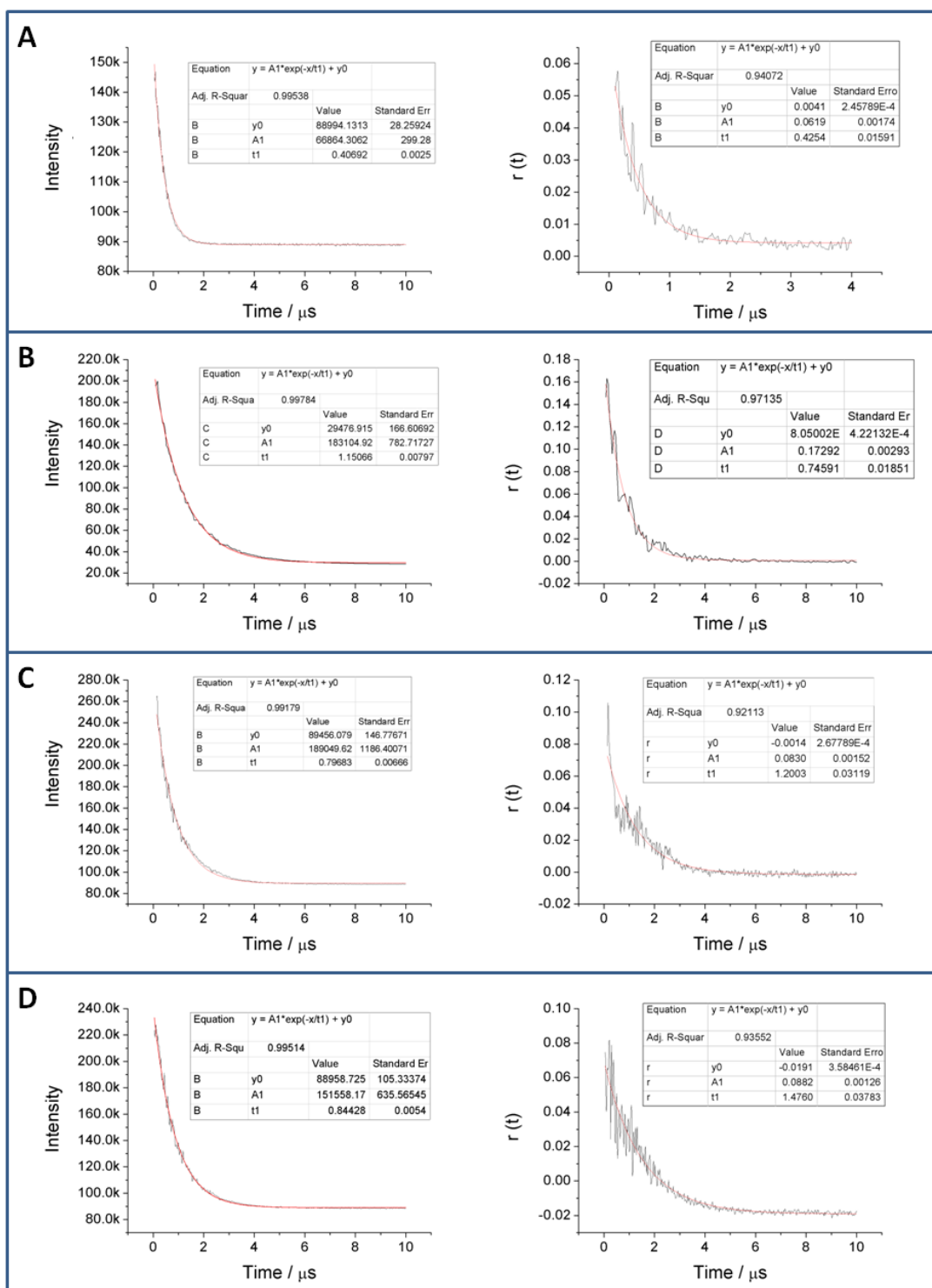


Figure 4.7. The total fluorescence intensity profile (**left**) and the fluorescence anisotropy profile (**right**) of **(A)** Ru-triBPY solution, and Ru-triBPY loaded MSNP with nanovalves in water for **(B)** amine-modified sample, **(C)** silanol surface (unmodified) sample, **(D)** phosphanated sample.

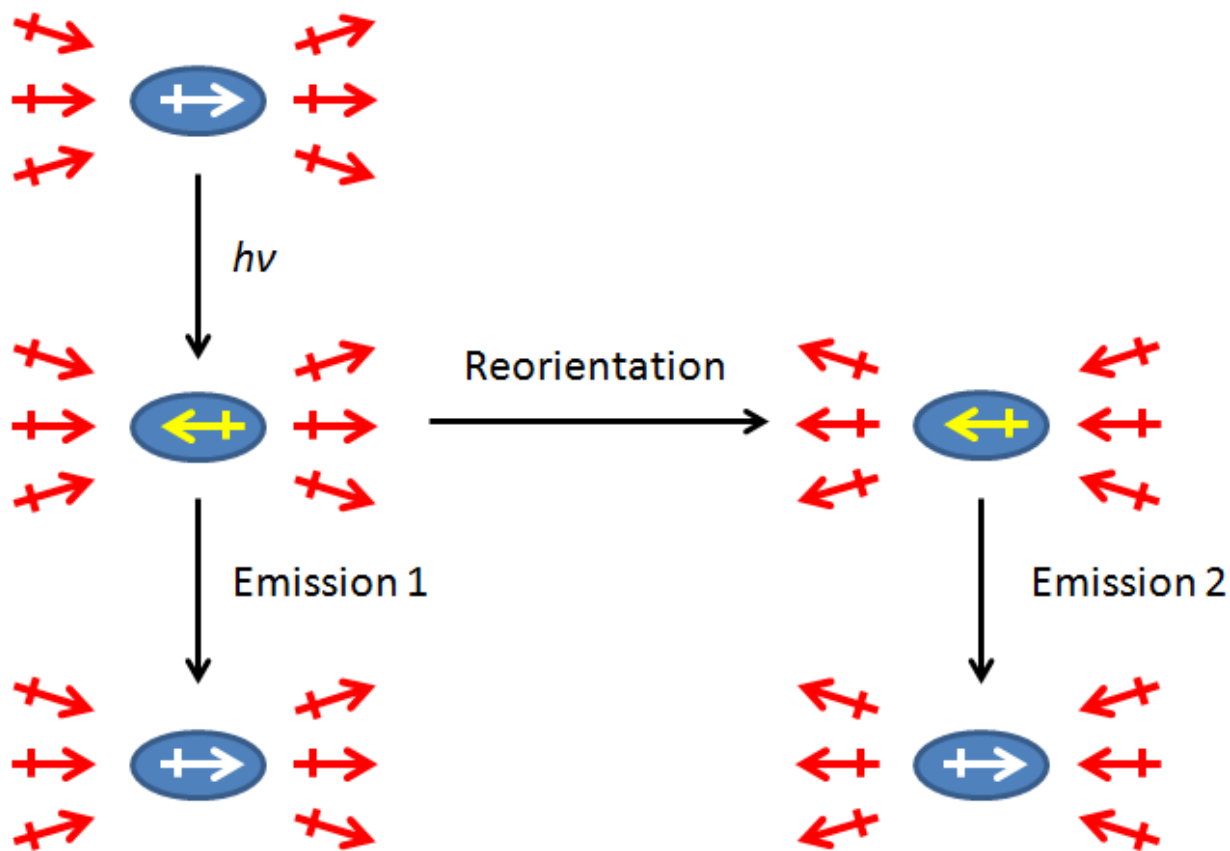


Figure 4.8. Schematic illustration of the origin of the rigidochromic effect. The rate of the solvent dipole moments reorientation relative to the excited state lifetime of the fluorophore determines the energy of the emission. Slower reorientation results in a higher energy emission. In this case, emission 1 is blue-shifted versus emission 2.

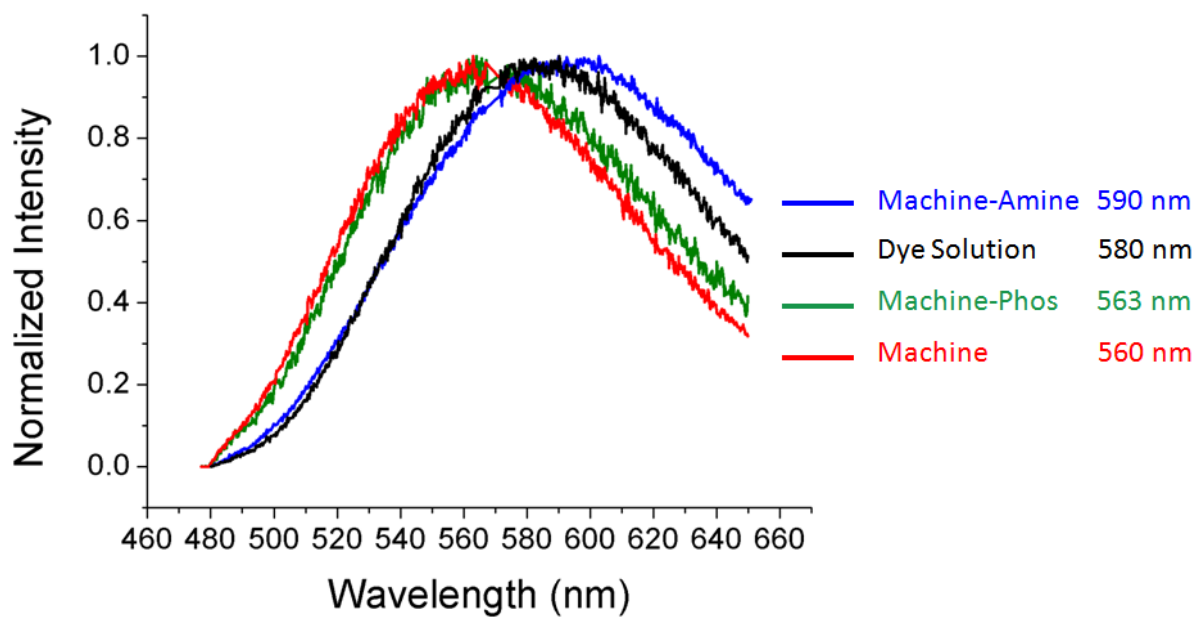


Figure 4.9. Emission spectra of Re-SBD solution and Re-SBD loaded samples showing the rigidochromic effect.

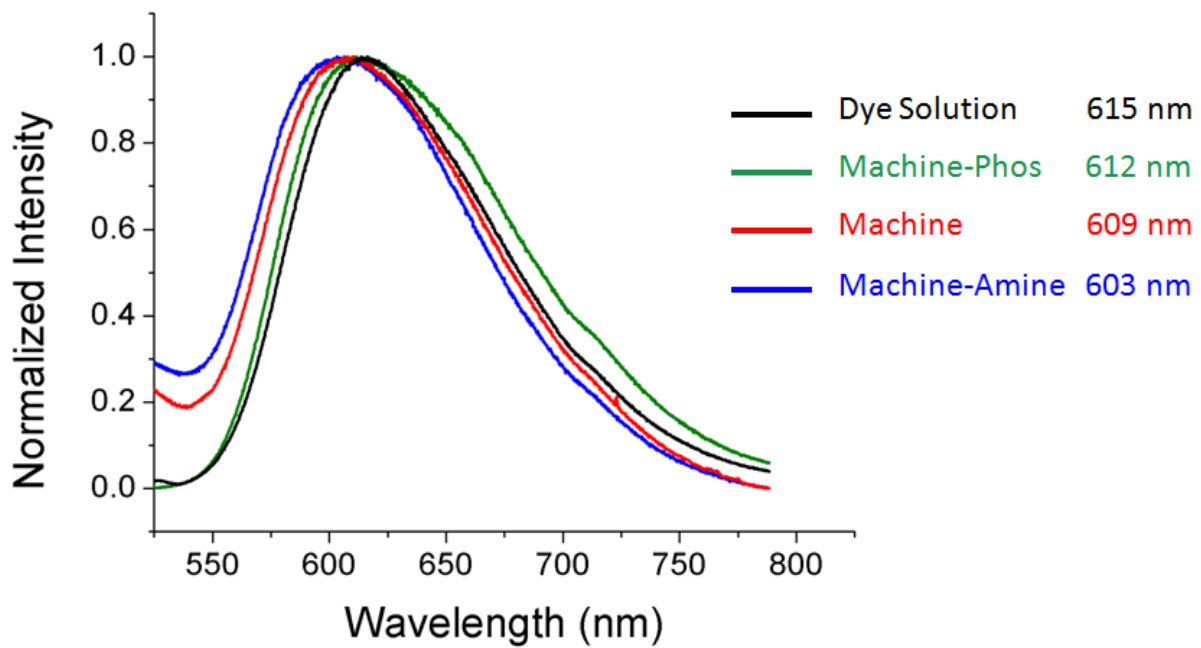


Figure 4.10. Emission spectra of Ru-triBPY solution and Ru-triBPY loaded samples showing the rigidochromic effect.

Table 4.1. Fluorescence lifetimes and correlation times of Re-SBD solution, Re-SBD solid, Re-SBD loaded dry MSNP, Re-SBD loaded MSNP in water and in toluene.

Re-SBD Samples	Fluorescence Lifetime (μs)		Fluorescence Correlation Time (μs)	
	T_{F1}	T_{F2}	T_{C1}	T_{C2}
Solution	0.99 ± 0.01	--	0.105 ± 0.001	--
Solid Dye	0.511 ± 0.003	--	2.30 ± 0.05	--
Loaded MSNP dry	1.6 ± 0.1	0.44 ± 0.02	3.43 ± 0.08	--
Loaded MSNP in water	1.21 ± 0.08	0.20 ± 0.01	2.1 ± 0.4	0.09 ± 0.05
Loaded MSNP in toluene	3.3 ± 0.7	0.93 ± 0.04	1.11 ± 0.04	--

Table 4.2. Fluorescence lifetimes and correlation times of Re-SBD loaded nanovalve-modified MSNP in water. Three different charge groups are employed: amine-modified, unmodified and phosphanate modified.

Re-SBD Samples	Fluorescence Lifetime (μs)		Fluorescence Correlation Time (μs)
	T_{F1}	T_{F2}	T_C
Amine	1.45 ± 0.09	0.192 ± 0.003	1.6 ± 0.1
Unmodified	1.18 ± 0.04	0.244 ± 0.005	1.95 ± 0.04
Phosphanated	1.83 ± 0.04	0.274 ± 0.007	2.65 ± 0.05

Table 4.3. Fluorescence lifetimes and correlation times of Ru-triBPy solution and Ru-triBPy loaded nanovalve-modified MSNP in water. Three different charge groups are employed: amine-modified, unmodified and phosphanate modified.

Ru-triBPy Samples	Fluorescence Lifetime (μs)	Fluorescence Correlation Time (μs)
	T_{F1}	T_C
Ru-triBPy Solution	0.407 ± 0.003	0.43 ± 0.02
Amine	1.151 ± 0.008	0.75 ± 0.02
Unmodified	0.797 ± 0.007	1.20 ± 0.03
Phosphanated	0.844 ± 0.005	1.48 ± 0.04

4.7 References

1. Dunn, B.; Zink, J. I., *Chem. Mater.* **1997**, 9, (11), 2280-2291.
2. Tarn, D.; Ashley, C.E.; Xue, M.; Carnes, E.C.; Zink, J.I.; Brinker, C.J. *Acc. Chem. Res.* **2013**, 46, 792-801.
3. Du, L.; Liao, S.; Khatib, H. A.; Stoddart, J. F.; Zink, J. I., *J. Am. Chem. Soc.* **2009**, 131, 15136-15142.
4. Kunkely, H.; Vogler, A., *Mater. Chem. Phys.* **2008**, 109, 506-509.
5. Straume, M.; Litman, B. *J. Biochemistry* **1987**, 26, 5121-5126.
6. Clayton, A.H.A.; Hanley, Q.S.; Arndt-Jovin, D.J.; Subramaniam, V.; Jovin, T.M. *Biophys J.* **2002**, 83, 1631-1649.
7. Valeur, B. *Molecular Fluorescence: Principles and Applications* **2001** Wiley-VCH.
8. Lakowicz, J.R. *Principles of Fluorescence Spectroscopy* **2006** Springer.
9. McKiernan, J.; Pouxviel, J.C.; Dunn, B.; Zink, J.I. *J. Phys. Chem.* **1989**, 93, 2129-2133.
10. Itokazu, M.K.; Polo, A.S.; Iha, N.Y.M. *J. Photochem. Photobio. A: Chem.* **2003**, 160, 27-32.
11. Rivera, E.J.; Barbosa, C.; Torres, R.; Rivera, H.; Fachini, E.R.; Green, T.W.; Connick, W.B.; Colon, J.L. *Inorg. Chem.* **2012**, 51, 2777-2784.

Chapter 5

A Chemical Amplifier Based On Enzyme-Encapsulated Mesoporous Silica Nanoparticles

5.1 Abstract

A chemical amplifier was constructed based on enzyme-encapsulated mesoporous silica nanoparticles. By employing a supramolecular nanogate assembly that is capable of controlling the access to the encapsulated enzyme, selectivity towards substrate sizes is enabled. With the pH-responsive feature of the nanogate system, an autonomously amplifying chemical process can be initiated by a proper combination of the nanogate and the substrate. This study demonstrates the first example of a chemical amplifier that is activated by and also amplifies the same type of reaction.

5.2 Introduction

Enzymes have been widely used in biosensors due to its highly specific catalytic properties.¹⁻²⁰ In most of those biosensors, an enzyme is attached to a moiety that is capable of recognizing certain molecules of interest, and a separate chemical process catalyzed by the enzyme is employed to quantify the enzymatic activity, which can be translated to the quantity of the recognized molecule.³⁻⁸ This process is sometimes referred as an enzymatic amplification, where the output signal resulted from the enzymatic reaction is non-stoichiometrically associated with the amount of the originally recognized molecule. Typical designs of these enzymatic amplifiers require a different type of chemical reaction during the amplification from that during the recognition. In this chapter, I present the operation of an enzymatic chemical amplifier that utilizes the same type of chemical reaction to achieve enzymatic amplification. The amplifier consists of two parts: a mesoporous silica matrix with encapsulated enzymes that maintains the enzymatic activity, and a pH-responsive supramolecular nanogate assembly that controls the substrate access towards the enzyme. I first demonstrate that the nanogate system enables substrate-size selectivity for the encapsulated enzyme. Then, I show that the operation of the nanogate system can be activated by the enzymatic process. Consequently, an autonomously amplifying chemical process can be initiated by a proper combination of the nanogate and the substrate.

5.3 Experimental

5.3.1 Synthetic Procedures

Mesoporous Silica Nanoparticles (MSNP): The synthesis of mesoporous silica nanoparticles using Pluronic P104 is based on published procedure.²¹ In a typical synthesis, 0.35 g of P104 was dissolved in 13.2 mL of HCl (1.6 M). The solution was stirred at 56 °C for an hour before

0.53 g of tetramethyl orthosilicate (Sigma Aldrich, 99%) was added. The solution was stirred at 56 °C for another 24 hours and the resulting white precipitates were collected via centrifugation. The nanoparticles were washed with H₂O and methanol dried under vacuum.

MSNP-Aldehyde: 1 g of the as-synthesized MSNP was resuspended in 50 mL of toluene and degassed with Argon. 300 μ L of 1-butylaldehydetriethoxysilane (Gelest, 90%) was added into the suspension drop wise. The suspension was then stirred at 80 °C under Argon for 10 hours and then cooled to room temperature. The resulting MSNP-Aldehyde was collected through centrifugation and washed with methanol. The P104 surfactant was then removed using a soxhlet extraction with methanol and 5 % HCl under Argon. The extracted MSNP-Aldehyde was then dried under vacuum.

MSNP-Cyclodextrin: 500 mg of extracted **MSNP-Aldehyde** was suspended in 50 mL of anhydrous dimethylformamide (DMF) and mixed with 500 mg of 6-(2-aminoethyl)amino-6-deoxy- β -cyclodextrin²² and 500 mg of anhydrous MgSO₄. The mixture was heated at 60°C for 24 hr under Argon. After cooling to room temperature, the resultant precipitates were collected by filtration and washed with H₂O. The product was dried under vacuum.

MSNP-Cyclodextrin-Amine: The reduction of the imine bond was carried out following published procedure.²³ 350 mg of **MSNP-Cyclodextrin** was suspended in 20 mL of anhydrous DMF under Argon and 200 mg of NaBH₄ (Sigma Aldrich, 96%) was added portion wise. The mixture was stirred at room temperature for 5 hours and the product was collected through centrifugation, washed with DMF and H₂O, and dried under vacuum.

Loading of Porcine Liver Esterase: 100 mg of **MSNP-Cyclodextrin** or **MSNP-Cyclodextrin-Amine** was suspended in a mixture of pH 7.4 PBS buffer (6 mL) and dimethyl sulfoxide (DMSO,

2 mL) at 4 °C. This suspension was mixed with 200 uL of Porcine Liver Esterase suspension (Sigma Aldrich, in 3.2 M ammonium sulfate, > 150 units/mg protein, 5 kU/ mL). This mixture was stirred at 4 °C for two days.

Capping the Nanogate: The hexamer cap molecules were synthesized through a Cu-catalyzed azide-alkyne coupling reaction following an established procedure.²² 30 mg of this capping molecule was dissolved in 1 mL of DMSO and added into the previous loading mixture. The suspension was further stirred at 4 °C for 5 hours and the resulting nanoparticles were collected through centrifugation. The excess amount of adsorbed esterase was removed by extensively washing the nanoparticles with a 3:1 mixture of pH 7.4 PBS buffer and Polyethylene glycol (Sigma Aldrich, MW. 2000). For the **No-Capping control** samples, the loaded nanoparticles were directly centrifuged without adding any capping molecules and then washed extensively with PBS-Polyethylene glycol mixture. All nanoparticles were dried under vacuum after washing.

5.3.2. Operation of the Enzymatic Amplifier

Generation of Conversion Profiles: The conversion profiles were generated using a continuous-monitoring fluorescence spectroscopic method. Generally, a solution of substrate (4-acetoxycinnamic acid, ACA; or 5-carboxyfluorescein diacetate, CFDA) was gently stirred in a cuvette and an excitation laser beam was directed into the solution. Nanoparticle samples were carefully added into the cuvette to start the enzyme process. The solution fluorescence was constantly recorded by a CCD camera and the fluorescence intensity was plotted over the time course to generate conversion profiles.

Studies Using ACA: 6 mL of ACA solution (0.2 mg/mL in 25 mM pH 8.0 TAPS buffer) and 6 mg of nanoparticle samples were employed in each experiment. A 351 nm laser (15 mW) was used

as the probe beam and the corresponding fluorescence intensity between 430 nm and 460 nm was integrated to generate conversion profiles. The 100% conversion point was determined through UV-vis spectroscopy by measuring the absorbance of the supernatant after 72 hours of reaction.

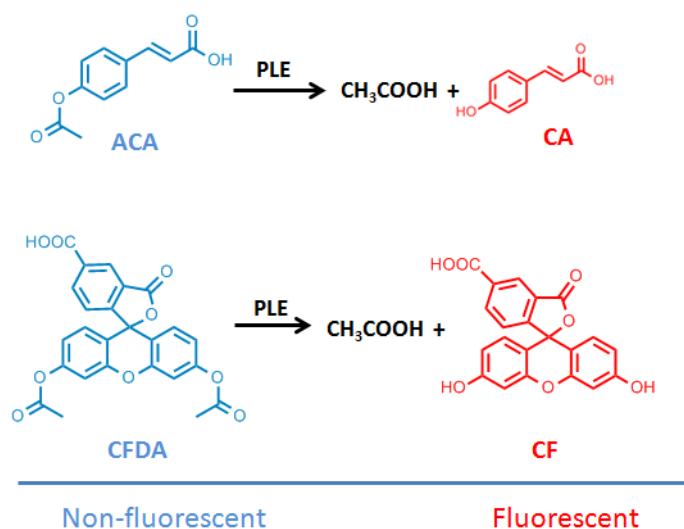
Studies Using CFDA: 6 mL of CFDA solution (0.1 mg/mL in 3 mL H₂O and 3 mL DMSO) and 6 mg of nanoparticle samples were employed in each experiment. 200 μ L of ACA solution (0.2 mg/mL in H₂O) was added together with the nanoparticles when needed. A 448 nm laser (5 mW) was used as the probe beam and the corresponding fluorescence intensity between 530 nm and 550 nm was integrated to generate conversion profiles. The 100% conversion point was determined through UV-vis spectroscopy by measuring the absorbance of the supernatant after 72 hours of reaction.

5.4 Results and Discussion

Various types of enzyme encapsulation or immobilization have been widely studied.^[9-20] In this study, I use mesoporous silica nanoparticles that are synthesized through a sol-gel process, where a tri-block copolymer (Pluronic P104) serves as a templating agent.²¹ The resulting material exhibits pore sizes around 6.5 nm, determined from N₂ adsorption-desorption measurements (Figure 5.1). The rod-shaped nanoparticles are around 300 x 500 nm, which was determined by TEM images (Figure 5.2). The pore structure provides ample space for the encapsulation of the porcine liver esterase, which has a hydrodynamic radius of around 4 nm.²⁴

In order to successfully encapsulate the model enzyme as well as to enable the substrate-size selectivity towards the enzymatic activity, a previously-established pH-responsive supramolecular nanogate assembly was constructed at the pore opening.²² This nanogate

consists of two components: β -cyclodextrin molecules that are grafted onto the silica surface through imine bonds, and an adamantane cluster molecule that exhibits a star-like structure, which can form an inclusion complex with the cyclodextrin moieties. (Figure 5.3A) When the adamantane cluster is introduced into the system, those that expand over the pore openings will block the pore entrance and therefore only those molecules with small enough sizes can diffuse in and out of the pores. Additionally, the pH-sensitive imine bonds can be cleaved under acidic conditions, in which case the cyclodextrin molecules together with the included adamantane cluster will move away from the pore opening and allow molecules to freely diffuse through the pore opening. In the scenario where the conversion of the substrates generates acids, the acid can activate the nanogate and open the access to the enzyme. This will facilitate the conversion of more substrate molecules and accelerate the reaction rate, which results in an autonomously amplifying chemical process. (Figure 5.3B)



In this study, the cyclodextrin-modified silica nanoparticles were loaded with porcine liver esterase (PLE) and then capped with the adamantane cluster molecules. Enzymes that were not successfully capped by the nanogate were removed through extensive washing with polyethylene glycol (MW 2000).²⁵ Two substrates with different sizes (4-acetoxycinnamic acid

and 5-carboxyfluorescein diacetate) were chosen to serve as model substrate molecules. These substrates exhibit no fluorescence before undergoing enzymatic reactions, but the resulting products (*p*-coumaric acid, CA; and 5-carboxyfluorescein, CF) are strongly fluorescent. Fluorescence spectroscopy was employed to quantify the conversion of the substrate. A substrate solution was stirred at room temperature and silica nanoparticles loaded with enzymes were added into the solution to initiate the enzymatic process. A probe beam was used to excite the product molecules, fluorescence and the corresponding spectra were recorded over the course of the experiment to generate a conversion profile.

4-acetoxycinnamic acid (ACA) molecules are small enough to pass through the nanogate.²⁶ As shown in Figure 5.4, ACA molecules were hydrolyzed by the encapsulated enzyme to produce fluorescent CA molecules, indicating that the ACA molecules were able to get through the nanogate and catalyzed by the enzyme (red curve). When the silica nanoparticles were not loaded with enzyme, the conversion rate in the corresponding experiment (green curve) was as slow as that of the autonomous hydrolysis of ACA in the buffer solution (black curve). In another control experiment, the nanoparticles were loaded with enzyme, but no capping agent was employed. In this case, the loaded enzymes were removed by ethylene glycol during the washing step. As a result, there was no distinct enzyme activity either (blue curve). These experiments proved that enzymes can be trapped into the mesopores of silica nanoparticles by the nanogate molecules, and the ACA molecules are small enough to pass through the nanogates and to be catalyzed by the encapsulated enzymes.

On the contrary, 5-Carboxyfluorescein diacetate (CFDA) molecules are too big to freely enter the gated pore (Figure 5.5B, green curve). This size-selectivity corresponds well with our previous studies,²³ and allows us to demonstrate the operation of the chemical amplification process. As shown in Figure 5.5B, when enzyme-loaded silica nanoparticles were added into the CFDA solution, the conversion of CFDA molecules was extremely slow, which was due to

the incapability of CFDA to pass through the nanogate and be converted by the esterase. In the contrast, when a small amount of ACA was introduced together with the silica nanoparticles, a significantly faster conversion process of CFDA was observed (Figure 5.5B, red curve). Because of their small sizes, the ACA molecules were able to enter the pore and were converted by the esterase, which generated acetic acid. The resulting acid activated the nanogate and opened the access of the CFDA molecules to the esterase. Since the conversion of CFDA itself also generates acetic acid, which can activate a neighboring nanogate and open the access to more enzymes. Therefore, this process became self-accelerating and therefore appeared to be an autonomously amplifying chemical process.

In order to prove the mechanism of this chemical amplifier, several control experiments were conducted. When ACA molecules were added without the enzyme-encapsulated nanoparticles, because no esterase was present in the system, no CFDA conversion was observed (Figure 5.5B, blue curve). This proves that ACA molecules do not interact with the CFDA molecules and do not facilitate the CFDA conversion. In another experiment, the acid-responsive imine bonds in the nanogate assembly were reduced to amine bonds, which disabled the acid-responsive feature.²³ When enzyme-encapsulated silica nanoparticles equipped with the amine version of nanogates were added into the CFDA solution, together with the addition of ACA, a negligible conversion rate was observed (Figure 5.5B, black curve). This was because the acid generated from the conversion of ACA could not activate the nanogate, therefore the access towards the enzyme for the CFDA molecules remained blocked. This result proves that the pH-responsiveness of the nanogate is indeed critical for the operation of this chemical amplifier, which further proves the mechanism of the amplifying process.

5.5 Summary

In summary, I have demonstrated the construction and the operation of a chemical amplifier based on enzyme-encapsulated silica nanoparticles equipped with pH-responsive nanogates. This work opens new realms in enzymatic catalysis, sensors and other biochemical applications.

5.6 Figures

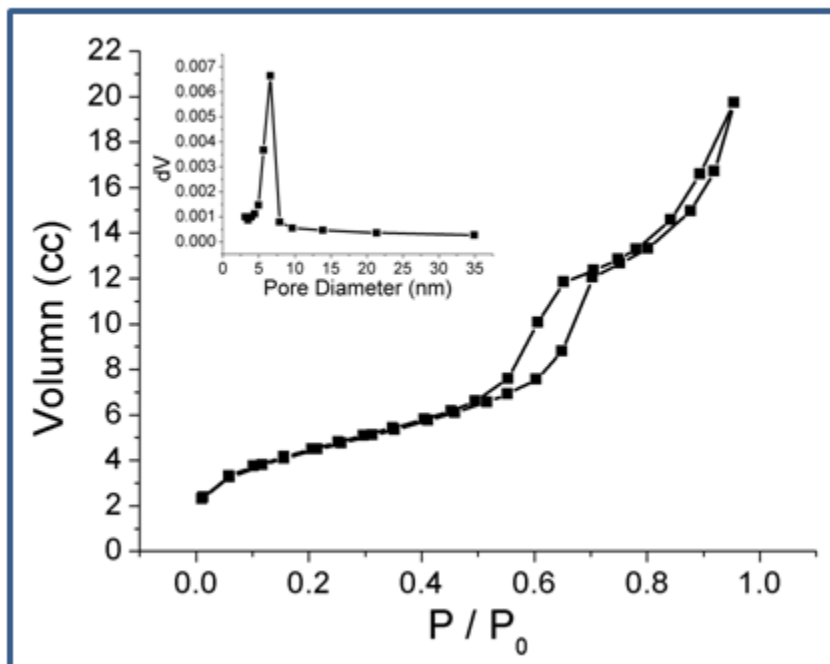


Figure 5.1. N₂ Adsorption isotherm and the pore size distribution of the extracted unmodified nanoparticles.

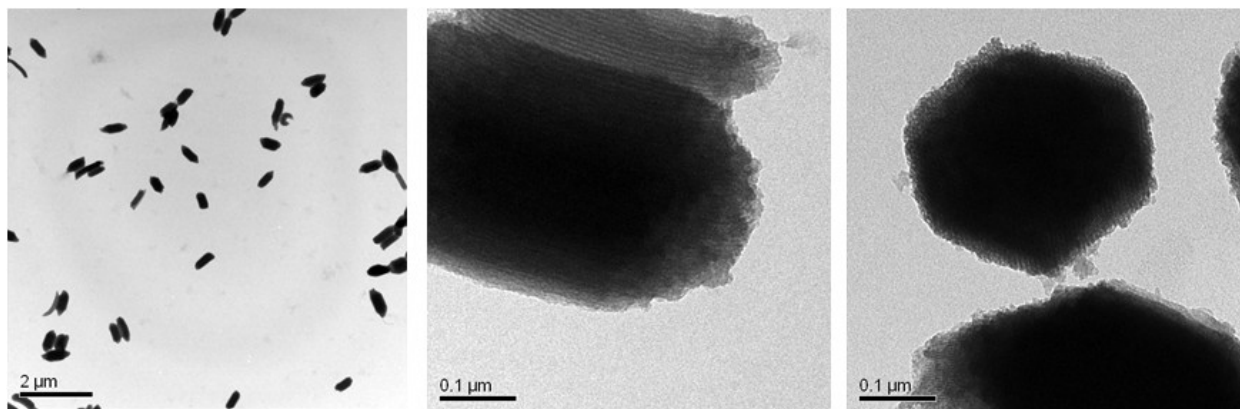


Figure 5.2. TEM images of the nanovalve-modified silica nanoparticle showing the overall size distribution around 300 nm by 500 nm (**Left**), the direction of the pore channels (**Middle**) and the pore openings (**Right**).

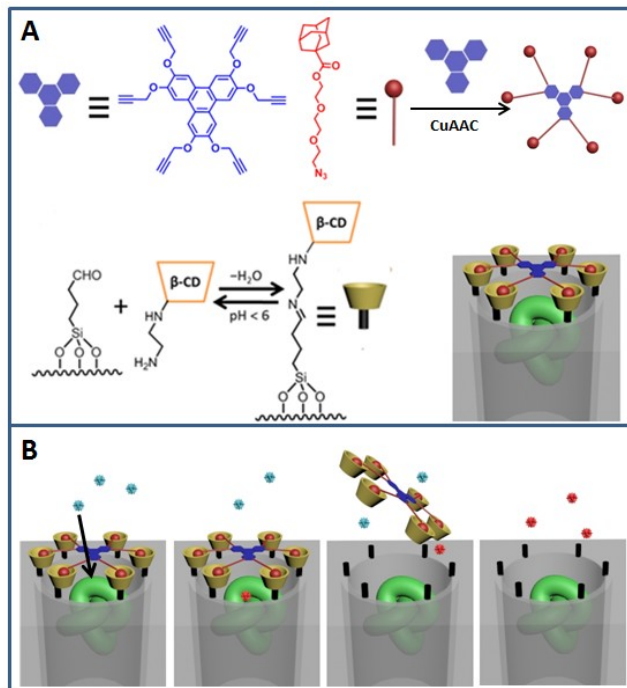


Figure 5.3. (A) Assembly of the nanogate. The capping agent is synthesized through a Cu catalyzed azid-alkyne coupling reaction. The green not represents the enzyme molecule that is trapped in the pore. **(B)** The mechanism of the self-amplifying process. A small substrate passes through the nanogate and is converted by the enzyme. The conversion generates acids and activates the nanogate, which allows more substrates to be converted at a higher rate.

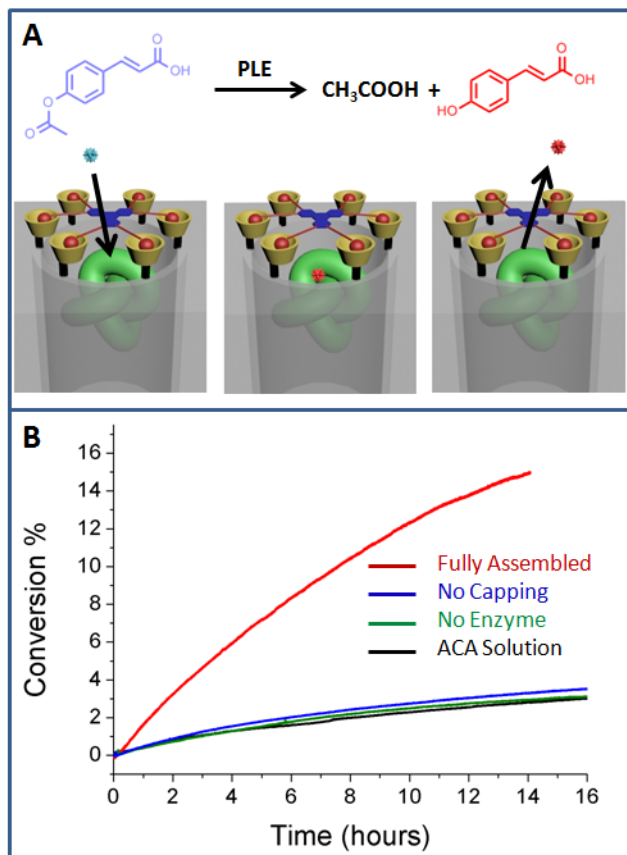


Figure 5.4. (A) Illustration of an ACA molecule passing through the nanogate and being converted by the enzyme. **(B)** Conversion profiles of the ACA solution with different samples: the fully assembled nanogate system with encapsulated enzymes, the no capping control, the no enzyme control, and the ACA solution by itself.

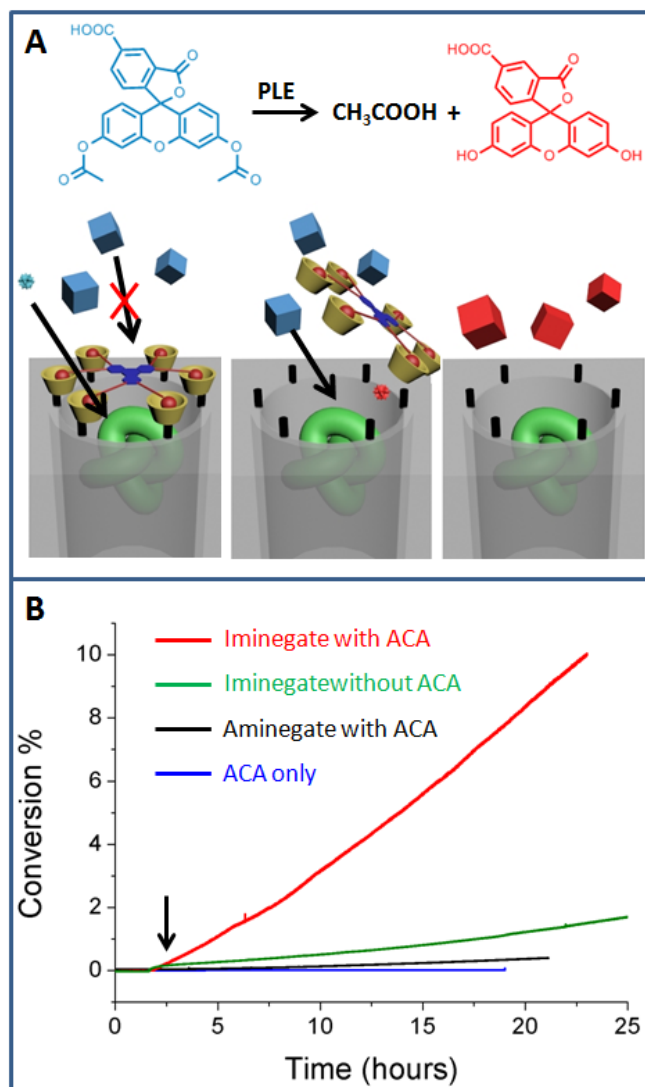


Figure 5.5. (A) Illustration of the operation of the enzyme-amplifier. The CFDA molecules are not able to be converted until ACA molecules pass through the nanogate and activate it. (B) Conversion profiles of the CFDA water solution with different samples added: the nanogate together with ACA solution; the nanogate alone; the amine-version of the nanogate with ACA solution; and ACA solution by itself. The black arrows indicate when nanoparticle samples were added into the solution.

5.7 References

1. M. F. Clark, A. N. Adams *J. Gen. Virol.*, **1977**, *34*, 475-483.
2. G. S. Wilson, Y. Hu *Chem. Rev.*, **2000**, *100*, 2693-2704.
3. G. Liu, Y. Wan, V. Gau, J. Zhang, L. Wang, S. Song, C. Fan *J. Am. Chem. Soc.*, **2008**, *130*, 6820-6825.
4. Y. Tan, R. M. Hoffman *Nature Protocols*, **2008**, *3*, 1388-1394.
5. K. Mannerstedt, A. M. Jansson, J. Weadge, O. Hindsgaul *Angew. Chem. Int. Ed.*, **2010**, *49*, 8173-8176.
6. O. R. Miranda, X. Li, L. Garcia-Gonzalez, Z.-J. Zhu, B. Yan, U. H. F. Uwe, V. M. Rotello *J. Am. Chem. Soc.*, **2011**, *133*, 9650-9653.
7. H. He, X. Xu, H. Wu, Y. Jin *Adv. Mater.*, **2012**, *24*, 1736-1740.
8. O. R. Miranda, H.-T. Chen, C.-C. You, D. E. Mortenson, X.-C. Yang, U. H. F. Bunz, V. M. Rotello *J. Am. Chem. Soc.*, **2010**, *132*, 5285-5289.
9. P. Wu, K. Hwang, T. Lan, Y. Lu *J. Am. Chem. Soc.*, **2013**, *135*, 5254-5457.
10. D. Lu, J. Cardiel, G. Cao, A. Q. Shen *Adv. Mater.*, **2010**, *22*, 2809-2813.
11. C. Mateo, V. Grazu, J. M. Palomo, F. Lopez-Gallego, R. Fernandez-Lafuente, J. M. Guisan *Nature Protocols*, **2007**, *2*, 1022-1033.
12. S. E. Letant, B. R. Hart, S. R. Kane, M. Z. Hadi, S. J. Shields, J. G. Reynolds *Adv. Mater.*, **2004**, *16*, 689-693.
13. H. Tang, F. Yan, P. Lin, J. Xu, H. L. W. Chan *Adv. Func. Mater.*, **2011**, *21*, 2264-2272.
14. M. Pita, M. Kramer, J. Zhou, A. Poghossian, M. J. Schoning, V. M. Fernandez, E. Katz *ACS Nano*, **2008**, *2*, 2160-2166.
15. D. Ivnitski, K. Artyushkova, R. A. Rincon, P. Atanassov, H. R. Luckarift, G. R. Johnson *Small*, **2008**, *4*, 357-364.

16. M. I. Kim, Y. Ye, B. Y. Won, S. Shin, J. Lee, H. G. Park *Adv. Func. Mater.*, **2011**, *21*, 2868-2875.
17. S. A. Yamanaka, B. Dunn, J. S. Valentine, J. I. Zink *J. Am. Chem. Soc.*, **1995**, *117*, 9095-9096.
18. A. K. Williams, J. T. Hupp *J. Am. Chem. Soc.*, **1998**, *120*, 4366-4371.
19. D. T. Nguyen, M. Smit, B. Dunn, J. I. Zink *Chem. Mater.*, **2002**, *14*, 4300-4306.
20. A. Wada, S. Tamaru, M. Ikeda, I. Hamachi *J. Am. Chem. Soc.*, **2009**, *131*, 5321-5330.
21. Y. Zhao, X. Sun, G. Zhang, B. G. Trewyn, I. I. Slowing, V. S.-Y. Lin *ACS Nano*, **2011**, *5*, 1366-1375.
22. M. Xue, D. Cao, J. F. Stoddart, J. I. Zink *Nanoscale*, **2012**, *4*, 7569-7574.
23. Y.-L. Zhao, Z. Li, S. Kabehie, Y. Y. Botros, J. F. Stoddart, J. I. Zink *J. Am. Chem. Soc.*, **2010**, *132*, 13016-13025.
24. W. Junge, K. Krisch *Eur. J. Biochem.*, **1974**, *43*, 379-389.
25. X. Wang, D. Lu, R. Austin, A. Agarwal, L. J. Mueller, Z. Liu, J. Wu, P. Feng *Langmuir*, **2007**, *23*, 5735-5739.
26. C. Wang, Z. Li, J. W. Gaines, Y.-L. Zhao, D. Cao, O. A. Bozdemir, M. W. Ambrogio, M. Frasconi, Y. Y. Botros, J. I. Zink, J. F. Stoddart *Angew. Chem. Int. Ed.*, **2012**, *51*, 5460-5465.

Chapter 6

Excited State Mixed Valence In A Binuclear Cu(I) Complex Analyzed

By A Neighboring Orbital Model

6.1 Abstract

Spectroscopic consequences of the excited state mixed valence (ESMV) in a binuclear copper complex are analyzed using the neighboring orbital model. This complex represents a new class of ESV system, where the coupling of two equivalent charge-bearing units is mediated through a copper-iodine bridged cluster. The coupling results in the break of degeneracy between the ligand orbitals and creates an energy gap of 1550 cm^{-1} . The result from the neighboring orbital model approach is supported by resonance Raman spectroscopic data and Gaussian molecular orbital calculations.

6.2 Introduction

Excited state mixed valence (ESMV) arises in molecules where two or more charge-bearing units are at equivalent sites.¹⁻⁵ At the ground state of the molecule, the charge distribution is totally symmetric, but in the excited state, the charge can localize on any of those equivalent units, which creates several possible asymmetric distributions. These distributions can be represented by a series of potential surfaces that are degenerate in energy along the displacement coordination. In certain cases, these potential surfaces can couple and generate new adiabatic surfaces, in which case the charge will be delocalized among those charge-bearing units, leading to some interesting spectroscopic consequences. For most of the ESVM compounds, the charge-bearing units (M) are coupled through a bridging unit (B) and the coupling can be analyzed through the neighboring orbital model (NOM).⁶ The basic NOM theory considers that the coupling among the charge-bearing units is mediated through mixing with orbitals on the bridge unit that exhibit appropriate energy and symmetry. In this work, I utilize this theory to analyze the electronic structure of a new type of ESVM compound, where the bridging unit consists of a highly coupled binuclear Cu_2I_2 unit.

The halogen bridged Cu_2X_2 unit has been a part of series of compounds where interesting photochemical properties have been studied.⁷⁻¹² Kern et al. reported the synthesis of several compounds, where two 1,2-bis(arylimino)acenaphthene (BIAN) ligands are connected through the Cu_2X_2 unit.¹³ These compounds are air-stable and display distinct metal-to-ligand or interligand charge-transfer bands in their absorption spectra. In the compound with Cu_2I_2 unit, the distance between the two copper ions falls into the range of cuprophilic interactions.⁸ This iodine-bridged compound is of particular interest in terms of ESVM analysis because the cuprophilic interaction leads to a highly delocalized charge distribution within the unit, which may enable the through-bond coupling of the two BIAN ligands. This compound can be described as a ligand-bridge-ligand (L-B-L) type molecule (Figure 6.1). At the excited state of

this compound, the negative charge can localize on either the left or the right side of the molecule, and though a possible through-bond coupling mediated by the delocalized orbital on the Cu_2I_2 bridge unit, the charge can be completely delocalized through the molecule. In this chapter, I analyze the ESMV feature of this compound by using the NOM theory. The analysis is compared with Gaussian calculation and it correlates well with the experimental data from electronic and vibrational spectroscopy.

6.3 Experimental

Synthesis and characterization

The compound **2** was synthesized according to literature (Figure 6.1).¹³ The absorption spectrum of **2** was obtained at 77 K using a Cary 5000 UV-vis-NIR spectrophotometer.

Resonance Raman spectroscopy

Resonance Raman spectra of **2** were obtained using a Jobin-Yvon HR 320/640 triple monochromator equipped with a CCD detector (Princeton Instruments Spec 10-400). The sample was excited by a Coherent Innova 90C argon ion laser (for wavelengths of 514.5, 501.7, 496.5, 488.0, 476.5, 472.6, 465.8 and 457.9 nm) or a Coherent Innova 300C krypton ion laser (for wavelengths of 676.4, 647.1 and 568.2 nm). Spectra were collected from spinning pellets of **2** with KPF_6 used as an internal standard. The intensity of each peak in the Raman spectrum was numerically integrated and averaged over multiple spectra collected with the same excitation wavelength. The integrated intensity of each peak was normalized to the intensity of the 750 cm^{-1} peak of the KPF_6 standard. Excitation profiles were calculated using the intensities of the identified vibrational modes.¹⁴⁻¹⁹

DFT calculation

Density functional theory (DFT) calculations were carried out using the Gaussian 03 suite of programs.²⁰ The B3LYP functional was employed in the calculation. The 6-31G basis set was used for calculating compound **1** and the *lanl2dz* basis set was used for compound **2**.

6.4 Results

6.4.1. Absorption spectra

The absorption spectrum of compound **2** in vis-NIR region is shown in Figure 6.2. The major peak in the spectrum represents the charge transfer band, and was previously assigned to a metal-to-ligand charge transfer.¹³ This band has a maximum at 17044 cm^{-1} , with three shoulders approximately at 18799, 15174 and 13602 cm^{-1} . The band can be deconvoluted into five Gaussian peaks with their maxima at 13719, 15269, 17094, 19174 and 20724 cm^{-1} respectively.

6.4.2. Gaussian calculation

The calculated frontier orbitals (HOMO-1 to LUMO+3) are displayed in Figure 6.3. The highest energy occupied orbitals have major components located on the Cu_2I_2 unit while the lowest energy unoccupied orbitals exhibit major components on the BIAN ligand. In the case of HOMO-1 orbital, there are contributions from the π orbitals on the $\text{N}=\text{C}-\text{C}=\text{N}$ units of the ligands. Similarly, LUMO+1 displays rather small components on the Cu_2I_2 unit.

6.4.3. Resonance Raman spectra

The vibrational modes are identified with the assistance of the Gaussian calculation (Table 6.1). The resonance Raman intensities of peaks corresponding to these modes are normalized to that of the 750 cm^{-1} peak from the KPF_6 standard, and these normalized intensities are plotted against excitation wavelengths to generate resonance Raman profiles.

The relative distortion is calculated according to the excitation wavelength. Figure 6.4 displays resonance Raman profiles of several important vibrational modes.

6.5 Discussion

6.5.1 Neighboring orbital model (NOM)

Basic theory of NOM

The compound **2** represents an L-B-L (Ligand-Bridge-Ligand) type molecule. In a simple NOM picture, the possible through-bond coupling of the two ligand π systems is mediated by the bridge unit, and the coupling occurs when the ligand π molecular orbitals mix with the appropriate neighboring orbitals on the bridge unit. In principle, those orbitals that are the closest in energy will result in the greatest mixing and contribute the most to the coupling. As shown in Figure 6.5, before the effective coupling occurs, those orbitals on the two ligand systems exhibit negligible direct overlap, and they can be represented either by the orbital localized on the left or the right ligand, or by the linear combinations between those two. The in-phase $\pi_a + \pi_b$ or out-of-phase $\pi_a - \pi_b$ linear combinations are degenerate in energy in the absence of coupling. When an orbital from the bridge unit, which has an appropriate symmetry and energy, mixes with one or both of those linear combinations, the energy degeneracy will be removed.

Analysis of the ligand orbitals

The orbitals participating in the effective mixing should have similar energy levels. Since the ligand acts as an electron acceptor in the charge transfer process addressed in this chapter, it is reasonable to focus our analysis on the empty π^* orbitals closest to the LUMO on the ligand. With the results from Gaussian calculation, I choose the LUMO (π_1) and LUMO+1 (π_2) as our

ligand orbitals in NOM. The linear combination of the orbitals from the left and right ligands results in degenerate orbitals with different symmetries. (Figure 6.6)

Analysis of the bridging unit orbitals

In this chapter, I choose the Cu_2I_2 core as the bridge unit in its entirety, because: 1) previous studies have proved that there are strong interactions between those two copper atoms,¹³ which make it reasonable to include both of them in the assessment of the coupling; 2) the Gaussian calculation of compound **2** suggests that the highest energy occupied orbitals consist of components located on both copper and iodine atoms (Figure 6.3).

In order to generate those orbitals that can participate in the coupling, the copper 3d orbitals and the iodine 5p orbitals are mixed based on symmetry within the D_{2h} point group. Orbitals from the two copper atoms are first transformed into their linear combinations, whose symmetries are assigned in the D_{2h} point group. (Figure 6.7) The same procedure is then performed on those iodine atoms to generate six linear combinations of 5p orbitals with different symmetries. (Figure 6.8) The two sets of linear combinations are then mixed based on symmetry to generate the expected molecular orbitals of the Cu_2I_2 unit. (Figure 6.9) With the aid of the Gaussian calculation, the relative energy of these orbitals can be estimated. (Figure 6.10) Because of the energy matching principle of NOM, only those filled orbitals with the highest energy levels on the Cu_2I_2 unit will participate in the coupling process. Figure 6.11 shows the schematic representations of those orbitals.

6.5.2 ESMV in compound 2

ESMV analyzed by NOM

For the CuI -BIAN compound, the lowest energy excited states involve ligand π^* orbitals that are interchangeably equivalent. In a diabatic basis, these orbitals are degenerate in energy,

and can be described as either a localized orbital on one of the ligand, or the linear combination between them. In an adiabatic picture, the orbitals on different ligands couple through the bridge unit and the degeneracy is thus removed. This requires the empty π^* orbitals from the ligands and the occupied orbitals from the Cu_2I_2 unit to mix based on symmetry and energy levels. Orbitals that fulfill these criteria are the in-phase $\pi_{1a}+\pi_{1b}$ orbital from the ligand, and a b_{1u} orbital on the Cu_2I_2 unit that arises from the out-of-phase mixing of $d_{yz}+d_{yz}'$ and p_z-p_z' orbitals on copper and iodine atoms respectively. The coupling removes the degeneracy of the $\pi_{1a}+\pi_{1b}$ and the $\pi_{1a}-\pi_{1b}$ orbitals, causing an energy separation between them. Figure 6.12 illustrates the orbital origin and the consequence of the coupling. Because the lower energy orbital arises from the out-of-phase combination of the ligand orbitals, the sign of the coupling can be determined to be positive.

Assignment of Peaks in Electronic Spectra

The deconvoluted peaks in the electronic spectrum of compound **2** (Figure 6.2) can be assigned based on the coupling described above. Figure 6.13 shows the relative energy levels of the molecular orbitals, and the transitions corresponding to different peaks in the charge transfer band. The two peaks with the lowest energy (peak 1 and 2) can be assigned as the transition from HOMO to LUMO and LUMO+1 respectively. The intensities of these two peaks correlate with the transition selection rules, and the energy difference between them reflects the energy separation of the orbitals as a consequence of the coupling. Peak 3 can be assigned as either the transition from HOMO to LUMO+2, or from HOMO-1 to LUMO. With the assistance from the resonance Raman profiles, it can be assigned as the HOMO to LUMO+2 transition, that will be discussed later in section 4.3. The two peaks with the highest energy are thus assigned as the HOMO-1 to LUMO and LUMO+1 transitions respectively. The energy difference between these two peaks (1550 cm^{-1}) is the same as that between peak 1 and 2, which is consistent with the coupling model.

6.5.3 Resonance Raman Analysis

The resonance Raman profile reveals the correlation between a vibrational mode and an electronic transition. As discussed before, peak 1 and 2 in the absorption spectrum correspond to the transitions from HOMO to LUMO and LUMO+1. When an electron is promoted from HOMO to LUMO or LUMO+1, the effective N=C bonding will be weakened due to the anti-bonding nature between the nitrogen and carbon atoms in LUMO and LUMO+1 (Figure 3). Consequently, any vibrational mode involving the motion of this bond will be enhanced when it is in resonance with peak 1 and 2. The enhancement of modes 473 cm^{-1} (Cu-N=C wagging in plane) and 1222 cm^{-1} (N=C-C=N unit stretching) in their resonance Raman profiles can be therefore explained (Figure 6.4). Additionally, the maxima at peak 2 for modes involving Cu-N stretching (838 cm^{-1} and 1222 cm^{-1}) can be further explained by the weak anti-bonding nature of the N-Cu bond in LUMO+1. The resonance Raman profiles of other vibrational modes can be correlated similarly according to the analysis.

Another useful application of resonance Raman profiles is to assist the assignment of electronic transitions. As discussed in section 4.2, the peak 3 in the absorption spectrum can be assigned to either HOMO \rightarrow LUMO+2, or HOMO-1 \rightarrow LUMO. From the Gaussian calculation (Figure 6.3 and Figure 6.6), it is obvious that LUMO has its major components located at the N=C-C=N unit of the ligand, while LUMO+2 exhibit major components on the ligands' aromatic ring systems. As shown in Figure 6.4, modes 1575 cm^{-1} and 1610 cm^{-1} exhibit their maxima at peak 3, and both of them are correlated to the motion of the aromatic ring unit on the ligand. Therefore, it is reasonable to conclude that LUMO+2 should be involved in the corresponding transition, and peak 3 is thus assigned as HOMO \rightarrow LUMO+2. This assignment is also consistent with the assignments for other peaks.

6.6 Summary

The $\text{Cu}_2(\mu\text{-I})_2(1,2\text{-bis}(\text{benzylimino})\text{acenaphthene})_2$ complex represents a ligand-bridge-ligand type compound, where the two BIAN ligands are interchangeably equivalent to each other. When the complex is excited, charge transfer from the Cu_2I_2 unit to the BIAN ligands occurs. According to the analysis using a neighboring orbital model, the two degenerate ligand orbital linear combinations can couple through mixing with a neighboring orbital located on the Cu_2I_2 bridge unit. The coupling results in the breaking of degeneracy between those two ligand orbitals and creates an energy gap of 1550 cm^{-1} . The frontier orbitals of this compound generated from the neighboring orbital analysis correlate well with the experimental results from absorption and vibrational spectroscopy.

6.7 Tables and Figures

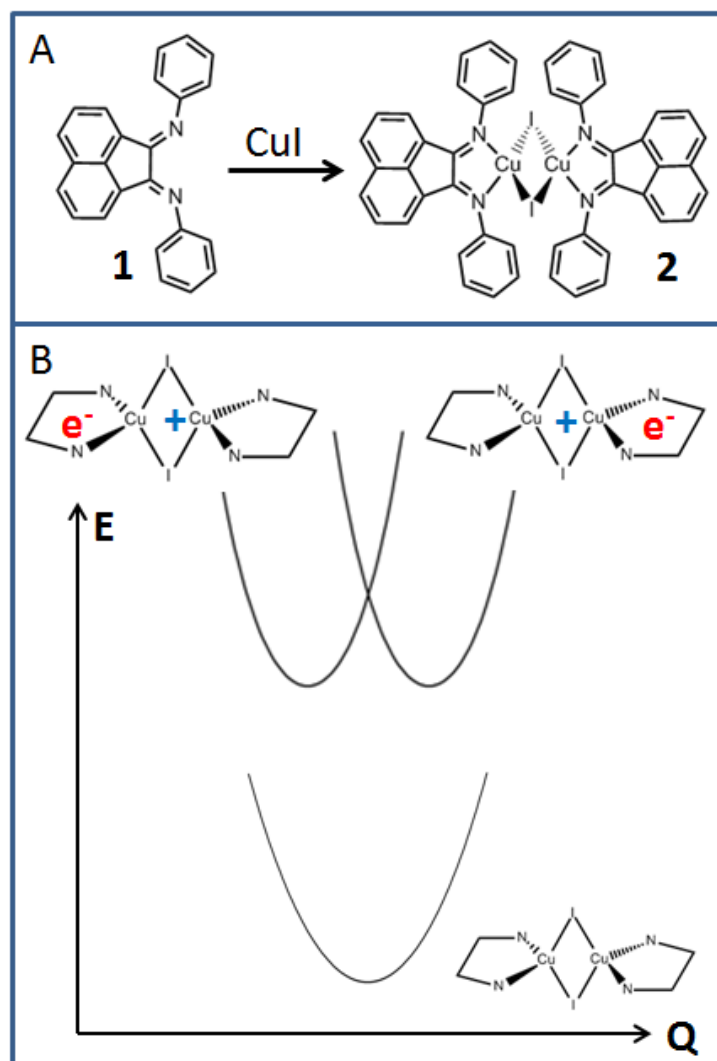


Figure 6.1. (A) Scheme for the synthesis of the binuclear Cu(I) compound **2**. (B) The potential surface diagram denoting the two possible charge distributions at the excited state.

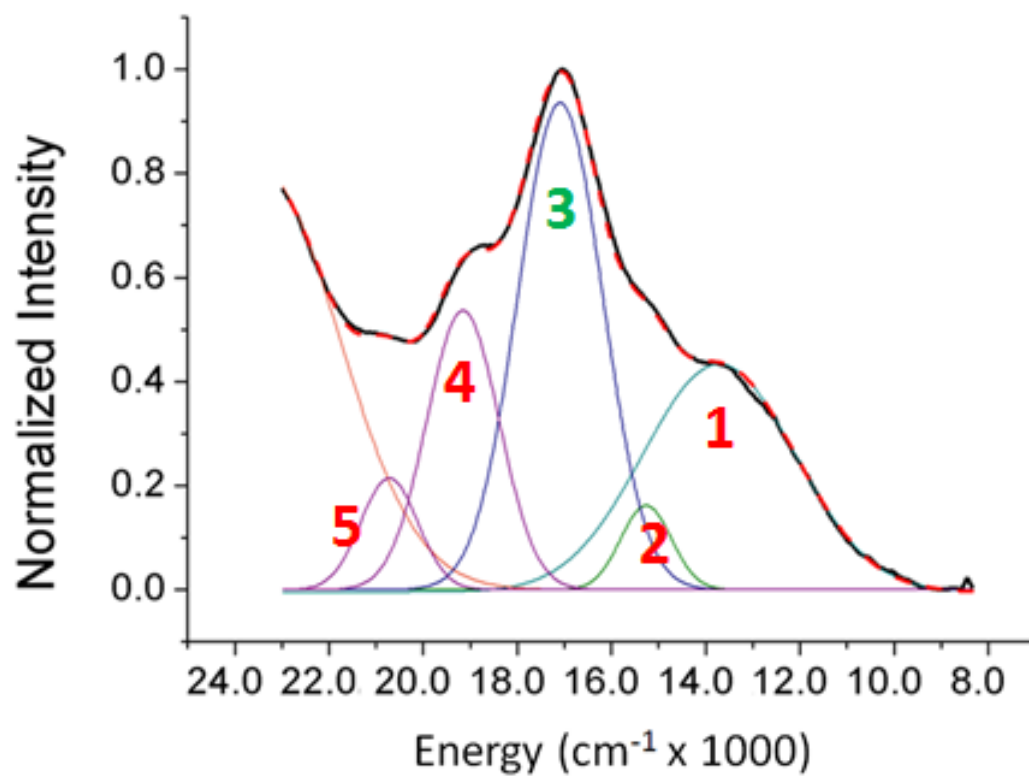


Figure 6.2. The absorption spectrum of compound **2** in vis-NIR region in which the charge transfer band arises. The deconvoluted peaks are marked with numbers and the sum of these peaks is plotted as the red dash line.

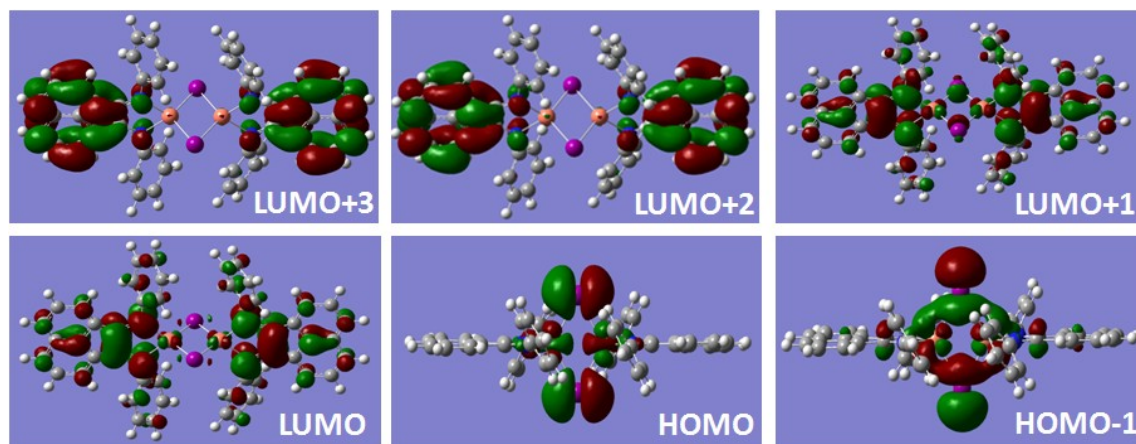


Figure 6.3. Selected molecular orbital contours of compound 2.

Table 6.1. Observed Resonance Raman Frequencies and Assignments.

ω^b	ω^c	assignment
195	181	Cu-Cu stretching
523	473	Cu-N=C wagging in plane with ligand ring rocking
530	512	Cu-N stretching with ligand ring wagging
619	598	Cu-N stretching with ligand ring breathing
838	838	Cu-N stretching with ligand ring breathing
1135	1115	C-C in the N=C-C=N unit stretching with ligand C-H wagging in plane
1251	1222	C-C in the N=C-C=N unit stretching with N-Cu-N wagging in plane
1482	1451	Ligand ring wagging
1609	1575	Ligand ring stretching
1646	1610	Ligand ring stretching

^aAll frequencies are given in cm^{-1} . ^bGaussian calculated frequency. ^cObserved frequency

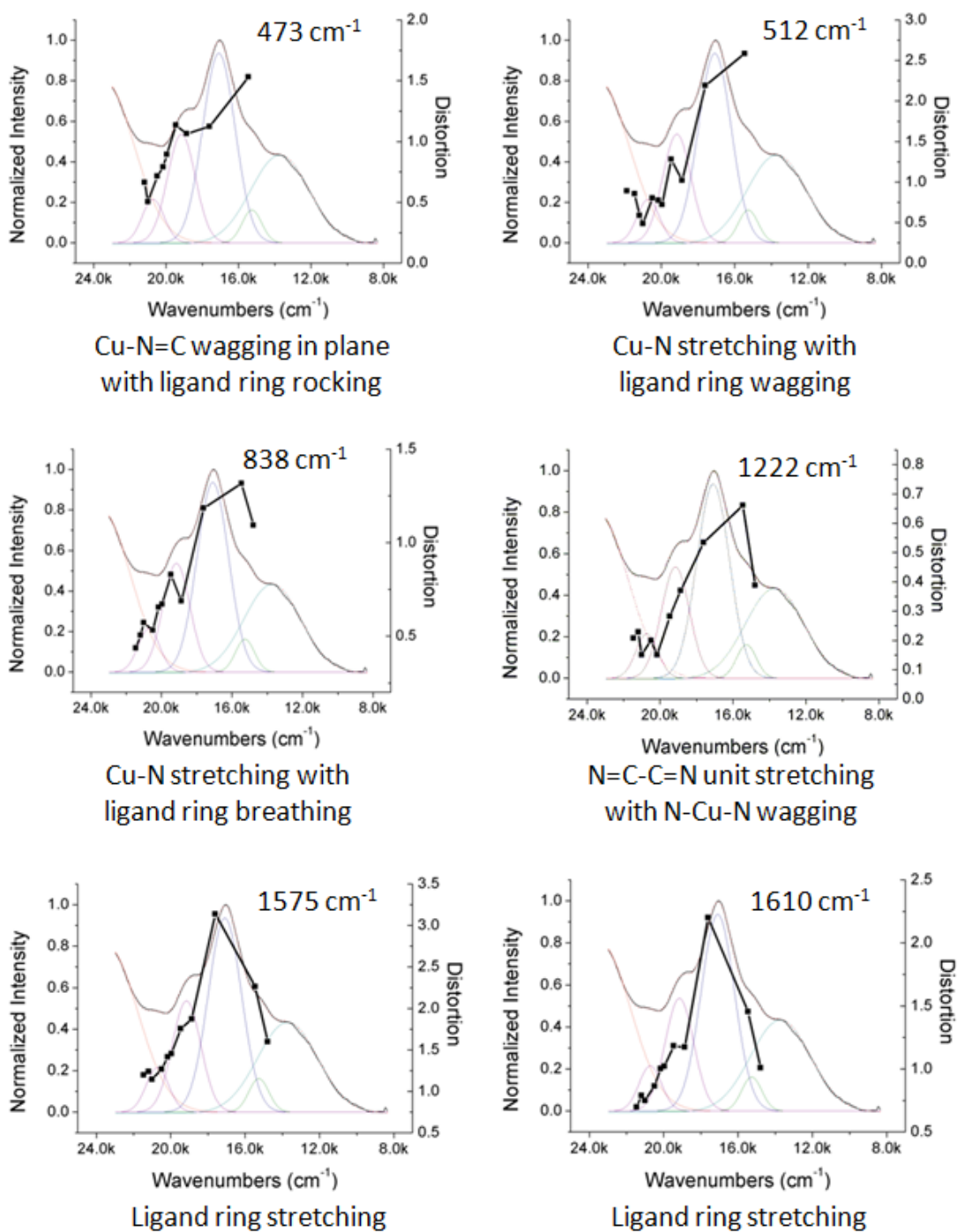


Figure 6.4. Resonance Raman profiles of selected vibrational modes. The normalized intensities of each mode (black line with dots) are plotted against the excitation wavelength. The background shows the absorption spectrum of compound **2** and its deconvoluted peaks.

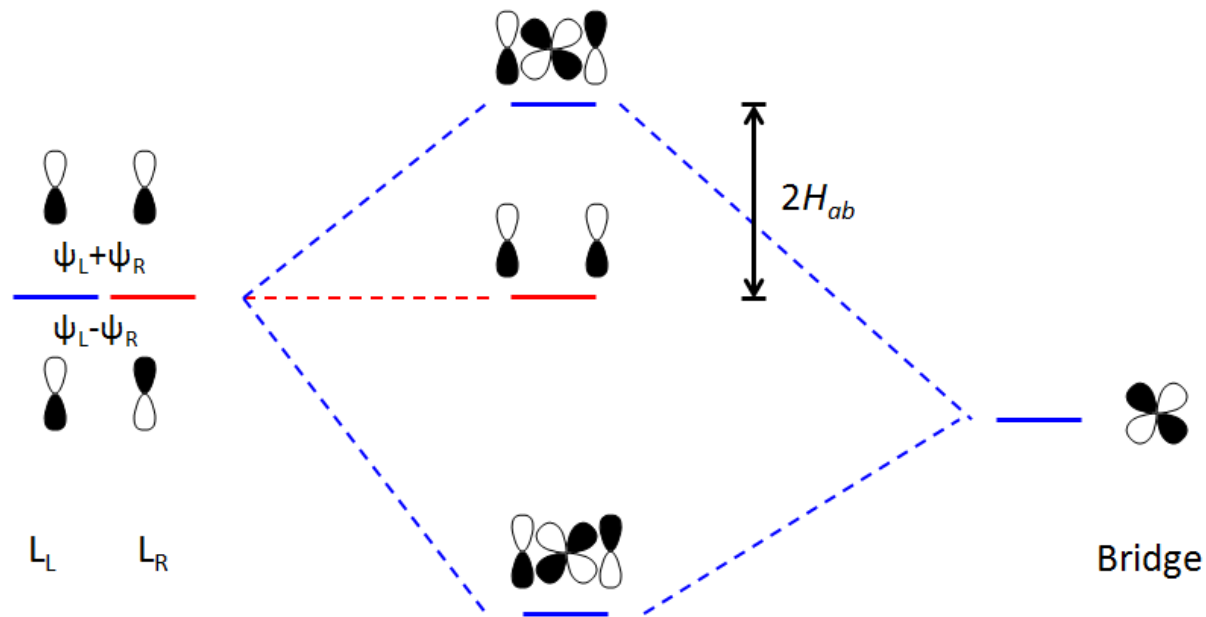


Figure 6.5. An example of NOM. The linear combinations of the orbitals from the left and the right ligands are degenerate in energy. When an orbital on the bridge unit possess appropriate energy level as well as symmetry, it can mix with one of those linear combinations and create energy separation between them. In a simplified picture, the energy separation equals to twice of the off-diagonal coupling term.

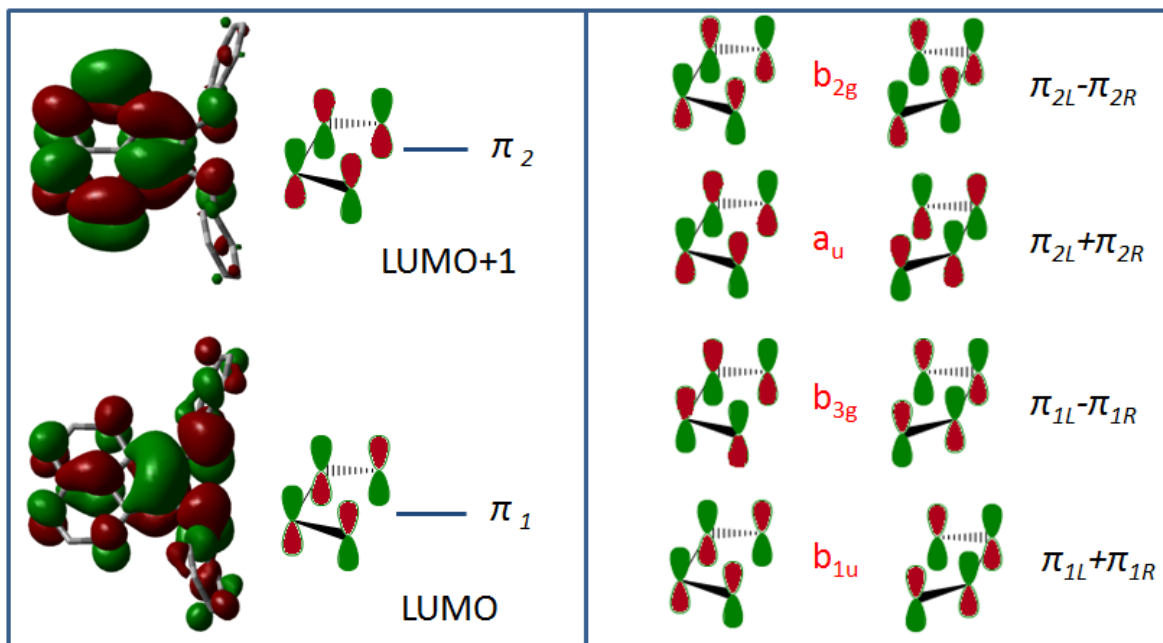


Figure 6.6. (Left) Contours of the two lowest unoccupied molecular orbitals of compound **1**. The orbitals are denoted as π_1 and π_2 respectively, and they are hereafter represented by simplified schemes emphasizing the phase and symmetry of the N=C-C=N subunit. **(Right)** The linear combinations of the ligand orbitals. Symmetries are assigned in D_{2h} point group.

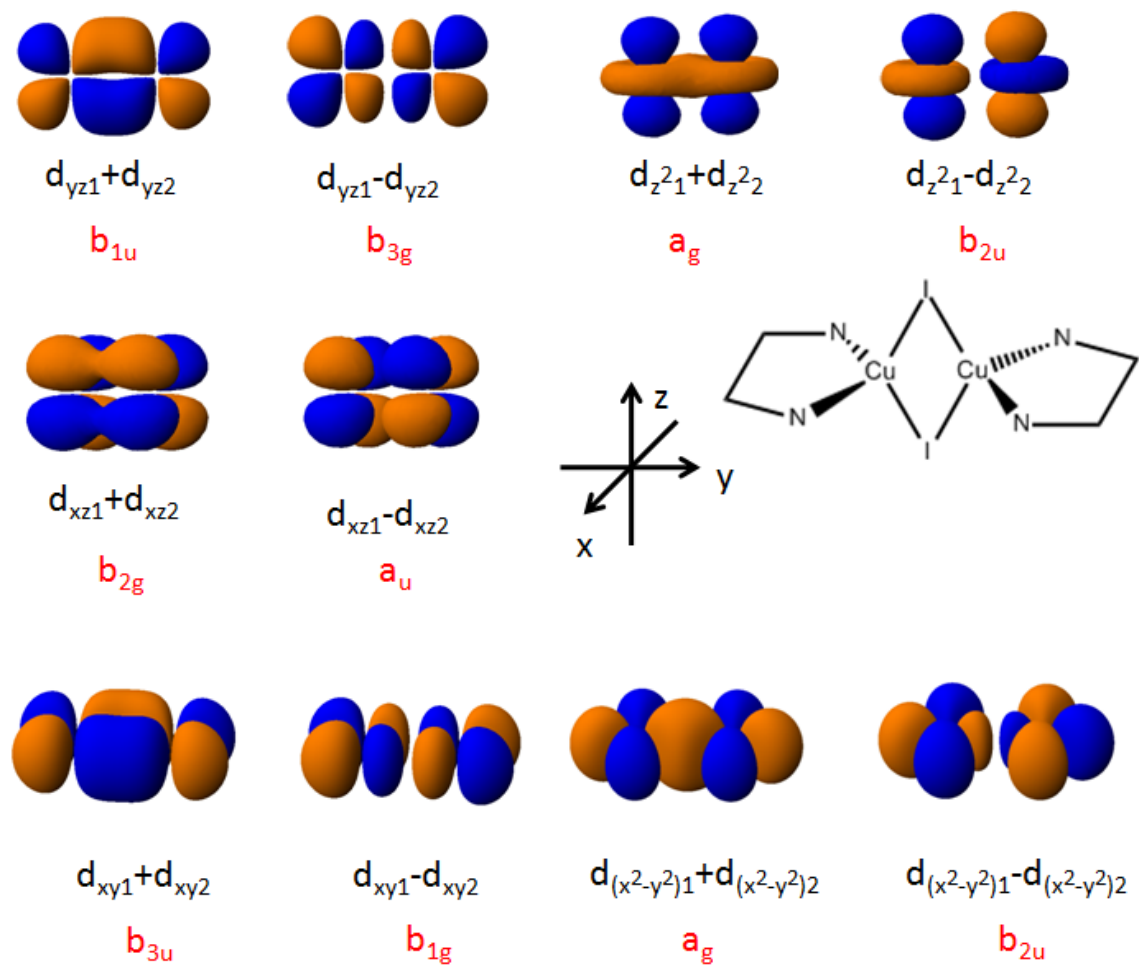


Figure 6.7. Orbital combinations on Cu atoms of the Cu_2I_2 bridge unit generated from symmetry adaption.

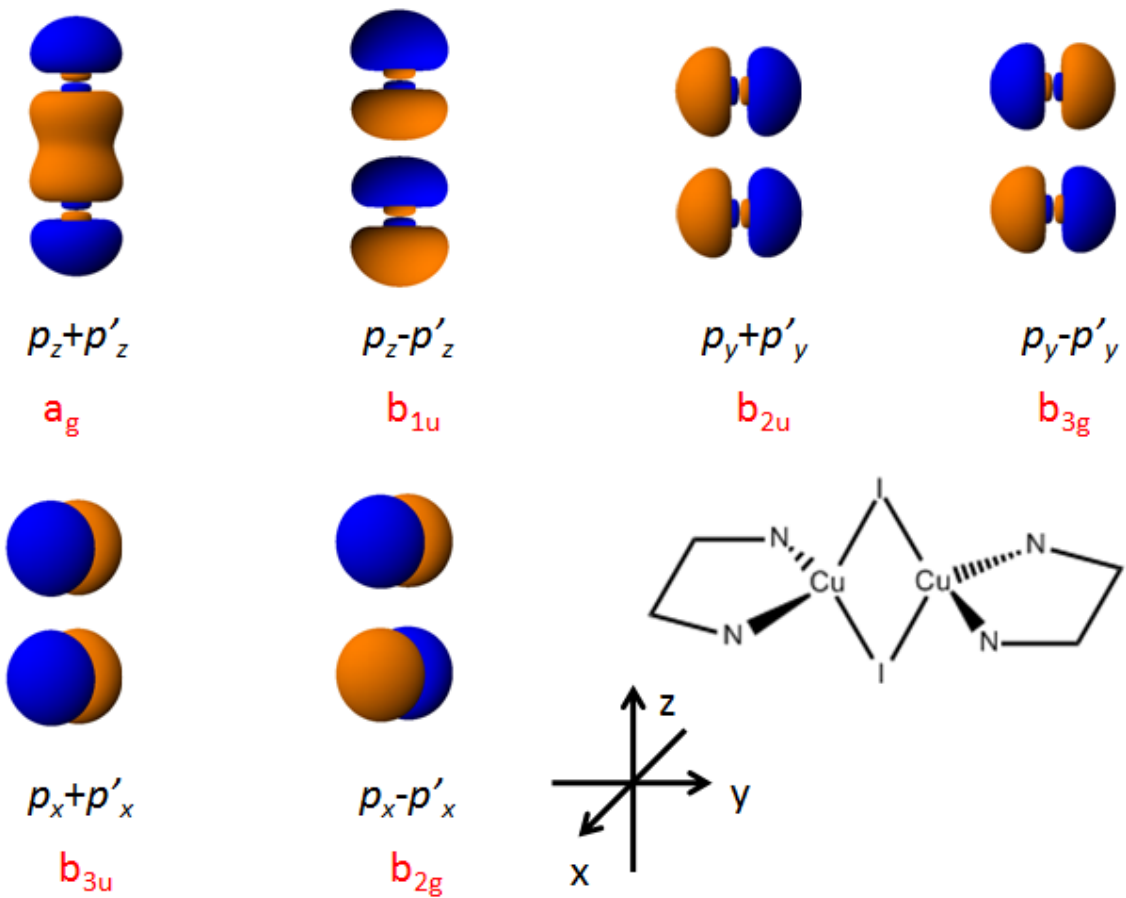


Figure 6.8. Orbital combinations on iodine atoms of the Cu_2I_2 bridge unit generated from symmetry adaption.

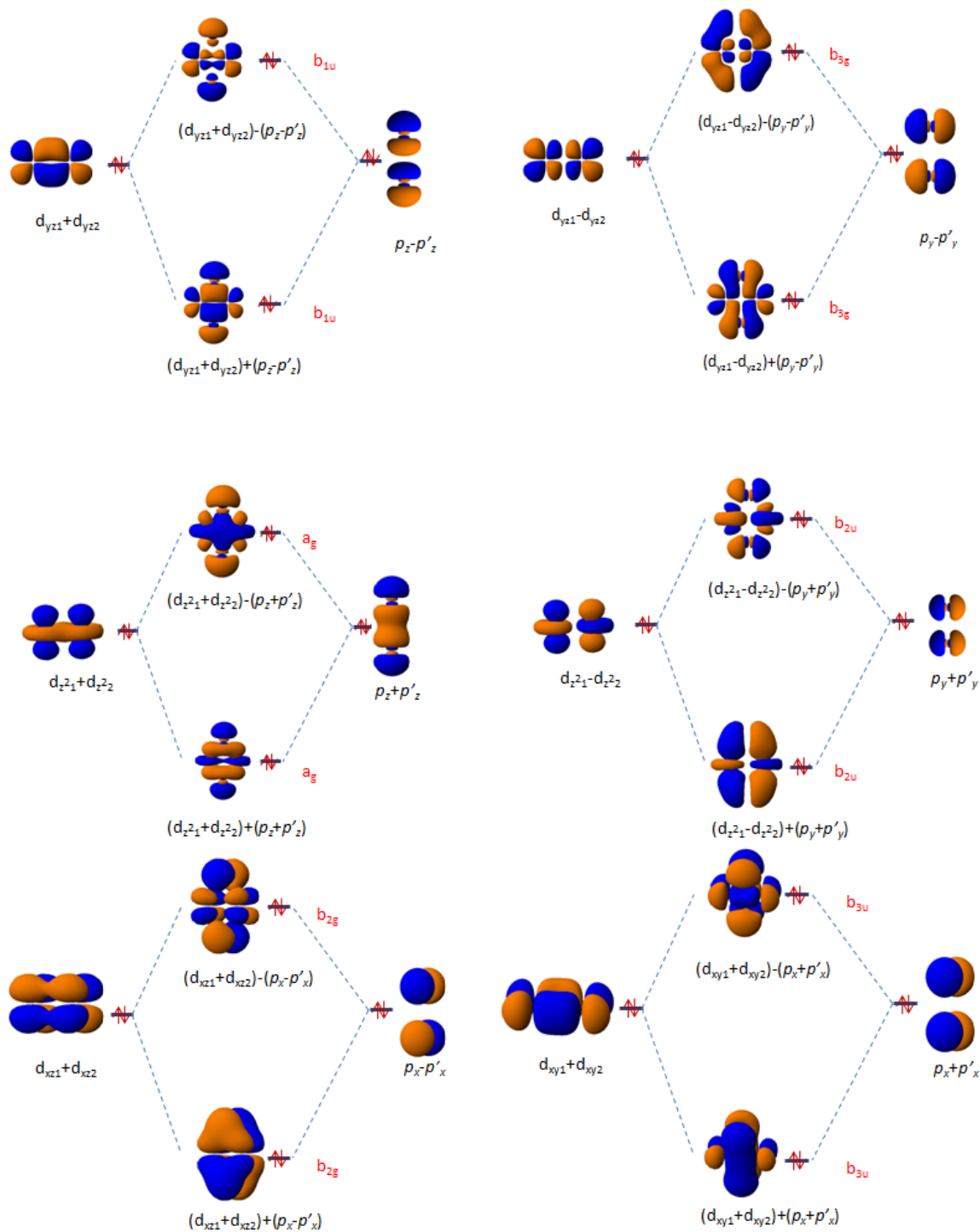


Figure 6.9. Orbital combinations between copper and iodine atoms of the Cu_2I_2 bridge unit generated from symmetry adaption.

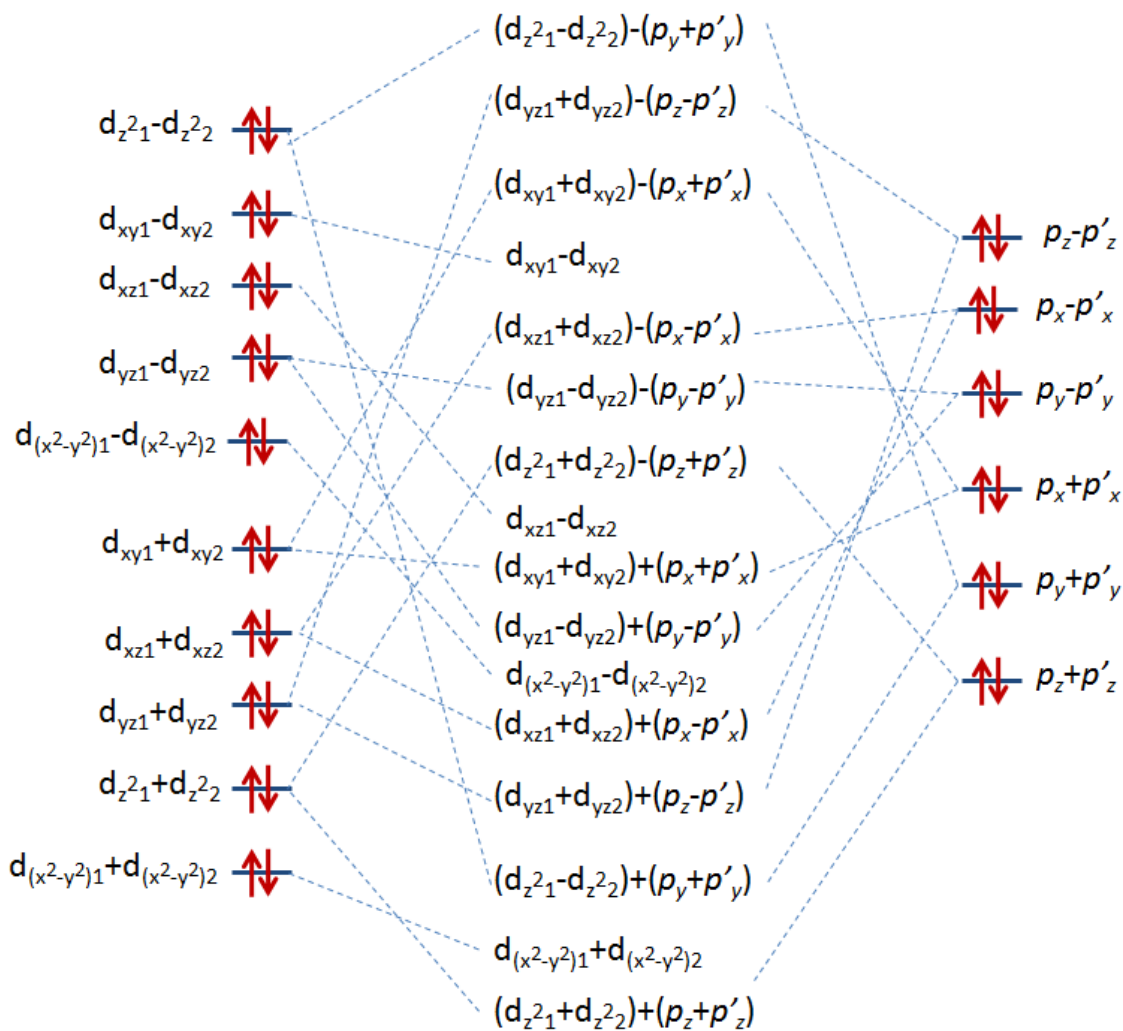


Figure 6.10. Energy diagram of the combined orbitals. Relative energy order is determined from the Gaussian molecular orbital calculation

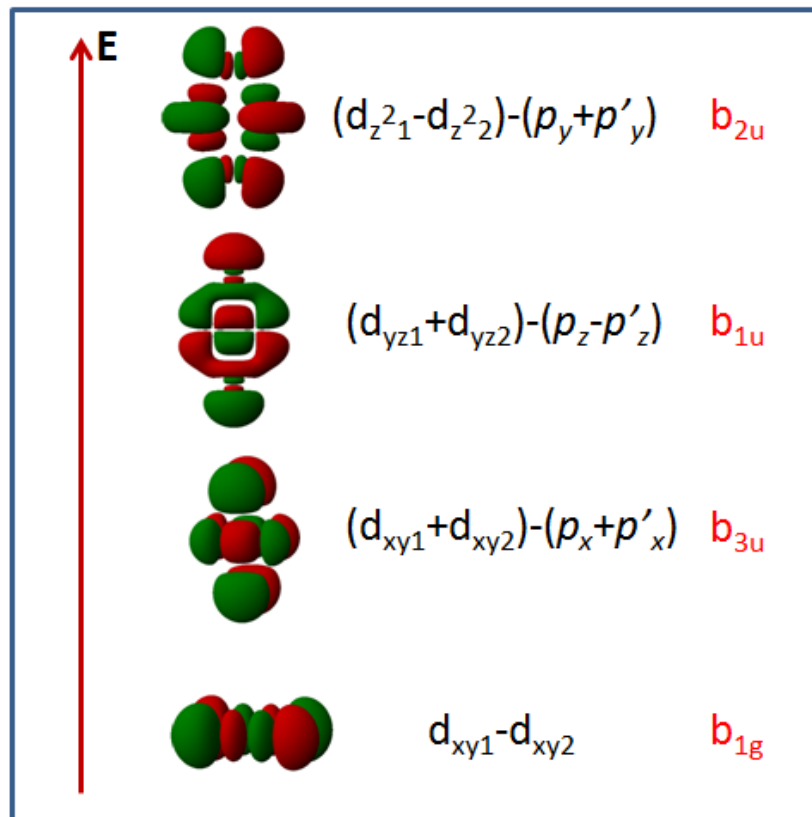


Figure 6.11. Schematic representations of the orbitals resulting from the symmetry adaption with the highest energy levels on the Cu_2I_2 unit. The coefficient of each orbital is not normalized and only represents the phase difference.

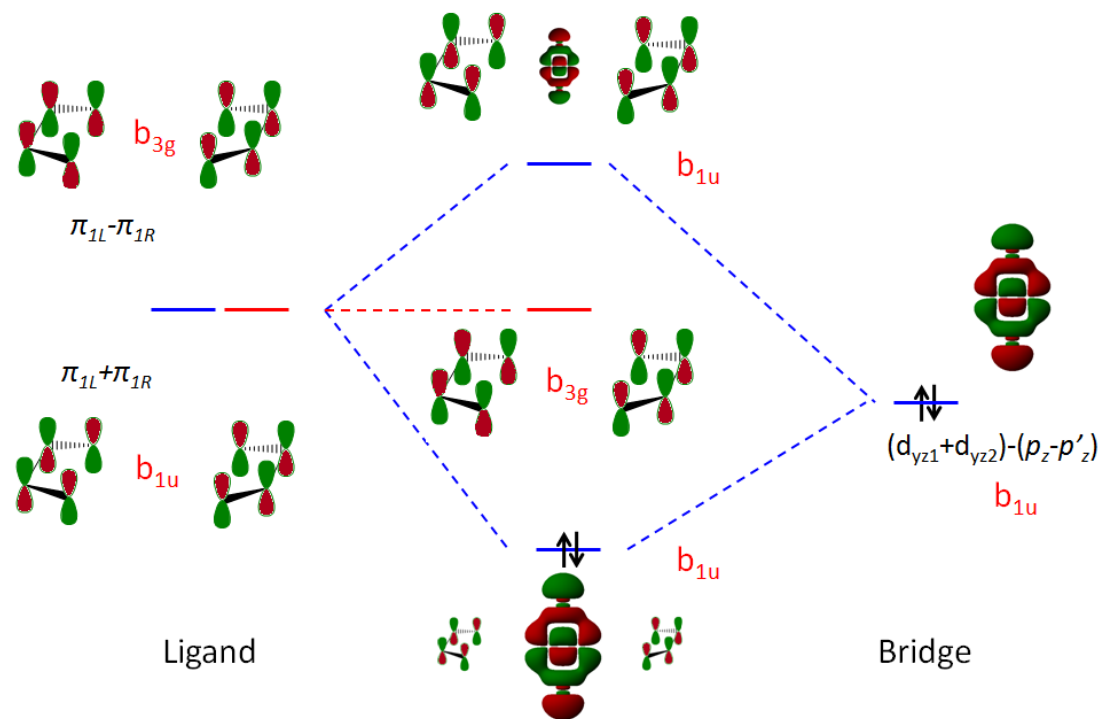


Figure 6.12. Schematic description of the coupling between the two ligand orbitals through the mixing with a b_{1u} orbital located on the Cu_2I_2 bridge unit. The result is from the analysis through the NOM.

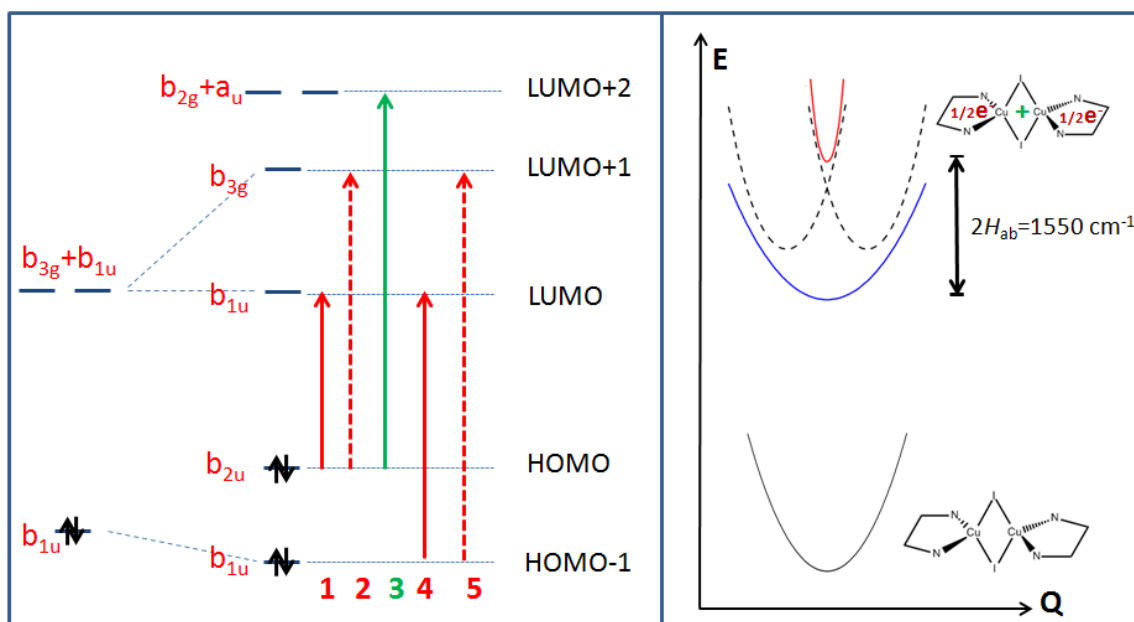


Figure 6.13. (Left) Orbitals contributing to the rise of ESMV before coupling, the frontier orbitals of compound **2** after orbital coupling, and the assignment of transitions corresponding to peaks in the absorption spectrum. The transitions 1, 2, 4 and 5 are related to the ESMV analysis and are denoted by red arrows, while transition 3 is out of the picture of the ESMV analysis in this chapter and is denoted by a green arrow. The allowed transitions are represented by solid arrows and the forbidden ones are denoted by dashed arrows. **(Right)** The potential surface diagram of compound **2** describing the coupled excited state. The dashed lines represent the diabatic excited state potential surface, while the blue and red lines show the coupled surfaces in the adiabatic basis. The energy separation between these coupled surfaces equals to the energy gap between the LUMO and LUMO+1 of compound **2**, and it is twice of the numeric value of the coupling term between these two.

6.8 References

1. Lockard, J. V.; Zink, J. I.; Konradsson, A. E.; Weaver, M. N.; Nelsen, S. F. *J. Am. Chem. Soc.* **2003**, *125*, 13471-13480.
2. Lockard, J. V.; Zink, J. I.; Trieber, D. A.; Konradsson, A. E.; Weaver, M. N.; Nelsen, S. F. *J. Phys. Chem. A* **2005**, *109*, 1205-1215.
3. Nelsen, S. F.; Konradsson, A. E.; Weaver, M. N.; Guzei, I. A.; Goebel, M.; Wortmann, R.; Lockard, J. V.; Zink, J. I. *J. Phys. Chem. A* **2005**, *109*, 10854-10861.
4. Plummer, E. A.; Zink, J. I. *Inorg. Chem.* **2006**, *45*, 6556-6558.
5. Hoekstra, R. M.; Dibrell, M. M.; Weaver, M. N.; Nelsen, S. F.; Zink, J. I. *J. Phys. Chem. A* **2009**, *113*, 456-463.
6. Nelsen, S. F.; Weaver, M. N.; Luo, Y.; Lockard, J. V.; Zink, J. I. *Chem. Phys.* **2006**, *324*, 195-201.
7. Ford, P. C.; Cariati, E.; Bourassa, J. *Chem. Rev.* **1999**, *99*, 3625-3647.
8. Kyle, K. R.; Ryu, C. K.; Ford, P. C.; DiBenedetto, J. A. *J. Am. Chem. Soc.* **1991**, *113*, 2954-2965.
9. Rath, N. P.; Holt, E. M.; Tanimura, K. *J. Chem. Soc., Dalton Trans.* **1986**, 2303-2310.
10. Li, R.-Z.; Li, D.; Huang, X.-C.; Qi, Z.-Y.; Chen, X.-M. *Inorg. Chem. Commun.* **2003**, 1017-1019.
11. Henary, M.; Wootton, J. L.; Khan, S. I.; Zink, J. I. *Inorg. Chem.* **1997**, *36*, 796-801.
12. Araki, H.; Tsuge, K.; Sasaki, Y.; Ishizaka, S.; Kitamura, N. *Inorg. Chem.* **2005**, *44*, 9667-9675.
13. Kern, T.; Monkowius, U.; Zabel, M.; Knör, G. *Inorg. Chim. Acta* **2011**, *374*, 632-636.
14. Henary, M.; Zink, J. I. *J. Am. Chem. Soc.* **1989**, *111*, 7407-7411.
15. Heller, E. J.; Sundberg, R. L.; Tannor, D. *J. Phys. Chem.* **1982**, *86*, 1822-1833.

16. Zink, J. I.; Shin, K.-S. K. *Advances in Photochemistry*; Wiley: New York, 1991; Vol. 16, pp 119-214.
17. Shin, K.-S. K.; Zink, J. I. *Inorg. Chem.* **1989**, *28*, 4358-4366.
18. Shin, K.-S. K.; Zink, J. I. *J. Am. Chem. Soc.* **1990**, *112*, 7148-7157.
19. Hanna, S. D.; Zink, J. I. *Inorg. Chem.* **1996**, *35*, 297-302.
20. Frisch, M. J.; Trucks, G. W.; Schlegel, H. B.; Scuseria, G. E.; Robb, M. A.; Cheeseman, J. R.; Montgomery, J. A., Jr.; Vreven, T.; Kudin, K. N.; Burant, J. C.; Millam, J. M.; Iyengar, S. S.; Tomasi, J.; Barone, V.; Mennucci, B.; Cossi, M.; Scalmani, G.; Rega, N.; Petersson, G. A.; Nakatsuji, H.; Hada, M.; Ehara, M.; Toyota, K.; Fukuda, R.; Hasegawa, J.; Ishida, M.; Nakajima, T.; Honda, Y.; Kitao, O.; Nakai, H.; Klene, M.; Li, X.; Knox, J. E.; Hratchian, H. P.; Cross, J. B.; Bakken, V.; Adamo, C.; Jaramillo, J.; Gomperts, R.; Stratmann, R. E.; Yazyev, O.; Austin, A. J.; Cammi, R.; Pomelli, C.; Ochterski, J. W.; Ayala, P. Y.; Morokuma, K.; Voth, G. A.; Salvador, P.; Dannenberg, J. J.; Zakrzewski, V. G.; Dapprich, S.; Daniels, A. D.; Strain, M. C.; Farkas, O.; Malick, D. K.; Rabuck, A. D.; Raghavachari, K.; Foresman, J. B.; Ortiz, J. V.; Cui, Q.; Baboul, A. G.; Clifford, S.; Cioslowski, J.; Stefanov, B. B.; Liu, G.; Liashenko, A.; Piskorz, P.; Komaromi, I.; Martin, R. L.; Fox, D. J.; Keith, T.; Al-Laham, M. A.; Peng, C. Y.; Nanayakkara, A.; Challacombe, M.; Gill, P. M. W.; Johnson, B.; Chen, W.; Wong, M. W.; Gonzalez, C.; Pople, J. A. *Gaussian 03, revision C.02*; Gaussian, Inc.: Wallingford, CT, 2004.